



The Sputtering and Characterization of C-Axis Oriented Aluminium Nitride Thin Films On Top Of Cubic Silicon Carbide-On-Silicon Substrates for Piezoelectric Applications

Author

Iqbal, Abid

Published

2017

Thesis Type

Thesis (PhD Doctorate)

School

Griffith School of Engineering

DOI

[10.25904/1912/1876](https://doi.org/10.25904/1912/1876)

Downloaded from

<http://hdl.handle.net/10072/365840>

Griffith Research Online

<https://research-repository.griffith.edu.au>



***The Sputtering and Characterization of C-Axis Oriented
Aluminium Nitride Thin Films On Top Of Cubic Silicon
Carbide-On-Silicon Substrates for Piezoelectric Applications***

A Thesis

Submitted to

The Griffith School of Engineering

Griffith University

Brisbane, Australia

by

Abid Iqbal

B. Eng, M. Eng

Submitted in fulfilment of the requirements for the degree

of

Doctor of Philosophy

October 2016

ABSTRACT

The growth of micro-scale wireless electronics is increasing significantly because of their miniaturisation and low power consumption. These devices currently draw power from batteries or chemical fuel cells. Their limited life-spans prompt active research to find an alternative solution by harvesting ambient energy from the environment. Numerous sources are available such as solar, thermoelectric, acoustic, and mechanical vibrations. Among them, mechanical vibration is perhaps the most practical to power these wireless electronic devices via piezoelectric transduction. Three most common piezoelectric materials are Lead zirconate titanate (PZT), zinc oxide (ZnO) and aluminum nitride (AlN). AlN is preferred over ZnO and PZT for several reasons. Chiefly among them is because it has the highest electromechanical coupling along the *c*-axis of wurzite AlN for longitudinal deformation.

This thesis investigates the sputtering of *c*-axis oriented AlN on top of cubic-silicon carbide-on-silicon (3C-SiC-on-Si) substrates for piezoelectric applications. The 3C-SiC buffer layer was used to reduce the lattice mismatch and thermal expansion coefficient between AlN and Si. In the first part of the research, RF sputtering was utilised for depositing AlN. The low growth rate of RF sputtering prompted the switch to DC sputtering. The DC sputtering suffered from electrical arching problems, which were addressed by gradually decreasing the sputtering pressure. However, the system had the limitation of 1200 W of maximum power. Therefore, Pulsed DC sputtering was employed to ramp up the power to 2400 W, as well as obtaining higher growth rate and low electrical arching. Throughout these experiments, the role of deposition pressure, sputtering power, deposition temperature, nitrogen concentration and substrate orientation towards the formation of a highly *c*-axis AlN films were systematically elucidated. The deposited films were selectively characterised in term of deposition rate, surface roughness, crystal quality, refractive index, in-plane stress and piezoelectric coefficient.

In the last part of this study, the applications of the AlN thin films as cantilever-based energy harvesters and bio-sensors were simulated. All structures used 3C-SiC as the bottom electrode, AlN as an active layer (piezoelectric element), and molybdenum (Mo) as the top electrode and proof mass. The dimensions of these structures were optimised using Matlab and verified by Finite Element Analysis (FEA) using Comsol and Intellisuite. The results from mathematical and FEA modelling were then compared and discussed.

*To my beloved parents, sisters, brother, nephews, niece, and friends
for their love, endless support
and encouragement.*

ACKNOWLEDGEMENT

Although it has been challenging, working towards a PhD degree has been truly rewarding, and I will forever treasure the lessons learned in the process. It gives me great honour to acknowledge the amazing people that have made all of this possible.

Working at the Queensland Micro- and Nanotechnology Centre, Griffith University, has been an incredible experience. I believe QMNC is a unique centre in the sense that the sharing of ideas and knowledge extends beyond individuals and to between groups with various backgrounds. I can never express my gratitude enough to the people who have helped me and have made a significant contribution to making this thesis possible.

First and foremost, I would like to convey my deepest and sincerest gratitude to my principal supervisor, Dr. Faisal Mohd-Yasin, for taking me on as a student and providing continuous supervision, guidance, and encouragement throughout my doctoral journey. Without his endless support, guidance, and enlightened contribution to this research, there would be no thesis. Moreover, even in his own difficult times, he never wavered in his leadership and wisdom. Everything you have done for me, your support, time and energy, is greatly appreciated.

My sincere gratitude is extended to Alan Iacopi, Glenn Walker, Kien Chaik and Leonie Hold for their invaluable technical assistance and guidance in operating the clean room equipment. Dr. Philip Tanner has been a valuable resource in helping me with electrical measurements. Their advice and opinions in response to my complicated queries and questions have served me well, and I owe them my heartfelt appreciation.

I would also like to acknowledge the financial support and scholarships (GUPRS and GUIPRS) provided by Griffith University. Also, I would like to acknowledge Mr Zailan Mohd Yusof of The National University of Malaysia (Bangi, Malaysia) and Dr. Alana Fernandes of Bluglass Ltd. (Sydney, Australia) for the XRD measurements.

Thanks, Lacey Shaw and Kerryn Iacopi, for all your help, administrative support, and assistance during the whole period of my PhD. Thank you to all my friends and colleagues for their amazing support throughout my education at the postgraduate level. Thanks to all the people whom I have forgotten to mention who have made a contribution, no matter how small, in supporting me through my life.

Finally, I would like to express my endless gratitude to my wonderful parents, sisters, brother, and other family members for their support and love throughout the years. I will never be able to thank you enough.

Abid Iqbal

STATEMENT OF ORIGINALITY

This work has not previously been submitted for a degree or diploma in any university. To the best of my knowledge and belief, the thesis contains no material previously published or written by another person except where due reference is made in the thesis itself.

_____Abid Iqbal_____

Author's Signature

Date: 18th October 2016____

TABLE OF CONTENTS

Abstract	I
Acknowledgement	IV
Statement of originality.....	VI
Table of contents.....	VIII
Selected List of Abbreviations	X
Chapter 1: Introduction	1
1.1 Significance of Research Work	2
1.2 Piezoelectricity	3
1.3 Current status and practical challenges:.....	6
1.4 Original research contributions	7
1.5 Thesis outline.....	8
1.6 Related publications	10
Chapter 2: Literature Review:.....	12
Chapter 3: RF sputtering of polycrystalline (100), (002) and (101) oriented AlN on an epitaxial 3C-SiC (100) on Si(100) substrate	47
Chapter 4: Controlled Sputtering of AlN (002) and (101) Crystal Orientations on Epitaxial 3C-SiC-on-Si (100) Substrate.....	63
Chapter 5: Highly c-axis oriented AlN on 3C-SiC-on-Si (111) substrates by DC reactive magnetron sputtering	76
Chapter 6: The sputtering of c-axis oriented AlN films on top of on- and off-axis 3C-SiC/Si (111) substrates at different deposition temperatures	92
Chapter 7: The effect of substrate temperature and sputtering power on the quality of AlN (002) films sputtered on top of 3C-SiC/Si (100) substrates	106
Chapter 8: Applications of AlN/3C-SiC/Si composite layers for piezoelectric applications	117

8.1. The design and optimization of two low frequency energy harvesters employing 3C-SiC/AlN/Mo composite layers	118
8.2. Design optimization and finite element analysis of AlN/3C-SiC piezoelectric bio-sensors	127
8.3. Comparison of seven cantilever designs for piezoelectric energy harvester based on Mo/AlN/3C-SiC	132
Chapter 9: Conclusions and recommendations	138
9.1. Conclusion:	139
9.2. Suggestions for future research.....	140

SELECTED LIST OF ABBREVIATIONS

RF.....Radio Frequency

Si.....Silicon

SiC.....Silicon Carbide

DC SputtererDirect Current sputtering

SiO₂.....Silicon Dioxide

FWHMFull width half Maximum

AlN.....Aluminium Nitride

Mo.....Molybdenum

XRDX-ray Diffraction

AFMAtomic force microscopy

SEMScanning electron microscope

Chapter 1: Introduction

1.1 Significance of Research Work

The use of wireless sensor networks are growing for various applications; security, agriculture, building environmental control, and monitoring structural and machine health. A wireless sensor network consists of sensor nodes that are spatially distributed and capable of communicating with other nodes to transmit data to the central hub. A sensor node comprises of a sensing unit, processing unit (microcontroller and external memory), transceiver, and communicating unit. The advancement in integrated circuit design and reduction in the size of the chips has reduced the power requirements for these sensor nodes. They have an average power consumption of $6\text{-}300 \mu\text{W}$, depending on the mode of operation i.e. idle or active [1].

Wireless sensor nodes are designed to run on conventional batteries. The increase in the use of wireless nodes and the decrease in their sizes have attracted researchers to seek alternative solutions to power the nodes. Common alternative solutions being developed are micro fuel cells and microturbine generators that involve chemical energy that need to be refuelled. Both are capable of providing high energy and power density for recharging devices such as laptops and mobile batteries. However, due to the prolonged service life of wireless sensors, the fuel replacement of their batteries is becoming a formidable and expensive process. Ambient energy sources are another alternative for powering these low-power wireless sensor nodes or electronics [2, 3].

Numerous sources are available such as solar, thermoelectric, acoustic, and mechanical vibrations. Among these, mechanical vibration is perhaps the most practical to power these wireless electronic devices via piezoelectric transduction. Three most common piezoelectric materials are Lead zirconate titanate (PZT), zinc oxide (ZnO) and aluminium nitride (AlN). AlN is preferred over ZnO and PZT for several reasons. Chiefly among them is because it has the highest electromechanical coupling along the *c*-axis of wurtzite AlN for longitudinal deformation [4].

This thesis investigates the sputtering of *c*-axis oriented AlN on top of cubic-silicon carbide-on-silicon (3C-SiC-on-Si) substrates for piezoelectric applications. The 3C-SiC buffer layer was used to reduce the lattice mismatch and thermal expansion coefficient between AlN and Si. The deposited films were selectively characterised in term of deposition rate, surface roughness, crystal quality, refractive index, in-plane stress and piezoelectric coefficient.

The use of silicon carbide materials also opens up new research areas for microsensors and electronics to operate in high temperature, high shock, and chemically corrosive environments. Silicon Carbide (SiC) has been identified as a platform material for electronics in harsh environments due to its strong characteristics of thermal, mechanical, and electrical stability[5].

1.2 Piezoelectricity

Piezoelectricity was derived from the Greek word “piezo”, which means “to squeeze”. It is the property of crystalline materials that develop an electric dipole when mechanical strain is applied to them, and they conversely exhibit an induced mechanical strain when subjected to an electric potential. In dielectrics, the electrons are strongly tied to the outermost atomic shells and form a symmetrical cloud around the nucleus in the absence of an electric field. In non-polar dielectrics, the electric field polarizes the atom or molecules in the material by moving the centre of the electron cloud away from the nucleus, resulting in the formation of the net electric dipole. All of these individual dipoles add up over the entire crystal and produce a net polarization that results in electric field generation across the material [6].

The relation between the stress and strain in the linear elastic material can be given by Hooke's law:

$$S = sT \text{ or } T = cS \quad (1.1)$$

where S is the mechanical strain, T is the mechanical stress, s is the elastic compliance constant, and c is the elastic stiffness constants. Similarly, the relation between electrical charge density displacement (D) and electric field (E) can be given by Gauss's law:

$$D = \epsilon_0 E + P \quad (1.2)$$

where D is the electric displacement vector (C/m^2), ϵ_0 is permittivity of free space (F/m), E is the electric field intensity (C/m^2) and P is the electric polarization vector (C/m^2). The piezoelectric properties of the material can be combined using Gauss's and Hooke's law, which is called electromechanical coupling. Equation 1.3 is typically used for the direct piezoelectric effect, while equation 1.4 is typically used for the indirect piezoelectric effect [6].

$$D = d \cdot T + \epsilon^T \cdot E \quad (1.3)$$

$$S = S^E \cdot T + d \cdot E \quad (1.4)$$

where D is electric displacement vector, $d \cdot T$ is six by six compliance matrix at constant electric field, ϵ^T is a dielectric constant tensor under constant stress, E is the electric field vector, S^E is the elastic compliance tensor at constant electric field, S is a six-dimensional strain vector, T is mechanical stress, and d is the piezoelectric constant tensor. The piezoelectric strain coefficient is defined as the strain developed per unit applied electric field strength or developed charge density per given strain.

1.2.1 Electromechanical Coupling Coefficient:

The electromechanical coupling coefficient k measures the efficiency of the mechanical energy that is converted into the electrical energy or vice versa. Therefore, it can be defined by equation 1.5 or 1.6 [7]:

$$k^2 = \frac{\text{Mechanical energy converted to electrical energy}}{\text{Electrical energy converted to mechanical energy}} \quad (1.5)$$

$$k^2 = \frac{\text{Electrical energy converted to mechanical energy}}{\text{Mechanical energy converted to electrical energy}} \quad (1.6)$$

1.2.2 Piezoelectric Material Properties:

Piezoelectric materials are evaluated based on key properties such as electromechanical coupling coefficient (k), piezoelectric strain coefficient (d) dielectric constant (ϵ) and Young's modulus (Y). The values of d and k must be significant for energy harvesting application. The Young's modulus deals with the stiffness of the piezoelectric material, which plays a vital role in resonance frequency and material strength. It is preferable that the dielectric constant (ϵ) of the piezoelectric materials is higher to decrease the source impedance [8].

1.2.3 Modes of Operation:

In piezoelectric materials, the positive charges are not uniformly distributed at the centre of atoms that creates a charge dipole. The direction along which the dipoles align is known as the "poling direction". In general, this poling direction is randomly distributed in the polycrystalline piezoelectric material, as shown in Figure 1.1 (a). This direction can be modified by applying voltages or a heat gradient across the material, as shown in Figure 1.1 (b). A Piezoelectric material has its specific temperature, known as the Curie temperature.

The material can be de-poled if it is exposed to a temperature higher than the Curie temperature of the material. When the voltage is applied across the piezoelectric material, the new poling direction will remain the same, even after the removal of voltage as shown in Figure 1.1 (c) [9].

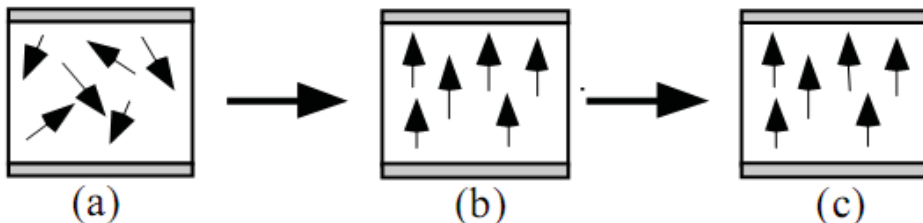


Fig.1.1. (a) Random poling direction; (b) Applied voltage above Curie temperature; (c) Poling direction remains same after removal of applied voltage.

In a linear dielectric medium, the induced polarisation field is directly proportional to the magnitude of electric field. This polarization field depends on the material properties. The isotropic piezoelectric material allows the polarisation field and electric field to remain equal in all directions. Alternately, an anisotropic piezoelectric materials allow polarization to take place along certain directions.

The relationship between the applied stress and the charge generated can be defined as the piezoelectric constant (D_k). This piezoelectric constant remains the same under static load conditions while it changes dramatically near resonance conditions. This relationship under the open circuit and static conditions can be given as:

$$D_k = d_{kij}\sigma_{ij} \quad (1.7)$$

where D_k represents charge per area and σ_{ij} is applied stress on the piezoelectric material. d_{kij} (C/N) is a third-rank tensor of piezoelectric coefficients. Both direct and converse piezoelectric effects are frequently expressed using the reduced matrix notation d_{km} , where k denotes the component of electric displacement D or field E in the Cartesian coordinates (x_1, x_2, x_3), and the index m = 1,...,6 is used to define the mechanical stress or strain. The value of m = 1, 2, and 3 correspond to the normal stresses along the x_1 , x_2 , and x_3 axes, respectively, whereas m = 4, 5, and 6 denote the shear stresses. The piezoelectric materials have five piezoelectric constants: d_{31} , d_{32} , d_{33} , d_{15} and d_{24} . Among these, piezoelectric constants d_{31} and d_{32} are equal in magnitude. Similarly, d_{15} and d_{24} have the same magnitude. Conventionally, the value of d_{15} and d_{33} is five and three times greater than d_{31} , respectively [9].

1.2.4 Vibration modes:

There are two vibrating modes for the piezoelectric effect; A longitudinal mode, which is also known as the d_{33} mode and transverse mode, which is commonly referred to as a d_{31} mode. In the longitudinal mode, the direction of the force is parallel to the poling direction, while in the transverse mode the force is perpendicular to the poling direction [9]. Both modes are illustrated in Figure 1.2 and Figure 1.3.

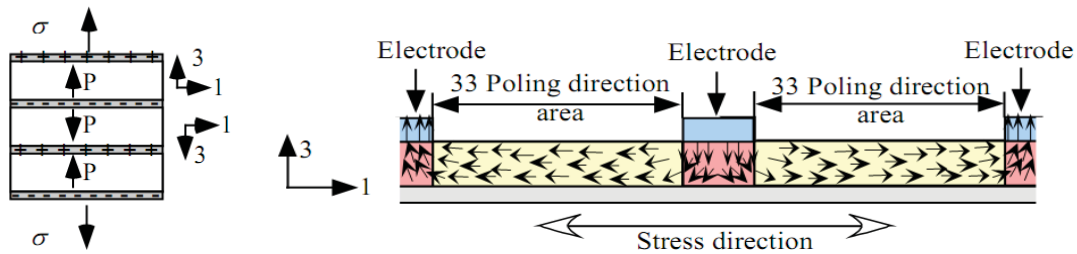


Fig.1.2 (left figure) Piezoelectric stacked and its poling direction in d_{33} mode
 (right figure) Interdigitated electrode arrangement on piezoelectric layer

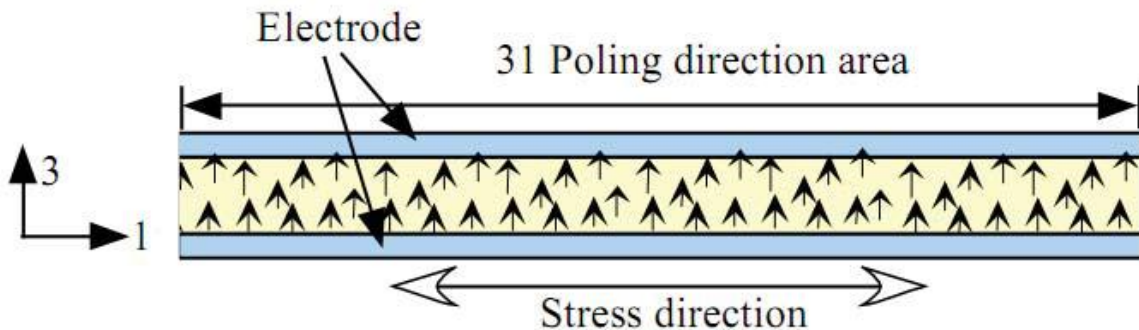


Fig.1.3 d_{31} mode piezoelectric device

1.3 Current status and practical challenges:

An exhaustive literature review on the sputtering of c-axis AlN will be covered in chapter 2. From that review, it was found that only a few reports have been published on the utilisation of 3C-SiC buffer layers to minimize the lattice mismatch and coefficient of thermal expansion between the Si substrate and AlN film. These values are shown in Table 1.1.

In terms of the intended applications, most of the reported energy harvesters are designed and tested for normal environmental conditions. Only a few of the energy harvesters are designed for harsh environmental conditions such as high temperature and corrosive environments [10]. Silicon carbide is highly stable in high temperatures and corrosive

environments. Therefore, we simulated the employment of silicon carbide as a structural layer as well as a lower electrode for electrical connections. Aluminium nitride is proposed as the piezoelectric materials because of its high Curie temperature of 1100 degree Celcius [11], which is needed if we target the application around 600 degree Celcius. Molybdenum (Mo) is proposed for use as a second electrode as well as for the mass, due to its high melting point (2623 °C) and high density. The material properties of all three layers are shown in Table 1.1.

Table 1.1: Material Properties of 3C-SiC, AlN, and Mo

Parameters	Si	3C-SiC	AlN	Mo
Young's Modulus [GPa]	140-188	440	330	312
Density [kg/m3]	3200	3100	3300	10200
Poisson's Ratio	0.28	0.14	0.24	0.30
Coefficient of Thermal Expansion 10-6 [1/K]	2.6	4	4.6	4.8
Specific Heat [J/(kg*K)]	700	750	740	250
Thermal Conductivity [W/(m*K)]	149	120	140-180	138

1.4 Original research contributions

The original research contributions can be summarised as follows:

- An exhaustive literature review of the sputtering conditions and their effects on the formation of AlN (002) films being deposited on a variety of substrates;
- the sputtering of highly c-axis oriented AlN films on top of 3C-SiC-on-Si substrates for piezoelectric applications;
- the characterization of the crystal quality of the said films on the crystal quality, surface roughness, deposition rate, refractive index, residual stress and piezoelectric constant;

- the elucidation on the role of sputtering parameters (sputtering pressure, substrate temperature, gas ratio, and deposition power, etc.) on the crystal orientation and surface roughness of deposited AlN thin films;
- the tuning of the residual stress of the selected AlN films from compressive to tensile using RF bias;
- the simulated applications of the sputtered AlN films for energy harvester and bio-sensor.

1.5 Thesis outline

The rest of the thesis will cover the following:

Given that the sputtering parameters play a vital role in crystal orientation and quality of deposited films, a literature review of AlN (002) deposition on a variety of substrates is presented in Chapter 2. This chapter will be submitted as a review in *Microelectronic Engineering* or equivalent.

Chapter 3 discusses the RF sputtering of polycrystalline AlN on top of 3C-SiC/Si (100) substrates. We studied the role of gas ratio, sputtering pressure, and power on AlN crystal orientations. This chapter was published as a research article in *Journal of Vacuum Science and Technology B*.

Chapter 4 discusses the effect of Nitrogen/Argon ratio on crystal orientations of polycrystalline AlN on top of 3C-SiC/Si (100) substrates using a standard DC sputterer. This chapter was published as a research article in *Journal of Crystal Growth*.

Chapter 5 elucidates the effect of low lattice mismatch of 1 % between AlN (002) and 3C-SiC/Si(111) substrates to produce a highly c-axis oriented AlN film using the same sputtering technique and equipment as in chapter 4. This chapter has been submitted as a manuscript to the *Journal of Crystal Growth*.

Chapter 6 describes the effect of deposition temperature to produce a highly c-axis oriented AlN film on top of on-axis and off-axis 3C-SiC/Si(111) substrates using a pulsed-DC sputtering system. This chapter will be submitted as a manuscript in *Thin Solid Films* or equivalent.

Chapter 7 investigates the role of substrate temperature and sputtering power of AlN films being grown on top of 3C-SiC/Si (100) substrates, which has been batch-fabricated with samples from chapter 6. This chapter will be submitted as a manuscript in *Thin Solid Films* or equivalent.

Chapter 8 includes three conference papers that have been published to simulate the applications of the AlN films as an energy harvesters and bio-sensors using the Mo/AlN/3C-SiC-on/Si structure.

Finally, the key conclusions and developments made throughout the study, along with recommendations for future work, are summarised in Chapter 9.

1.6 Related publications

List of papers constituting this thesis (in order of the chapters):

- **Iqbal, A.**, Chaik, K., Walker, G., Iacopi, A., Mohd-Yasin, F., & Dimitrijev, S. (2014). RF sputtering of polycrystalline (100),(002), and (101) oriented AlN on an epitaxial 3C-SiC (100) on Si (100) substrate. *Journal of Vacuum Science & Technology B*, 32(6), 06F401.
- **Iqbal, A.**, Walker, G., Iacopi, A., & Mohd-Yasin, F. (2016). Controlled sputtering of AlN (002) and (101) crystal orientations on epitaxial 3C-SiC-on-Si (100) substrate. *Journal of Crystal Growth*, 440, 76-80.
- **Iqbal, A.**, Walker, G., Iacopi, A., & Mohd-Yasin, F. (2016). Highly c-axis oriented AlN on 3C-SiC-on-Si (111) substrates by DC reactive magnetron sputtering. Submitted to *Journal of Crystal Growth*, (under review)
- **Iqbal, A.**, Mohd-Yasin, F., & Dimitrijev, S. (2014, October). The design and optimization of two low frequency energy harvesters employing 3C-SiC/AlN/Mo composite layers. In *AIP Conference Proceedings*, Vol. 1621, No. 1, pp. 290-296
- **Iqbal, A.**, Mohd-Yasin, F., & Dimitrijev, S. (2014, August). Design optimization and finite element analysis of AlN/3C-SiC piezoelectric bio-sensors. In *Semiconductor Electronics (ICSE), 2014 IEEE International Conference on* (pp. 509-512). IEEE.
- **Iqbal, A.**, & Mohd-Yasin, F. (2015, August). Comparison of seven cantilever designs for piezoelectric energy harvester based On Mo/AlN/3C-SiC. In *Micro and Nanoelectronics (RSM), 2015 IEEE Regional Symposium on* (pp. 1-4). IEEE.

List of papers not included in this thesis (outside the scope of this thesis)

- **Iqbal, A.**, Mohd-Yasin, F., & Dimitrijev, S. (2014). Design Optimization and Finite Element Analysis of 3C-SiC Bio-Sensors based on Dogbone Resonator. *Applied Mechanics & Materials*, (595).
- V. V. Sasi, **A. Iqbal** , K. Chaik, P. Tanner, A. Iacopi and F. Mohd-Yasin, "RF Sputtering of ZnO (002) Thin Films on top of 3C-SiC- on-Si (100) Substrates for Low Cost, Piezoelectric Devices" In *30th Eurosensors Conference (Eurosensors 2016) Procedia Engineering*

References:

- [1] S. Roundy, P. K. Wright, and J. M. Rabaey, *Energy scavenging for wireless sensor networks*: Springer, 2003.
- [2] S. P. Beeby, M. J. Tudor, and N. White, "Energy harvesting vibration sources for microsystems applications," *Measurement science and technology*, vol. 17, p. R175, 2006.
- [3] N. E. Dutoit, B. L. Wardle, and S.-G. Kim, "Design considerations for MEMS-scale piezoelectric mechanical vibration energy harvesters," *Integrated Ferroelectrics*, vol. 71, pp. 121-160, 2005.
- [4] Z. Vashaei, T. Aikawa, M. Ohtsuka, H. Kobatake, H. Fukuyama, S. Ikeda, *et al.*, "Influence of sputtering parameters on the crystallinity and crystal orientation of AlN layers deposited by RF sputtering using the AlN target," *Journal of Crystal Growth*, vol. 311, pp. 459-462, 2009.
- [5] P. M. Sarro, "Silicon carbide as a new MEMS technology," *Sensors and Actuators A: Physical*, vol. 82, pp. 210-218, 2000.
- [6] S. Roundy and P. K. Wright, "A piezoelectric vibration based generator for wireless electronics," *Smart Materials and structures*, vol. 13, p. 1131, 2004.
- [7] A. Kholkin, B. Jadidian, and A. Safari, "Ceramics, piezoelectric and electrostrictive," *Encyclopedia of Smart Materials*, 2002.
- [8] S. Priya and D. J. Inman, *Energy harvesting technologies* vol. 21: Springer, 2009.
- [9] S. Kim, "Low power energy harvesting with piezoelectric generator," University of Pittsburgh, 2002.
- [10] M. Ishihara, S. Li, H. Yumoto, K. Akashi, and Y. Ide, "Control of preferential orientation of AlN films prepared by the reactive sputtering method," *Thin Solid Films*, vol. 316, pp. 152-157, 1998.
- [11] E. Iborra, J. Olivares, M. Clement, L. Vergara, A. Sanz-Hervás, and J. Sangrador, "Piezoelectric properties and residual stress of sputtered AlN thin films for MEMS applications," *Sensors and Actuators A: Physical*, vol. 115, pp. 501-507, 2004.

Chapter 2: Literature Review:

The role and ranges of sputtering parameters to grow c-axis oriented aluminium nitride for piezoelectric applications

Abstract:

A highly c-axis oriented Aluminum Nitride thin film is preferred for piezoelectric applications. This paper provides guidelines on the commonly used ranges of sputtering parameters towards this goal. These guidelines are compiled based on 50 journal articles that report the sputtering of c-axis AlN films on a wide variety of substrate materials and equipment. We selectively highlight key works that study the role of each sputtering parameters. Finally, the interdependent relationships between all the sputtering parameters in view of the kinetic energies and surface mobility of the adatoms towards growing highly c-axis AlN films are illustrated.

Keywords: physical vapor deposition; sputtering ; aluminium nitride; piezoelectric

I. Introduction

Energy harvesting or energy scavenging is the process of extracting minute amounts of energy from ambient sources in the environment. The energy harvester is used to power wireless sensors instead of conventional batteries because of their limited life span and inefficient recharging and battery replacement. The ambient sources are broadly divided into four categories: solar, thermal, wind and mechanical vibration [1]. Numerous research groups have investigated different methods to convert the ambient sources into electrical energy via non-resonant and resonant devices [2]. In recent years, energy harvesting approaches have been proposed using solar, thermoelectric, electromagnetic, piezoelectric, and capacitive schemes at the micro and nanoscales. Among them, piezoelectric emerges as the most practical solution. Piezoelectric transduction does not require external power sources for polarisation in comparison to electrostatic transductions, and also it is easy to fabricate compared to electromagnetic transductions [3].

Piezoelectricity was derived from the Greek word “piezo”, which means “to squeeze”. It is the property of crystalline materials that develop an electric dipole when mechanical strain is applied to them. They conversely exhibit an induced mechanical strain when subjected to an electric potential. In dielectrics, the electrons are strongly tied to the outermost atomic shells and form a symmetrical cloud around the nucleus in the absence of an electric field. In non-polar dielectric, the electric field polarizes the atom or molecules in the material by moving the centre of the electron cloud away from the nucleus, resulting in the formation of the net electric dipole. All of these individual dipoles add up over the entire crystal and produce a net polarization that results in electric field generation across the material [4].

Figure 1 shows the process of converting mechanical to electrical energies through piezoelectric transduction. There are three primary steps. In the first step, the mechanical energy is absorbed from the ambient environment. It can be in the form of vibration, force or motion. In the second step, this energy is piezoelectrically transduced to electrical voltage and current. Finally, the electrical energy is rectified and stored [5].

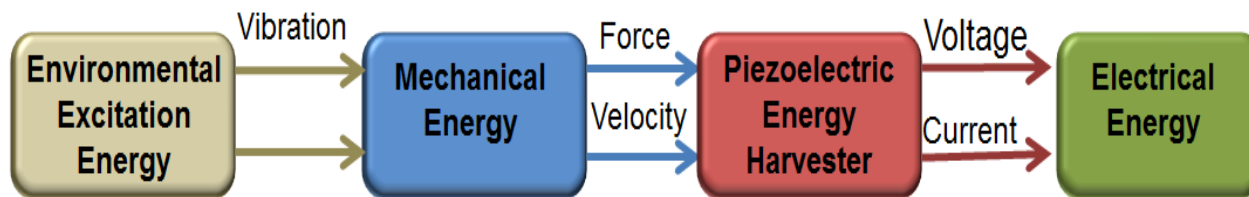


Fig 1: Piezoelectric transduction of mechanical to electrical energies.

Piezoelectric materials are classified into five categories i.e., polycrystalline, single crystal, polymers, ceramics and thin films [6]. The selection of these materials depends on the deposition methods, process complexity and application's compatibility. Thin films have a substantial

range of advantages such as low hysteresis, high sensitivity, low power requirements and the ability to generate large mechanical deflections. The three most commonly used piezoelectric thin films are lead zirconate titanate (PZT), zinc oxide (ZnO) and aluminium nitride (AlN).

PZT is preferred in piezoelectric applications due to its high electromechanical coupling coefficient (k) and piezoelectric coefficient (d_{ij}). However, the presence of lead in PZT results in possible contamination in the clean room during its processing. ZnO and AlN exhibit similar values of k and d_{ij} . The key difference is the fact that zinc oxide performance degrades significantly at high temperature due to its low Curie point (50° Celcius). If the micro-scale energy harvester is targeted to work at high temperature, AlN trumps over PZT and ZnO due to these reasons.

The primary contribution of this review is the generic guidelines on the role and ranges of sputtering parameters towards achieving highly c-axis AlN films. This information has been extracted from 50 journal articles. The rest of the chapter is as follows. Section II first describes the AlN crystal structure. Section III then states the structural, optical, thermal, and piezoelectric properties of AlN. Section IV and V discuss the basic sputtering system and the summaries of AlN deposition works, respectively. In several of these reviewed articles, the intended applications are also described. Some examples include BAW and SAW devices [7], PZT transducers [8] and a large voltage source [9]. Section VI concludes by providing the optimized range of sputtering parameters for *c-axis* AlN thin films from a variety of substrates and sputtering equipment.

II. AlN Crystalline Structure

AlN belongs to the III–V semiconductor family because it has a close-packed crystal structure [10]. In particular, AlN has a hexagonal closed-packed wurtzite structure, with lattice parameters ranging from 3.110 to 3.113 Å for the a-axis, and from 4.978 to 4.982 Å for the c-axis. The c/a ratio varies between 1.600 and 1.602, deviating from the ideal wurtzite structure, which is probably due to lattice instability [11]. It has higher values of hardness and thermal conductivity compared to the other members of the III-V nitride semiconductors. The AlN crystalline structure,

bond configuration and different planes in AlN are shown in Figure 2. Each Al atom is surrounded by four N atoms, forming a tetrahedron with three B_1 bonds between Al-N(i) ($i=1,2,3$) and one B_2 bond between Al-N₀ bond in the c-axis direction. The bond lengths of B_1 and B_2 are 0.1885 and 0.1917 nm, respectively. The bond angle for N₀-Al-N₁ is 107.7° and that for N₁-Al-N₂ is 110.5°. The (100) plane is composed of the B_1 bonds, while (002) and (101) planes consist of the B_1 and B_2 bonds [12]. The kinetic energy of the sputtering particles directly modifies the adatoms mobility. The adatoms with low mobility contributes to B_1 bonds that produced the (100) plane, while the adatoms with high kinetic energy contributes to B_1 and B_2 bonds that create (101) and (002) plane.

The standard PDF card of AlN (PDF-65-0832) XRD pattern is shown in Figure 3.

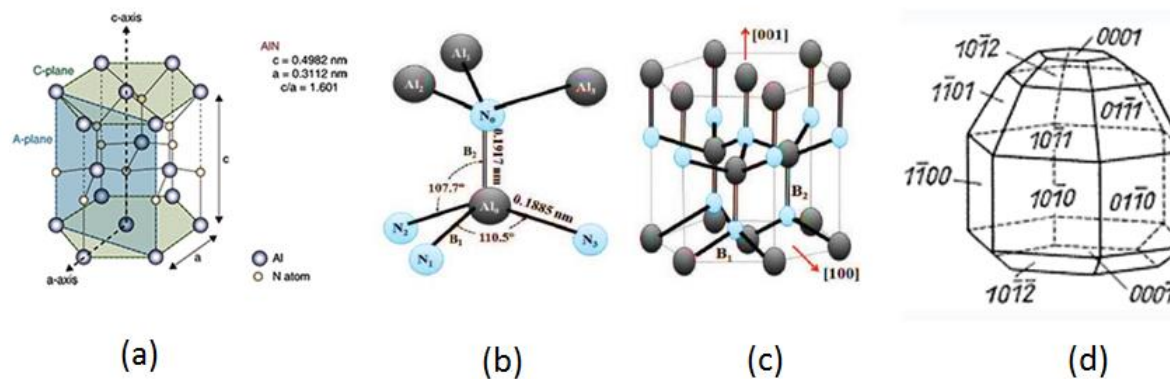


Figure 2: (a) Crystal structure of AlN (b) Bond configuration of AlN (c) Bonds in configurations (d) Planes in AlN

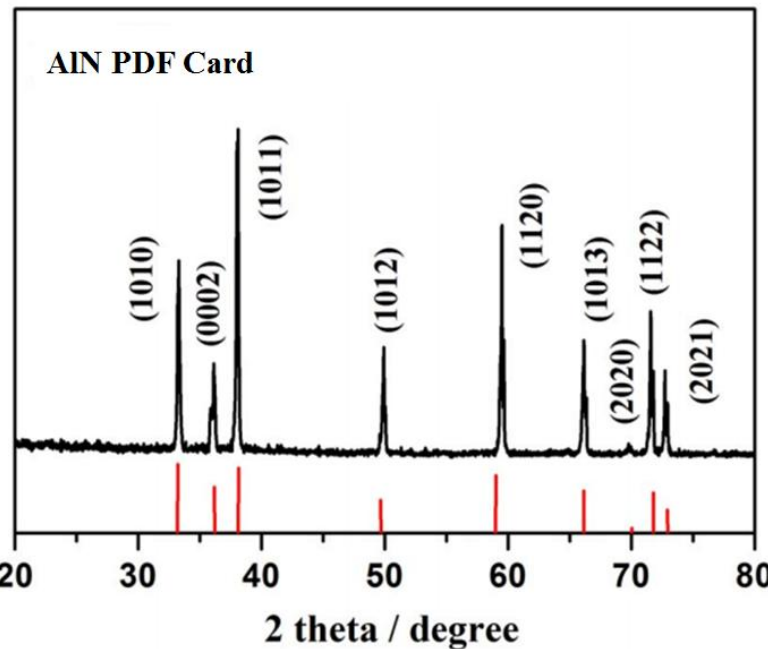


Figure 3: The standard PDF card of AlN (PDF-65-0832) XRD patterns.

III. Aluminium Nitride Properties

The structural, optical, thermal, and piezoelectric properties of AlN are given in Table 1 [13, 14]. AlN possesses a large energy band-gap of about 6 eV [8, 9], high thermal conductivity (260 W/(m.K)), high breakdown voltage (15 kV/mm), high resistivity ($10^{14} \Omega \cdot \text{cm}$), and high thermal and chemical stability at high temperatures in comparison to other common piezoelectric materials. It has high SAW velocity (5910 m/s) and moderate electromechanical coupling coefficient (~1 %) [15]. The value of this parameter is highest along the (002) plane i.e. c-axis.

Table 1. The List of AlN Basic Properties

Structural Properties	Density (g/cm ³)	3.257
	Modulus of Elasticity (GPa)	331
	Elastic Constant C ₁₁ (GPa)	410±10
	Elastic Constant C ₁₂ (GPa)	149±1
	Elastic Constant C ₁₃ (GPa)	99±4
	Poisson's Ratio	0.22
	Common Crystal Structure	Wurtzite
	Lattice constant (Å)	a = 3.112 c = 4.982
	Hardness (Kg/mm ²)	1100
	Water Absorption	None
Optical Properties	Density of states Conduction Band (cm ⁻³)	4.1×10 ¹⁸
	Effective hole mass	m _{hz} = 3.53 m ₀ m _{hx} = 10.42 m ₀
	Density of states V band (cm ⁻³)	4.8×10 ²⁰
	Optical phonon energy (meV)	113
	Refractive index (vis-ir)	~2.15
Electrical Properties	Breakdown field (V/cm)	1.2-1.8×10 ⁶
	Mobility electrons holes (cm ² /VS)	135 / 14
	Dielectric constant (static/high frequency)	8.5-9.14/4.6-4.84
	Energy Band Gap (eV)	6.13-6.23
	Resistivity (Ohm.cm)	10 ¹⁴
Thermal Properties	Thermal conductivity (W/m°K)	175
	Thermal expansion (×10 ⁻⁶ /°C)	4.2-5.3
	Debye temperature (K)	980
	Melting Point (°C)	2200

Piezoelectric Properties	Coupling Coefficient (C/m^2) e_{15}	-0.33~-0.48
	Coupling Coefficient (C/m^2) e_{31}	-0.38~-0.82
	Coupling Coefficient (C/m^2) e_{33}	1.26-2.1
	Relativity Permittivity Coefficient ϵ_{11}	9
	Relativity Permittivity Coefficient ϵ_{22}	9
	Relativity Permittivity Coefficient ϵ_{33}	11

IV. Sputtering:

Sputtering is one of the physical vapour deposition (PVD) methods that are widely used for the deposition of thin films. The schematic of the generic sputtering system is shown in Figure 4. The sputtering system consists of two chambers. The first chamber is the load lock chamber with wafer degas heater. The samples are heated with an IR heater in this chamber in order to remove the moisture. The load lock chamber system are generally turbo-pumped down to a low base pressure ($\approx 10^{-8}$ Torr) to create an ultra-high vacuum in order to reduce the number of particles in the sputtering atmosphere and this decreases possible film contamination. The second chamber, also known as “the main chamber” consists of a high vacuum chamber with sputtering targets, shutters, gas feeds, electrical power supplied (Pulsed DC, RF or DC power), wafer handling and a vacuum system (cryopump system). It is connected to the load lock via a gate valve. The main chamber is normally purged with Ar gas prior to the samples being loaded to avoid contamination.

The samples are placed on a susceptor (sample carrier) and loaded into the load locked chamber which is turbo-pumped down to the low base pressure. They are heated initially to remove the moisture and transferred to the main chamber. The targets generally of 4 " in diameter are set at 20 degrees off perpendicular to the susceptor. The target materials are generally of any solid types such as single metal, alloys or compounds, or insulating and conducting materials. In the sputtering process, electrically neutral argon atoms are introduced into a vacuum chamber at a low pressure (1 to 20 mTorr). The voltage (AC, DC or pulsating DC depends on the system) is applied between the target and substrate which ionizes the argon atoms that creates plasma (consisting of ions and electrons) in the chamber. The negative voltage is applied to

the target, which serves as the cathode, while the positive potential is applied to the susceptor that acts as the anode. These argon ions are accelerated to the target (anode). The target atoms are ejected out from the target surface because of forceful collision from these ions. These target atoms are attracted towards the substrate, where they eventually start to condense into a thin film. The electrons released during argon ionization are also accelerating to the anode substrate; subsequently they collide with additional argon atoms, creating more ions and free electrons in the process and continuing the cycle.

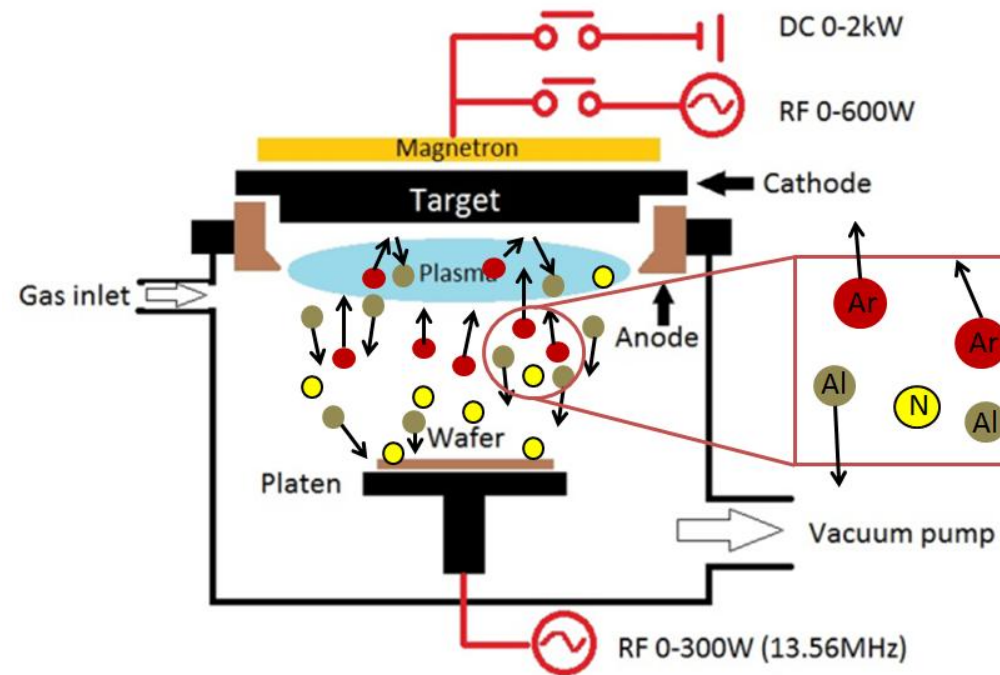


Figure 4: Schematic of a sputtering system used for AlN sputtering [16]

V. The role of sputtering parameters

Table 2 summarises the published works on the deposition of c-axis AlN film on various substrates and using different sputtering equipment. Each row lists the details of one particular work, which is identified by the last name of the first author and year of publication. There are in total 50 articles that were collected and reviewed. The columns listed the following: Author (Year of publication), substrate material, processing type, sputtering power, sputtering pressure, base pressure, N₂/Ar ratio, total gas, distance between target to substrate, FWHM, deposition rate, thickness, surface roughness and notes. The notes column contains additional information that is unique to that particular work. For example, some workers perform annealing on the samples. Therefore the temperature for the post-annealing treatment will be provided, along with the condition and duration of the annealing. Few researchers reported work on the tuning of the in-plane stress of the AlN film via RF bias. Hence, the values of the substrate bias voltage will be provided together with the values of the stresses (in MPa).

The crystal quality of the AlN film is normally given by its FWHM value. However, this review is not able to rank these published works using this parameter because some groups used FWHM of the rocking curve, while others used FWHM of the diffraction peak. There also few older papers that characterized crystal quality in term of peak intensity. Nevertheless, other qualities of thin films such as their deposition rate, thickness and surface roughness are uniformly provided.

The rest of section V discusses the role of the main sputtering parameters, namely the process pressure, the deposition power, the ratio of N₂/Ar, the sputtering temperature, the film thickness, the distance between target to substrate, the bias voltage, the base pressure and the pre-sputtering steps. For each parameter, the supporting physics in view of the kinetic energy and surface mobility of the adatoms will be explained. Afterwards, selected works that explain the dominant role of each sputtering parameter will be highlighted.

Table 2: Summary of published works on the deposition of c-axis AlN film

Authors [ref]	Substrate	Sputtering type	Substrate temperature C	Pressure (mTorr)	Base pressure (mbar)	Nitrogen %	Power (W)	Total Gas (sccm)	Distance between substrate (cm)	FWHM	Deposition rate (nm/min)	Thickness (μm)	Surface roughness (nm)	Notes
Year of Publication														
Ohtsuka et al. [17] (2016)	sapphire	Pulsed DC magnetron sputterer	550	3 to 11 mTorr		50	800		6	3.3 (FWHM of Rocking Curve)	60	1.5		Effect of sputtering pressure on crystalline quality and residual stress.
Stan et al. [18] (2015)	Si	RF magnetron sputterer	50	1.5		25		40	3.5	11, 7.1 (FWHM of Rocking Curve)	19	0.6, 1.1	0.5 to 1.6	Investigated Electric and pyroelectric properties of deposited films.
Wang et al. [19] (2016)	Glass	DC magnetron sputtering	400	9		15	170	35	4.7		66.5	8.35	48	Investigated effect of substrate temperature and bias voltage on crystal orientation.
Jiao et al. [20] (2015)	Si (100), Si (111), SiO ₂ , and amorphous Si (a-Si)	RF Magnetron sputtering	Room temperature	5	5e-4	50, 66, 75, 80	150, 200, 250, 300	60	6				4.22	Effect of various Si substrates on film quality. Effect of RF power and gas flow on residual stress and film quality.
Bi, et al. [21] (2014)	Si (100)	DC magnetron sputtering	400	3	1.12e-10	85	460	22.8	7.5	1.63 (FWHM of Rocking Curve)	7.5	1.8		Measured the longitudinal piezoelectric coefficient of deposited films.
Shih, et al. [22] (2014)	Si ₃ N ₄ /Si	RF Magnetron sputtering	300	5, 10, 15	6.67e-8	60	200, 250, 300		5		11.2	1.9	6.42	Effect of RF power and sputtering pressure on film quality. Fabricated Saw device.
Stoeckel, et al. [23] (2014)	Si (100)	Pulsed DC magnetron sputtering	350	5.25		80	865		7.5	0.39	0.204			Measured Transverse piezoelectric coefficient d ₃₁ .

Authors	Substrate	Sputtering type	Substrate temperature C	Pressure (mTorr)	Base pressure (mbar)	Nitrogen %	Power	Total Gas sccm	Distance between substrate (cm)	FWHM	Deposition rate (nm/min)	Thickness (μm)	Surface roughness nm	Notes
Jiao, et al. [24] (2015)	Si(100) and Si (111)	RF magnetron sputtering	Room temp	4.87	5e-4	50 to 80	150- 350	60	6				4.22	Effect of various Si substrates on film quality.
Yang, et al. [25] (2014)	Mo/Si(100)	RF magnetron sputtering	20 to 600.	7.5	2e-7	50	200		6.5	2.4 (FWHM of Rocking Curve)				Effect of substrate temperature on film quality.
García Molleja, et al. [26] (2013)	SiO ₂ /Si (100)	DC reactive magnetron sputtering	Room temp	3	2e-8	30	100		3	0.8 to 0.19° (FWHM of Diffraction peak)		1.5		Effect of film thickness on residual stress and film quality.
Monteagudo-Lerma, et al. [27] (2013)	C-sapphire	RF reactive sputtering	400	3.5	1e-5	100	150		10.5	1.63 (FWHM of Rocking Curve)		120 nm	1.8 to 0.3	Effect of substrate bias, RF power and substrate temperature on deposited films.
Aissa, et al. [28] (2013)	Si(100)	DC Magnetron sputtering	Room temp	3	6e-5	35	150	40	3		20 to 40 580 fr dcm and 980 fr HiPMS			Comparison of the structural properties and residual stress as a function of sputtering pressure deposited via DCM and HiPMS.
Kale, et al. [29] (2012)	Si, copper, quartz	RF magnetron sputtering	200	6	1e-7	50	100		5					Structural and electrical properties as a function of N ₂ concentration.
Rodríguez-Madrid, et al. [30] (2012)	Microcrystalline diamond	Balanced magnetron sputter deposition	25	3	6.6e-8	75	700	12	4.5	2 (FWHM of Rocking Curve)		3	4.2	Effect of film thickness on film quality for SAW devices.

Authors	Substrate	Sputtering type	Substrate temperature C	Pressure (mTorr)	Base pressure (mbar)	Nitrogen %	Power	Total Gas sccm	Distance between substrate (cm)	FWHM	Deposition rate (nm/min)	Thickness (µm)	Surface roughness nm	Notes
Jin, et al. [31] (2013)	Si(100)	DC magnetron sputtering	430	3	5e-6	50	270	100		2.259 (FWHM of Rocking Curve)	21.78	1	1.97	Effect of substrate temperature on structural properties.
Ababneh, et al. [32] (2012)	Ti/sc	DC magnetron sputtering			4e-3	100	1000		6.5	0.3 (FWHM of Diffraction peak)		0.6	1	Effect of base pressure on film quality.
García-Gancedo, et al. [33] (2011)	IR /Si(100)	Pulse DC magnetron sputtering	400	1.2	2.39e-5	70	1200			1.8 (FWHM of Rocking Curve)	40	1.5	7	AlN based BAW sensors for biometric applications
Phan and Chung [34] (2011)	Si(100)	Pulse DC magnetron sputtering	Room temp	3.5	5e-7	90			8	0.21 (FWHM of Diffraction peak)	8			Effect of post annealing on acoustic wave applications.
Singh, et al. [35] (2011)	N-type Si(100)	RF magnetron sputtering	Room temp	5,10,20	2e-6	50	100,20 0,300		5					Effect of sputtering pressure on deposited films.
Cardenas-Valencia, et al. [36] (2011)	Sapphire	Pulse DC magnetron sputtering	860	1.25, 1.5		50	205	11.5		0.32 (FWHM of Diffraction peak)	200			Novel sputterer as the magnet was embedded in the target.
Iriarte, et al. [37] (2011)	Au/Si substrate	Pulsed DC reactive ion beam	50	2	6.6e-8	55	900	65	5.5	1.3 (FWHM of Rocking Curve)			1.43	AlN growth on Au substrate.

Authors	Substrate	Sputtering type	Substrate temperature C	Pressure (mTorr)	Base pressure (mbar)	Nitrogen %	Power	Total Gas sccm	Distance between substrate (cm)	FWHM	Deposition rate (nm/min)	Thickness (µm)	Surface roughness nm	Notes
Moreira, et al. [38] (2011)	P-Si-(100)	DC magnetron sputtering	50	3	2e-8	27	50	80			70			Electrical characterization of AlN prepared at different N ₂ concentration.
Singh, et al. [39] (2011)	Glass, Si, oxidized Si, Al-SiO ₂ -Si, Cr-SiO ₂ -Si, and Au-Cr-SiO ₂ -Si	RF magnetron sputtering	Room temp	5,10,20	2e-6	100	100,20 0,300			0.32-0.40 (FWHM of Diffraction peak)		1	7.7	Comparison of AlN sputtered at different power and pressure on various substrates.
Subramanian, et al. [40] (2011)	Si(100), glass	DC magnetron sputtering	200	1 *10^-6 m bar	1e-6	50	180		6					Mechanical and Optical properties of deposited films.
Ababneh, et al. [41] (2010)	Si (100)		150-200	1.5, 4.5	5e-6		300, 500, 1000	50	6.5	0.29-0.35 (FWHM of Diffraction peak)	6-12	0.5		Effect of N ₂ concentration, sputtering pressure and deposition power on deposited films.
Stan, et al. [42] (2010)	Si(100)	RF magnetron sputtering	150	~10-4 Pa	1e-6	25	100	40	3	3.5 (FWHM of Rocking Curve)	12.5	0.2, 0.75 and 1		Effect of film thickness on Si, SiO ₂ and Pt substrates.
Vashai et al. [43] (2009)	Silicon	Pulse DC magnetron sputtering	300	2.1		100	1500	50	6	1.2-2.4 (FWHM of Rocking Curve)		0.28 pa		Influence of sputtering parameters on AlN film quality.

Authors	Substrate	Sputtering type	Substrate temperature C	Pressure (mTorr)	Base pressure (mbar)	Nitrogen %	Power	Total Gas sccm	Distance between substrate (cm)	FWHM	Deposition rate (nm/min)	Thickness (µm)	Surface roughness nm	Notes
Clement, et al. [44] (2009)	Iridium layers	Pulse DC magnetron sputtering	400	5	6.6e-8	80	10000		5	2 (FWHM of Rocking Curve)	24			Comparison of BAW resonator performance on Mo and Ir substrates.
Cherng, et al. [45] (2008)	Si(100)	Pulse DC magnetron sputtering			4e-6	40-100	1500		7	2 (FWHM of Rocking Curve)				Two step deposition method by varying power, pressure and N ₂ concentration.
Abdallah, et al. [46] (2008)	Si(100)	DC reactive magnetron sputtering	Room temp	3	1.32e-5	30			3	0.14-0.4 (FWHM of Diffraction peak)	40			Effect of thickness on film quality.
Cherng and Chang [47] (2008)		Pulse DC magnetron sputtering	Room temp	2	5.33e-7	60	600		7	2 (FWHM of Rocking Curve)		1.6		Role of base pressure in AlN deposition.
Chiu, et al. [48] (2007)		DC reactive magnetron sputtering	250–450	3–7.5		30–100	1000–1600		2–12	2.7° (FWHM of Rocking Curve)	12	2	1	Effect of substrate temperature, sputtering power and N ₂ concentration on AlN films.
Kano, et al. [49] (2006)	Si, SiO ₂	RF magnetron sputtering	100	3.75		50	460			8.3				Measured Piezoelectric coefficient up to 300 °C.
Venkataram, et al. [50] (2006)		DC reactive magnetron sputtering	Room temp	6	1.3e-4	variable	500		5.5	0.4 (FWHM of Diffraction peak)	60			Effect of N ₂ concentration on structural, optical and mechanical properties of deposited films.

Authors	Substrate	Sputtering type	Substrate temperature C	Pressure (mTorr)	Base pressure (mbar)	Nitrogen %	Power	Total Gas sccm	Distance between substrate (cm)	FWHM	Deposition rate (nm/min)	Thickness (µm)	Surface roughness nm	Notes
Benetti, et al. [51] (2006)	Diamond	RF magnetron sputtering	200-500	3		100	500		5	0.4 (FWHM of Diffraction peak)				Effect of sputtering temperature
Kar, et al. [52] (2006)	Si(100)	RF magnetron reactive sputtering	200	4.5	3e-6	80	400		5		5.5		2.4	Effect of nitrogen concentration of film quality
Umeda, et al. [53] (2006)	Si(100)	RF magnetron sputtering	200	1.5	1e-6	70	1300-1800	60	5	1.4and 2.1 (FWHM of Rocking Curve)			1.7	Effect of sputtering parameters on residual stress
Guo, et al. [54] (2006)	Sapphire	RF magnetron sputtering	100	5	1e-7	40	100-250	9			8		6	Effect of sputtering power
Medjani, et al. [55] (2006)	Si(100)	RF magnetron sputtering	room, 400,800	3.75	4e-9	14	150	18	6.5					Effect of substrate temperature and bias voltage on the crystallite orientation
Vergara, et al. [56] (2006)	Si(100)	RF magnetron sputtering	900-1300	6.75	2.5e-7	50								Effect of rapid thermal annealing on piezoelectric response
Kar, et al. [57] (2006)	P-type Si(100)	RF magnetron sputtering	100-400	4.5	3e-6	80	400		8				2	Role of sputtering temperature
Jang, et al. [58] (2006)	P-type Si	RF magnetron sputtering	300	2-5.25	6.6e-5		100							Effect of rapid thermal annealing in oxygen ambient

Authors	Substrate	Sputtering type	Substrate temperature C	Pressure (mTorr)	Base pressure (mbar)	Nitrogen %	Power	Total Gas sccm	Distance between substrate (cm)	FWHM	Deposition rate (nm/min)	Thickness (µm)	Surface roughness nm	Notes
Kar, et al. [59] (2005)	Silicon, copper, quartz	RF magnetron reactive sputtering	200	4.5	3e-6	80	400		5	0.25 (FWHM of Diffraction peak)			2.1-3.68	Influence of rapid thermal annealing on morphological and electrical properties
Iriarte, et al. [60] (2005)		Pulse DC magnetron sputtering		2	6.6e-8	70	900		5.5	1.3 (FWHM of Rocking Curve)				Comparison of metallic substrate on crystal orientation
Zhang, et al. [61] (2005)	Si (100), Si 111)	RF magnetron sputtering	350	6	3.7e-7	100	500		8					Effect of sputtering power on crystal quality and strain in film
Sanz-Hervas, et al. [62] (2005)	Al, SiO ₂ , Cr, Mo and Ti	RF reactive sputtering		7		50	800							Effect of substrate bias on crystal quality

i. Process pressure

According to the kinetic theory of molecular gases, the mean free path of a gas molecule is inversely proportional to the pressure at constant temperature. In other words, a low process pressure maintains a high particle energy, resulting in high adatoms mobility, which then translates into high growth of AlN (002) films [63]. On the contrary, it was reported that when the sputtering pressure increases, the collision between sputtering particles and Ar ions led to the formation of AlN (100) films [64].

In one study, Cherng et al. [45] utilized multistep deposition pressures to enhance the quality of deposited AlN on Si (100) using pulsed DC reactive sputtering. They used a smaller pressure of 0.8 mTorr for initial nucleation for 10 minutes. Afterwards, a second step was done at 2 mTorr, 3.3 mTorr, and 4.6 mTorr respectively. They observed that the two-step sputtering shows a better figure of merit compared to the one step method, which resulted in smaller FWHM of the rocking curve as well as the smaller magnitude of residual stress. The value of stress decreased from -926 MPa to -317 MPa and with a constant deposition rate of about 36 nm/min.

Kar et al. [65] investigated the effect of sputtering pressure on the crystal orientation and the morphological properties of deposited AlN on a p-type Si substrate in the range of 1.5 to 6 mTorr. They observed the successful deposition of AlN (002) film until 4.5 mTorr. They further observed that the crystal orientation changed to (100) with a further increase of deposition pressure to 8 mTorr. The surface roughness increased from 1.56 nm to 3.24 nm with an increase in sputtering pressure. Also, the grain size of the deposited film rises to 114 nm until the 4.5 mTorr deposition pressure, but then decreased to 80 nm at 6 mTorr.

There are two more works that are worth mentioning. Atul Vir Singh et al. [39] reported an increase in deposition rate with an increase in sputtering pressure over different substrates (Glass, Si, oxidized Si, Al–SiO₂–Si, Cr–SiO₂–Si, and Au–Cr–SiO₂–Si). They varied the sputtering pressure from 5, 10, and 20 mTorr and concluded that low pressure was favourable for the highly crystalline c-axis oriented AlN. Chiu et al. [48] observed that deposition rate increased with the decrease in pressure due to the increased of the sputtered particles. They theorised that the FWHM values decreased at low pressure because the adatoms had more kinetic energy to settle in the close (002) plane.

ii. Sputtering power

The kinetic energy of the sputtering particle is directly proportional to the sputtering power. The latter enhances the energy of adatoms, so that they move to the lowest energy state and arrange themselves along the c-axis orientation. Various research groups employed high deposition power at low deposition pressure to achieve AlN (002) film. The power ranges from 100 W to 5.5 KW. However, several groups demonstrated that the high power can negatively affect the quality of c-axis orientation because of an increase in the kinetic energies of the secondary atoms. These atoms attacked the substrate surface, causing surface damage and prompting deterioration in the preferred c-axis orientation [66].

The sputtering power also depends on the substrate to target distance and the type of sputtering system. Lower power is needed for shorter distance. A low sputtering power in the range of 300 W to 500 W is typically used in RF sputtering, while a high power in the range of 1000 W to 1800 W is typically employed in D.C. sputtering.

In one published work, Kusaka et al. [43, 66] employed D.C. magnetron sputtering on a glass substrate to deposit AlN films at a constant N₂ gas pressure at various sputtering powers. They observed that the grain size and the crystal quality improve with increasing power. Further, they noted that tensile stresses were obtained at low input power, while large compressive stresses were achieved at high powers.

Vashaei et al. [43] varied RF power and base pressure from 250 W to 900 W and 4–20 mTorr, respectively. The substrate temperature was set from 200 °C to 400 °C. They reported an improvement in crystal quality and deposition rate with an increase in nitrogen concentration and RF power. This result is supported by Cheng et al. [63]. They concluded that higher power, shorter substrate-to-target distance, lower sputtering pressure, and lower N₂ ratio were the formula to form AlN (002) film.

Another group, Guo et al. [54] investigated the effect of RF power on the deposition rate, surface roughness, and optical transmittance (transmittance is the fraction of incident light of a specific wavelength which passes via a sample over a specific range of wavelength) of AlN films. The deposition rate and the surface roughness increased and decreased, respectively with the increase in RF power. They also reported that the absorption edge of AlN films shifts to longer wavelengths with an increase in RF sputtering power and was attributed to the defects induced by highly energetic ion bombardment, that is directly related to the sputtering power.

Kumada et al. [67] studied the impact of sputtering power on the shift in AlN crystal orientation. In their experiment using RF sputtering, they varied the power from 200 to 900 W in steps of 100 W and at 50 % Nitrogen concentration. AlN (101) and (002) poly crystals were obtained between 200-600 W power, while AlN (002) film were obtained starting from 700 W power.

A Berkeley group i.e. Lin et al. [68] used a two-steps deposition method to obtain highly c-axis oriented AlN thin films on epitaxial 3C-SiC/Si (100) substrate. The first 50-nm-nucleation layer was deposited with high nitrogen concentration with an AC power of 3 kW. The second step used 5.5 kW. They obtained AlN (002) film with the lowest FWHM rocking curve values of 1.73°.

iii. N₂ to Ar ratio

There are two opposite theories to explain the need for higher or lower N₂/Ar ratio to grow AlN (002) film. During the sputtering process, plasma state is created around the target. This plasma is composed of electrons, argon and nitrogen atoms, divalent nitrogen molecules, and argon and nitrogen ions. The positive ions, N₂⁺ and Ar⁺ are attracted towards the substrate. Due to its heavier atomic mass, Ar⁺ transfers more kinetic energy to the target and generates more Al atoms. Hence, the ejected Al particles have higher kinetic energy. That increases the adatoms' mobility on the surface of the growing films, so they can arrange themselves along the (002) orientation [63]. An increase of nitrogen concentration lowers the kinetic energy of sputtered ions because of the N₂⁺ lower atomic mass. These scattered ions undergo more scattering due to the increased probability of collision between the sputtered particles and nitrogen atoms. Hence, the adatoms' mobility decreases, and they arrange themselves into a loosely packed crystal orientations such as the (100) orientation [69].

Zhong et al. also reported the strong influence of the N₂ concentration on the AlN films. They reported a decrease in the diffraction peak amplitude in (002) with an increase in the N₂ concentration. The FWHM rocking curve values also increased from 2.02 to 3 with an increase in N₂ concentration from 25 % to 75% [70]. Clement et al. [71] also reported similar results. The XRD spectra shows that (002) was more predominant at 15 % N₂. The (002) diffraction peak amplitude decreased with an increase in Nitrogen concentration, and the amplitude of the other diffractions peaks such as (102) and (101) was increased.

Lui et al. [69] studied the effect of nitrogen concentration in the range of 20 % to 80 %. They reported a FWHM value of 3.1° at 20 % and 40 % Nitrogen concentration that

increase dramatically to 7.41° with further increase in nitrogen concentration. They also observed that the intensity of the (002) peak decreased significantly when the nitrogen concentration was in the range of 60–100 %.

There is a contradictory theory. Some groups achieved highly c-axis oriented AlN at higher N_2 concentration. According to them, the deposition rate has a strong effect on the crystal orientation. At higher N_2 to Ar ratio, the deposition rate is low because of the lower number of argon ions in the plasma. This provides a longer time interval for the Al atoms to react with N_2 and arrange themselves with previously synthesized AlN grains to form the (002) plane. At lower N_2 to Ar ratio, higher deposition rate is achieved. Therefore, the faster arrival of the Al atoms at the surface results in weak AlN bonding [52, 66].

There are many supporters of this contradictory theory. Kale et al. [52] studied the effect of nitrogen concentration on AlN crystal orientation. They reported that at low N_2 concentration, a strong (100) peak with a minor peak of (110) was observed. The increase in nitrogen concentration enhanced the (002) orientation. After 50% nitrogen concentration, the films are fully (002) oriented.

Another proponent of the second theory is Kar et al. [29]. They studied the effect of nitrogen concentration on grain growth, structural, and electrical properties of AlN films. They varied the nitrogen concentration from 20% to 80%. At 20 % N_2 , the (100) orientation was prominent compared to (002). The trend reverses, and highly oriented (002) peak dominated around 80 % N_2 .

Xiangquan Jiao et al. [24] RF sputtered AlN films on various substrates such as Si (100), Si (111), oxidized Si (SiO_2), and amorphous Si (a-Si). The concluded that SiO_2 was the most appropriate candidate for the growth of well-textured AlN thin films. They observed that the sputtering at 150 W and 75 % concentration yielded the strongest (002) crystal peak on SiO_2 .

iv. Substrate temperature and annealing

The substrate temperature influences the kinetic energy available to the adatoms on the surface of the substrate. As mentioned previously, higher kinetic energy assists in the deposition of highly c-axis oriented films [31, 72]. However, increasing the substrate temperature also has a negative effect. Because the substrate material differs from AlN, this results in higher coefficient of thermal expansion (CTE) difference between the two layers. This translates as thermal stresses, which deteriorates the film quality [73].

The effect of substrate temperature on AlN orientation has been reported by numerous groups. They deposited c-axis oriented AlN from room temperature to 650 °C. Jie Yang et al. [25] deposited AlN on a Mo buffer layer utilizing DC and RF sputtering. The main aim was to study the effect of substrate temperature on the crystal orientation of AlN and the film's morphology. They carried out the sputtering at the following substrate temperatures: 20 °C, 200 °C, 400 °C, and 600 °C. As the deposition temperature increased from 20 °C, the crystal orientation changes from (101) to (002) at 400 °C. When the substrate temperature was further increased to 600 °C, the intensity of the AlN (0002) peak decreased. They also observed changes in surface morphology. The AlN deposited at 20 °C exhibited irregular granular grains, while at 400 °C, only spherical grains were observed.

Another group studied the effect of substrate temperature on deposition rate and the crystal orientation. Hao Jin et al. [31] deposited AlN thin films by DC magnetron sputtering onto a Si(100) substrate. They used a substrate temperature of 60 °C, 160 °C, 250 °C, 340 °C, 430 °C, and 520 °C. The deposition rate increased from 60 °C to 250 °C and saturates afterwards (21.78 nm/min). However, the deposition rate does not decrease monotonically above 250 °C. The XRD results showed that the highest peak of the (002) orientation was observed at 430 °C. The intensity of the AlN (002) peak decreased afterwards.

Medjani et al. [55] investigated the combined effect of substrate temperature and substrate bias. They deposited AlN films on Si (100) by R.F. magnetron sputtering by varying the deposition temperature (from 25 °C to 800 °C) and bias voltage (from 0 V to -100 V). It was found that the lower substrate temperature and moderate bias voltage helps in the formation of the (002) plane. A bias voltage smaller than -75 V and a deposition temperature of 400 °C resulted in the growth of the (100) plane.

Guo et al. [74] studied the effect substrate temperature on the surface roughness. They sputtered c-axis oriented AlN using the R.F. sputtering at a substrate temperature of 100 °C and a nitrogen concentration of 20%. They observed that the surface roughness increased linearly with substrate temperature and nitrogen concentration.

One group performed post-annealing treatment. Kar et al. [59] increased the annealing temperature from 400 °C to 1000 °C in steps of 200 °C. They observed that the intensity of AlN (002) diffraction peak increased until 800 °C, and then marginally decreased at 1000 °C. They also reported a small shift in the XRD diffraction peaks at higher temperatures, due to

the residual stress during thermal annealing. Also, the surface roughness (in rms) increased from 2.1 nm to 3.68 nm at annealing temperature of 400 °C to 1000 °C, respectively.

v. Film Thickness:

The good lattice matching between the substrate and the deposited thin film is beneficial for AlN crystal growth along the c-axis orientation. Numerous research groups have successfully deposited c-axis oriented AlN on a broad range of materials such Si (100), Si (111), titanium, molybdenum, aluminium, c-sapphire, aluminium oxide, microcrystalline diamond, glass, silicon dioxide, copper, silicon carbide, chromium and so on. The majority of the commonly used substrates have a large lattice mismatch with AlN, which affects the crystal quality. In thin films, the large lattice mismatch leads to the large misfit strain that is inversely proportional to the film thickness, and deteriorates the crystal quality. However, as the film thickness increases, the large lattice mismatch has less impact on the crystal quality. The misfit strain decreases with an increase in film thickness that reduces the effect of large lattice mismatch [75].

Martin et al. [76] investigated the influence of AlN film thickness on its properties. They deposited AlN of thickness from 35 nm to 2 μm, on top of Pt (111) electrodes. They reported the FWHM of the rocking curve decreased from 2.60 to 1.14°, the RMS roughness was increased from 3.8 to 18.6 Å and the effective piezoelectric coefficient (namely $d_{33,f}$) increased from 2.75 to 5.15 pm/V.

Molleja et al. [26] investigated the role of AlN film thickness on crystal quality and residual stress. The FWHM of the diffraction peak indicating a (002) orientation decreased from 0.8 to 0.19 when the thickness was increased from 80 nm to 1.5 μm. They further reported that the thinner film had compressive stresses, while the thicker ones ($> 0.9 \mu\text{m}$) had tensile stress. Madrid et al. [30] supported Molleja's group result by using the FWHM of the rocking curve measurement.

Ababneh et al. [41] studied the effect of film thickness on the values of d_{33} and d_{31} piezoelectric coefficient. They noticed that by increasing the AlN film thickness from 600 nm to 2400 nm, the values for the d_{33} and d_{31} increases from 3.0 and -1.0 pm/V to 5.0 and -1.8 pm/V, respectively. The values for the thicker film were close to the d_{33} and d_{31} values of bulk AlN.

vi. Target- substrate distance

The target-substrate distance plays a role in obtaining c-axis oriented films. According to the Kinetic theory of molecular gases, the sputtering parameters have a direct impact on the mean free path (λ) of particles which directly influences the crystal orientation of deposited films. In the case of a smaller distance between the target and the substrate (D) compared to mean free path (λ) of the particles, the sputtering particles reach the substrate with higher kinetic energy and adatom mobility. The lower number of collisions because of less collisions with other particles, that assists them to align along the (002) orientation. On the other hand, when the distance between the target and the substrate (D) is larger compared to the mean free path (λ) of particles, most of the sputtering particles collide one or many times with other particles before reaching the substrate. Thus, the kinetic energy and adatom mobility of the sputtered particles would decrease and the particles will align them along other crystal orientations.

A target to substrate distance in the range of 5 cm to 25 cm was used by different research groups. The smaller distance is used in a low deposition power system. Most of the groups used the target to substrate distance in the range of 3 cm to 8 cm for a sputtering power in the range of 300 W to 1000 W.

Xiao-Hong et al. [77] deposited AlN on Si (111) substrates using DC sputtering. They studied the effects of the sputtering pressure, sputtering power, and target to the substrate distance on the crystal orientation of the AlN films. The distance between the substrate to target was varied from 3cm to 12 cm. They reported that a lower sputtering pressure and shorter distance helped to form the (002) plane. On the contrary, a higher sputtering pressure and longer distance are beneficial for the growth of the (100) plane. The findings from this group was supported by another works by Chen et al. [78], as well as Cheng et al. [63].

vii. Substrate bias voltage

At low sputtering pressure, highly oriented AlN thin films can be obtained without substrate bias. The substrate bias is also normally used to increase the deposition rate. However, a higher substrate bias can also result in stress at the film–substrate interface and other crystal orientations such as (100) or (101), which will diminish the coupling coefficient of an electro-acoustic devices.

In some work, the substrate voltage is used to tune the intrinsic stress of the film. This is because the energy of the depositing species is proportional to the bias voltage. Figure 5 illustrates this. The ions normally have low energy in case of no voltage bias at the substrate, which results in intrinsic tensile stress. In the case of substrate bias, the ions have higher energy, which generates a compressive stress in the thin films.

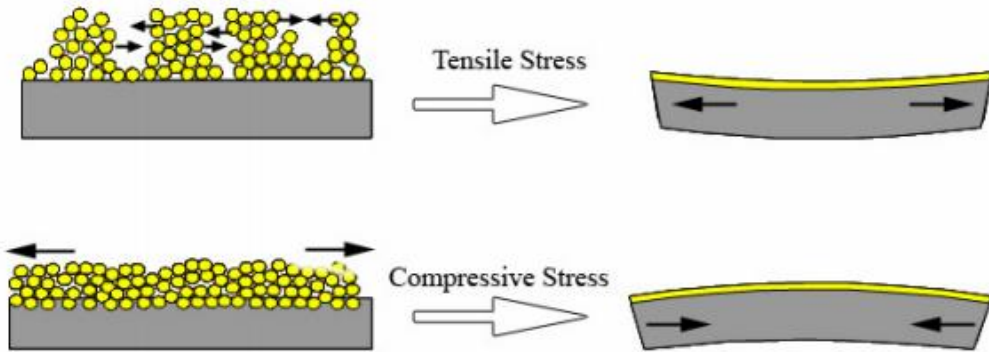


Fig 5: Types of stress within a thin film coating.

Medjani et al. [55] studied the deposition of AlN on Si (100) substrates by RF sputtering under various substrate negative bias V_s (0 up to -100 V) and deposition temperature (25 °C up to 800 °C). They observed that lower deposition temperature and moderate bias favour the formation of (002) planes. Further, strong biasing beyond -75 V and deposition temperature higher than 400 °C led to the growth of the (100) plane.

Chu et al. [79] RF sputtered AlN thin films on glass substrates at room temperature. They applied different negative bias voltage from 0 V to 320 V. The XRD diffraction showed a (002) oriented AlN up to -210 V. Afterwards, small diffraction peaks of AlN (002) and (100) planes were observed starting at a bias voltage of -240 V. The (002) plane vanished at the bias voltage of -320 V.

There is one group who reported contradictory results on substrate bias effect. Iborra et al. [80] applied a bias voltage from -14 V to -28 V on the substrate. The XRD diffraction results showed that high bias voltage of larger than -24 V is required to achieve purely (002) oriented films. Prior to this value, the (102) and (103) diffraction peaks were more dominant.

viii. Base pressure

In general, a low base pressure is essential to obtain a high-quality film. Al has high affinity for the oxygen, which in turn degrades the crystalline quality of AlN. It is observed that low base pressure minimizes the oxygen content in the chamber. Many groups have used a base pressure of 3.6×10^{-3} to 3.6×10^{-7} Torr for the deposition of AlN. The effects of outgassing on the deposition of AlN using pulsed-DC reactive sputtering of highly (002) oriented AlN thin film was conducted by Cherng et al. [47]. They studied the effect of outgassing by pumping down the system into the base pressure of 3×10^{-6} Torr, 1×10^{-6} Torr and 4×10^{-7} Torr before admitting the gas mixture into the chamber. Outgassing is the desorption of gases/ vapors from the vacuum surfaces in the absence of deliberately injected gas that results in unavoidable contamination at the time of films sputtering. They observed that outgassing was directly related to the base pressure and at lower base pressure, the sputtering parameters become less efficient on both rocking curve width and residual stress because of less contamination.

ix. Pre-Sputtering

The pre-sputtering is performed to remove impurities that are present in the target, substrate and the chamber. A pure aluminium target is normally used for reactively sputtering AlN films. This target oxidizes over time, producing a thin layer of aluminium oxide (Al_2O_3) on the target's surface. Furthermore, impurities can also be deposited on the target's surface during sputtering. Pre-sputtering is crucial to remove these oxide layer and other impurities.

VI. Conclusion:

The sputtering parameters and their roles in depositing c-axis oriented AlN films have been explained in this chapter. These relationships are derived by analysing 50 journal articles that reports c-axis AlN sputtering on a wide variety of substrates and equipment. Several general guidelines have been established towards this goal. First, the process pressure should be lower than 4 mTorr. Second, the sputtering power should be between 300 to 500 W for R.F. system and between 1k to 1.8 kW for D.C. system. Third, the N_2/Ar ratio should be over 50 %. Fourth, the substrate temperature should be in a range of 300 to 400 degree Celsius. Fifth, the film's thickness should be over 1 um. Sixth, the target to substrate distance should be

between 3 to 8 cm. Seventh, the substrate voltage bias should be 0 or smaller than -75 V. Eighth, the base pressure should be lower than 3.6×10^{-7} Torr.

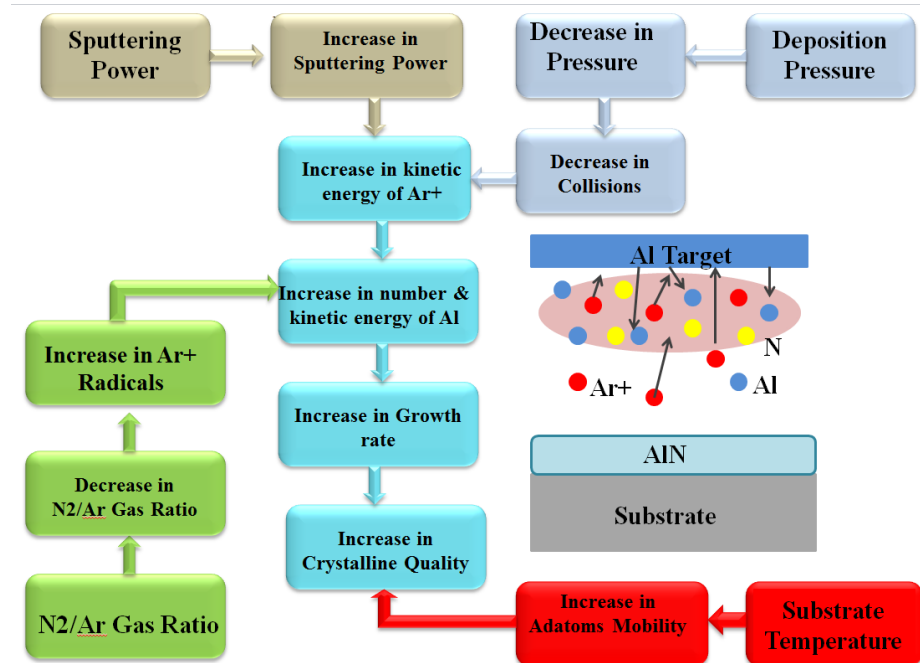


Fig 6: Flow chart on the role of sputtering parameters towards depositing c-axis AlN

Figure 6 shows the flow chart depicting the relationship between all sputtering parameters and the goal of growing a highly c-axis AlN film. The kinetic energy and adatom mobility on the surface of the substrate are used as the supporting physics to explain the relationships. Other items of the flow chart are self-explanatory. There are two main points. First, all these parameters alter the kinetic energy and the surface mobility of the adatoms, which ultimately arrange themselves along specific crystal orientations. Second, the net energy of adatoms is dependent on all the sputtering parameters. This value will be shifted by varying one or more parameters. Therefore, it is important to finely tune the sputtering recipe to achieve the right balance.

References:

- [1] S. Roundy, P. K. Wright, and J. M. Rabaey, *Energy scavenging for wireless sensor networks*: Springer, 2003.
- [2] N. E. Dutoit, B. L. Wardle, and S.-G. Kim, "Design considerations for MEMS-scale piezoelectric mechanical vibration energy harvesters," *Integrated Ferroelectrics*, vol. 71, pp. 121-160, 2005.
- [3] K. Cook-Chennault, N. Thambi, and A. Sastry, "Powering MEMS portable devices—a review of non-regenerative and regenerative power supply systems with special emphasis on piezoelectric energy harvesting systems," *Smart Materials and Structures*, vol. 17, p. 043001, 2008.
- [4] D. Isarakorn, A. Sambri, P. Janphuang, D. Briand, S. Gariglio, J. Triscone, *et al.*, "Epitaxial piezoelectric MEMS on silicon," *Journal of Micromechanics and Microengineering*, vol. 20, p. 055008, 2010.
- [5] H. Kim, S. Priya, H. Stephanou, and K. Uchino, "Consideration of impedance matching techniques for efficient piezoelectric energy harvesting," *IEEE transactions on ultrasonics, ferroelectrics, and frequency control*, vol. 54, pp. 1851-1859, 2007.
- [6] H.-B. Fang, J.-Q. Liu, Z.-Y. Xu, L. Dong, D. Chen, B.-C. Cai, *et al.*, "A MEMS-based piezoelectric power generator for low frequency vibration energy harvesting," *Chinese Physics Letters*, vol. 23, pp. 732-734, 2006.
- [7] E. Iborra, J. Olivares, M. Clement, L. Vergara, A. Sanz-Hervás, and J. Sangrador, "Piezoelectric properties and residual stress of sputtered AlN thin films for MEMS applications," *Sensors and Actuators A: Physical*, vol. 115, pp. 501-507, 2004.
- [8] M.-A. Dubois and P. Muralt, "Measurement of the effective transverse piezoelectric coefficient e_{31} of AlN and Pb(Zr x , Ti $1-x$)O 3 thin films," *Sensors and Actuators A: Physical*, vol. 77, pp. 106-112, 1999.
- [9] R. Elfrink, T. Kamel, M. Goedbloed, S. Matova, D. Hohlfeld, Y. Van Andel, *et al.*, "Vibration energy harvesting with aluminum nitride-based piezoelectric devices," *Journal of Micromechanics and Microengineering*, vol. 19, p. 094005, 2009.
- [10] S. E. Boeshore, *Aluminum nitride thin films on titanium: piezoelectric transduction on a metal substrate*: ProQuest, 2006.
- [11] E. Ruiz, S. Alvarez, and P. Alemany, "Electronic structure and properties of AlN," *Physical Review B*, vol. 49, p. 7115, 1994.

- [12] V. Cimalla, J. Pezoldt, and O. Ambacher, "Group III nitride and SiC based MEMS and NEMS: materials properties, technology and applications," *Journal of Physics D: Applied Physics*, vol. 40, p. 6386, 2007.
- [13] M. E. Levinshtein, S. L. Rumyantsev, and M. S. Shur, *Properties of Advanced Semiconductor Materials: GaN, AlN, InN, BN, SiC, SiGe*: John Wiley & Sons, 2001.
- [14] J. H. Edgar, "Properties of group III nitrides," *Institution of Electrical Engineers*, 1994.
- [15] T. Suetsugu, T. Yamazaki, S. Tomabechi, K. Wada, K. Masu, and K. Tsubouchi, "AlN epitaxial growth on atomically flat initially nitrided α -Al₂O₃ wafer," *Applied surface science*, vol. 117, pp. 540-545, 1997.
- [16] A. Iqbal, K. Chaik, G. Walker, A. Iacopi, F. Mohd-Yasin, and S. Dimitrijev, "RF sputtering of polycrystalline (100),(002), and (101) oriented AlN on an epitaxial 3C-SiC (100) on Si (100) substrate," *Journal of Vacuum Science & Technology B*, vol. 32, p. 06F401, 2014.
- [17] M. Ohtsuka, H. Takeuchi, and H. Fukuyama, "Effect of sputtering pressure on crystalline quality and residual stress of AlN films deposited at 823 K on nitrided sapphire substrates by pulsed DC reactive sputtering," *Japanese Journal of Applied Physics*, vol. 55, p. 05FD08, 2016.
- [18] G. Stan, M. Botea, G. Boni, I. Pintilie, and L. Pintilie, "Electric and pyroelectric properties of AlN thin films deposited by reactive magnetron sputtering on Si substrate," *Applied Surface Science*, vol. 353, pp. 1195-1202, 2015.
- [19] J. Wang, Q. Zhang, G. Yang, C. Yao, Y. Li, R. Sun, *et al.*, "Effect of substrate temperature and bias voltage on the properties in DC magnetron sputtered AlN films on glass substrates," *Journal of Materials Science: Materials in Electronics*, vol. 27, pp. 3026-3032, 2016.
- [20] X. Jiao, Y. Shi, H. Zhong, R. Zhang, and J. Yang, "AlN thin films deposited on different Si-based substrates through RF magnetron sputtering," *Journal of Materials Science: Materials in Electronics*, vol. 26, pp. 801-808, 2015.
- [21] X. Bi, Y. Wu, J. Wu, H. Li, and L. Zhou, "A model for longitudinal piezoelectric coefficient measurement of the aluminum nitride thin films," *Journal of Materials Science: Materials in Electronics*, vol. 25, pp. 2435-2442, 2014.
- [22] W.-C. Shih, Y.-C. Chen, W.-T. Chang, C.-C. Cheng, P.-C. Liao, and K.-S. Kao, "Design and fabrication of nanoscale IDTs using electron beam technology for high-frequency SAW devices," *Journal of Nanomaterials*, vol. 2014, p. 2, 2014.

- [23] C. Stoeckel, C. Kaufmann, R. Hahn, R. Schulze, D. Billep, and T. Gessner, "Pulsed DC magnetron sputtered piezoelectric thin film aluminum nitride—Technology and piezoelectric properties," *Journal of Applied Physics*, vol. 116, p. 034102, 2014.
- [24] X. Jiao, Y. Shi, H. Zhong, R. Zhang, and J. Yang, "AlN thin films deposited on different Si-based substrates through RF magnetron sputtering," *Journal of Materials Science: Materials in Electronics*, pp. 1-8, 2014.
- [25] J. Yang, X. Jiao, R. Zhang, H. Zhong, Y. Shi, and B. Du, "Growth of AlN Films as a Function of Temperature on Mo Films Deposited by Different Techniques," *Journal of Electronic Materials*, vol. 43, pp. 369-374, 2014.
- [26] J. García Molleja, B. J. Gómez, J. Ferrón, E. Gautron, J. Bürgi, B. Abdallah, *et al.*, "AlN thin films deposited by DC reactive magnetron sputtering: effect of oxygen on film growth," *The European Physical Journal Applied Physics*, vol. 64, p. 20302, 2013.
- [27] L. Monteagudo-Lerma, S. Valdueza-Felip, A. Núñez-Cascajero, M. González-Herráez, E. Monroy, and F. Naranjo, "Two-step method for the deposition of AlN by radio frequency sputtering," *Thin Solid Films*, vol. 545, pp. 149-153, 2013.
- [28] K. A. Aissa, A. Achour, J. Camus, L. Le Brizoual, P.-Y. Jouan, and M.-A. Djouadi, "Comparison of the structural properties and residual stress of AlN films deposited by dc magnetron sputtering and high power impulse magnetron sputtering at different working pressures," *Thin Solid Films*, vol. 550, pp. 264-267, 2014.
- [29] A. Kale, R. Brusa, and A. Miotello, "Structural and electrical properties of AlN films deposited using reactive RF magnetron sputtering for solar concentrator application," *Applied Surface Science*, vol. 258, pp. 3450-3454, 2012.
- [30] J. Rodríguez-Madrid, G. Iriarte, D. Araujo, M. Villar, O. A. Williams, W. Müller-Sebert, *et al.*, "Optimization of AlN thin layers on diamond substrates for high frequency SAW resonators," *Materials Letters*, vol. 66, pp. 339-342, 2012.
- [31] H. Jin, B. Feng, S. Dong, C. Zhou, J. Zhou, Y. Yang, *et al.*, "Influence of Substrate Temperature on Structural Properties and Deposition Rate of AlN Thin Film Deposited by Reactive Magnetron Sputtering," *Journal of electronic materials*, vol. 41, pp. 1948-1954, 2012.
- [32] A. Ababneh, M. Alsumady, H. Seidel, T. Manzaneque, J. Hernando-García, J. Sánchez-Rojas, *et al.*, "c-axis orientation and piezoelectric coefficients of AlN thin films sputter-deposited on titanium bottom electrodes," *Applied Surface Science*, vol. 259, pp. 59-65, 2012.

- [33] L. García-Gancedo, Z. Zhu, E. Iborra, M. Clement, J. Olivares, A. Flewitt, *et al.*, "AlN-based BAW resonators with CNT electrodes for gravimetric biosensing," *Sensors and Actuators B: Chemical*, vol. 160, pp. 1386-1393, 2011.
- [34] D.-T. Phan and G.-S. Chung, "The effect of geometry and post-annealing on surface acoustic wave characteristics of AlN thin films prepared by magnetron sputtering," *Applied Surface Science*, vol. 257, pp. 8696-8701, 2011.
- [35] A. V. Singh, S. Chandra, A. Srivastava, B. Chakroborty, G. Sehgal, M. Dalai, *et al.*, "Structural and optical properties of RF magnetron sputtered aluminum nitride films without external substrate heating," *Applied Surface Science*, vol. 257, pp. 9568-9573, 2011.
- [36] A. M. Cardenas-Valencia, S. Onishi, and B. Rossie, "Single-crystalline AlN growth on sapphire using physical vapor deposition," *Physics Letters A*, vol. 375, pp. 1000-1004, 2011.
- [37] G. Iriarte, D. Reyes, D. González, J. Rodriguez, R. García, and F. Calle, "Influence of substrate crystallography on the room temperature synthesis of AlN thin films by reactive sputtering," *Applied Surface Science*, vol. 257, pp. 9306-9313, 2011.
- [38] M. Moreira, I. Doi, J. Souza, and J. Diniz, "Electrical characterization and morphological properties of AlN films prepared by dc reactive magnetron sputtering," *Microelectronic Engineering*, vol. 88, pp. 802-806, 2011.
- [39] A. V. Singh, S. Chandra, and G. Bose, "Deposition and characterization of c-axis oriented aluminum nitride films by radio frequency magnetron sputtering without external substrate heating," *Thin Solid Films*, vol. 519, pp. 5846-5853, 2011.
- [40] B. Subramanian, V. Swaminathan, and M. Jayachandran, "Micro-structural and optical properties of reactive magnetron sputtered Aluminum Nitride (AlN) nanostructured films," *Current Applied Physics*, vol. 11, pp. 43-49, 2011.
- [41] A. Ababneh, U. Schmid, J. Hernando, J. Sánchez-Rojas, and H. Seidel, "The influence of sputter deposition parameters on piezoelectric and mechanical properties of AlN thin films," *Materials Science and Engineering: B*, vol. 172, pp. 253-258, 2010.
- [42] G. Stan, I. Pasuk, A. Galca, and A. Dinescu, "HIGHLY TEXTURED (001) AlN NANOSTRUCTURED THIN FILMS SYNTHESIZED BY REACTIVE MAGNETRON SPUTTERING FOR SAW AND FBAR APPLICATIONS," *Digest Journal of Nanomaterials & Biostructures (DJNB)*, vol. 5, 2010.

- [43] Z. Vashaei, T. Aikawa, M. Ohtsuka, H. Kobatake, H. Fukuyama, S. Ikeda, *et al.*, "Influence of sputtering parameters on the crystallinity and crystal orientation of AlN layers deposited by RF sputtering using the AlN target," *Journal of Crystal Growth*, vol. 311, pp. 459-462, 2009.
- [44] M. Clement, J. Olivares, E. Iborra, S. González-Castilla, N. Rimmer, and A. Rastogi, "AlN films sputtered on iridium electrodes for bulk acoustic wave resonators," *Thin Solid Films*, vol. 517, pp. 4673-4678, 2009.
- [45] J. Cherng, C. Lin, and T. Chen, "Two-step reactive sputtering of piezoelectric AlN thin films," *Surface and Coatings Technology*, vol. 202, pp. 5684-5687, 2008.
- [46] B. Abdallah, C. Duquenne, M. Besland, E. Gautron, P. Jouan, P. Tessier, *et al.*, "Thickness and substrate effects on AlN thin film growth at room temperature," *The European Physical Journal Applied Physics*, vol. 43, pp. 309-313, 2008.
- [47] J. Cherng and D. Chang, "Effects of outgassing on the reactive sputtering of piezoelectric AlN thin films," *Thin solid films*, vol. 516, pp. 5292-5295, 2008.
- [48] K.-H. Chiu, J.-H. Chen, H.-R. Chen, and R.-S. Huang, "Deposition and characterization of reactive magnetron sputtered aluminum nitride thin films for film bulk acoustic wave resonator," *Thin Solid Films*, vol. 515, pp. 4819-4825, 2007.
- [49] K. Kano, K. Arakawa, Y. Takeuchi, M. Akiyama, N. Ueno, and N. Kawahara, "Temperature dependence of piezoelectric properties of sputtered AlN on silicon substrate," *Sensors and Actuators A: Physical*, vol. 130, pp. 397-402, 2006.
- [50] S. Venkataraj, D. Severin, R. Drese, F. Koerfer, and M. Wuttig, "Structural, optical and mechanical properties of aluminium nitride films prepared by reactive DC magnetron sputtering," *Thin Solid Films*, vol. 502, pp. 235-239, 2006.
- [51] M. Benetti, D. Cannata, F. Di Pietrantonio, E. Verona, A. Generosi, B. Paci, *et al.*, "Growth and characterization of piezoelectric AlN thin films for diamond-based surface acoustic wave devices," *Thin solid films*, vol. 497, pp. 304-308, 2006.
- [52] J. Kar, G. Bose, and S. Tuli, "Influence of nitrogen concentration on grain growth, structural and electrical properties of sputtered aluminum nitride films," *Scripta materialia*, vol. 54, pp. 1755-1759, 2006.
- [53] K. Umeda, M. Takeuchi, H. Yamada, R. Kubo, and Y. Yoshino, "Improvement of thickness uniformity and crystallinity of AlN films prepared by off-axis sputtering," *Vacuum*, vol. 80, pp. 658-661, 2006.
- [54] Q. Guo, T. Tanaka, M. Nishio, and H. Ogawa, "Growth properties of AlN films on sapphire substrates by reactive sputtering," *Vacuum*, vol. 80, pp. 716-718, 2006.

- [55] F. Medjani, R. Sanjines, G. Allidi, and A. Karimi, "Effect of substrate temperature and bias voltage on the crystallite orientation in RF magnetron sputtered AlN thin films," *Thin Solid Films*, vol. 515, pp. 260-265, 2006.
- [56] L. Vergara, J. Olivares, E. Iborra, M. Clement, A. Sanz-Hervás, and J. Sangrador, "Effect of rapid thermal annealing on the crystal quality and the piezoelectric response of polycrystalline AlN films," *Thin Solid Films*, vol. 515, pp. 1814-1818, 2006.
- [57] J. Kar, G. Bose, and S. Tuli, "Correlation of electrical and morphological properties of sputtered aluminum nitride films with deposition temperature," *Current Applied Physics*, vol. 6, pp. 873-876, 2006.
- [58] K. Jang, K. Lee, J. Kim, S. Hwang, J. Lee, S. K. Dhungel, *et al.*, "Effect of rapid thermal annealing of sputtered aluminium nitride film in an oxygen ambient," *Materials science in semiconductor processing*, vol. 9, pp. 1137-1141, 2006.
- [59] J. Kar, G. Bose, and S. Tuli, "Influence of rapid thermal annealing on morphological and electrical properties of RF sputtered AlN films," *Materials science in semiconductor processing*, vol. 8, pp. 646-651, 2005.
- [60] G. F. Iriarte, J. Bjurstrom, J. Westlinder, F. Engelmark, and I. V. Katardjiev, "Synthesis of c-axis-oriented AlN thin films on high-conducting layers: Al, Mo, Ti, TiN, and Ni," *Ultrasonics, Ferroelectrics, and Frequency Control, IEEE Transactions on*, vol. 52, pp. 1170-1174, 2005.
- [61] J. Zhang, H. Cheng, Y. Chen, A. Uddin, S. Yuan, S. Geng, *et al.*, "Growth of AlN films on Si (100) and Si (111) substrates by reactive magnetron sputtering," *Surface and Coatings Technology*, vol. 198, pp. 68-73, 2005.
- [62] A. Sanz-Hervas, L. Vergara, J. Olivares, E. Iborra, Y. Morilla, J. Garcia-Lopez, *et al.*, "Comparative study of c-axis AlN films sputtered on metallic surfaces," *Diamond and related materials*, vol. 14, pp. 1198-1202, 2005.
- [63] H.-E. Cheng, T.-C. Lin, and W.-C. Chen, "Preparation of [002] oriented AlN thin films by mid frequency reactive sputtering technique," *Thin Solid Films*, vol. 425, pp. 85-89, 2003.
- [64] H. Cheng, Y. Sun, J. Zhang, Y. Zhang, S. Yuan, and P. Hing, "AlN films deposited under various nitrogen concentrations by RF reactive sputtering," *Journal of crystal growth*, vol. 254, pp. 46-54, 2003.
- [65] J. Kar, G. Bose, and S. Tuli, "A study on the interface and bulk charge density of AlN films with sputtering pressure," *Vacuum*, vol. 81, pp. 494-498, 2006.

- [66] K. Kusaka, D. Taniguchi, T. Hanabusa, and K. Tominaga, "Effect of input power on crystal orientation and residual stress in AlN film deposited by dc sputtering," *Vacuum*, vol. 59, pp. 806-813, 2000.
- [67] T. Kumada, M. Ohtsuka, K. Takada, and H. Fukuyama, "Influence of sputter power and N₂ gas flow ratio on crystalline quality of AlN layers deposited at 823 K by RF reactive sputtering," *physica status solidi (c)*, vol. 9, pp. 515-518, 2012.
- [68] C.-M. Lin, W.-C. Lien, T.-T. Yen, V. V. Felmetser, D. G. Senesky, M. A. Hopcroft, *et al.*, "Growth of highly c-axis oriented AlN films on 3C-SiC/Si substrate," in *Tech. Dig. Solid-State Sens. Actuators Microsystems Workshop*, 2010, pp. 324-327.
- [69] H. Liu, G. Tang, F. Zeng, and F. Pan, "Influence of sputtering parameters on structures and residual stress of AlN films deposited by DC reactive magnetron sputtering at room temperature," *Journal of Crystal Growth*, vol. 363, pp. 80-85, 2013.
- [70] H. Zhong, Z. Xiao, X. Jiao, J. Yang, H. Wang, R. Zhang, *et al.*, "Residual stress of AlN films RF sputter deposited on Si (111) substrate," *Journal of Materials Science: Materials in Electronics*, vol. 23, pp. 2216-2220, 2012.
- [71] M. Clement, E. Iborra, J. Sangrador, A. Sanz-Hervás, L. Vergara, and M. Aguilar, "Influence of sputtering mechanisms on the preferred orientation of aluminum nitride thin films," *Journal of applied physics*, vol. 94, pp. 1495-1500, 2003.
- [72] W.-J. Liu, S.-J. Wu, C.-M. Chen, Y.-C. Lai, and C.-H. Chuang, "Microstructural evolution and formation of highly c-axis-oriented aluminum nitride films by reactively magnetron sputtering deposition," *Journal of crystal growth*, vol. 276, pp. 525-533, 2005.
- [73] G. Iriarte, J. Rodriguez, and F. Calle, "Synthesis of c-axis oriented AlN thin films on different substrates: A review," *Materials Research Bulletin*, vol. 45, pp. 1039-1045, 2010.
- [74] Q. Guo, M. Yoshitugu, T. Tanaka, M. Nishio, and H. Ogawa, "Microscopic investigations of aluminum nitride thin films grown by low-temperature reactive sputtering," *Thin Solid Films*, vol. 483, pp. 16-20, 2005.
- [75] J.-M. Myoung, W.-H. Yoon, D.-H. Lee, I. Yun, S.-H. Bae, and S.-Y. Lee, "Effects of thickness variation on properties of ZnO thin films grown by pulsed laser deposition," *Japanese journal of applied physics*, vol. 41, p. 28, 2002.

- [76] F. Martin, P. Muralt, M.-A. Dubois, and A. Pezous, "Thickness dependence of the properties of highly c-axis textured AlN thin films," *Journal of Vacuum Science & Technology A*, vol. 22, pp. 361-365, 2004.
- [77] X.-H. Xu, H.-S. Wu, C.-J. Zhang, and Z.-H. Jin, "Morphological properties of AlN piezoelectric thin films deposited by DC reactive magnetron sputtering," *Thin Solid Films*, vol. 388, pp. 62-67, 2001.
- [78] Y. Chen, R. Wang, B. Wang, T. Xing, X. Song, M. Zhu, *et al.*, "Effects of mean free path on the preferentially orientated growth of AlN thin films," *Journal of crystal growth*, vol. 283, pp. 315-319, 2005.
- [79] A. Chu, C. Chao, F. Lee, and H. Huang, "Influences of bias voltage on the crystallographic orientation of AlN thin films prepared by long-distance magnetron sputtering," *Thin Solid Films*, vol. 429, pp. 1-4, 2003.
- [80] E. Iborra, M. Clement, J. Sangrador, A. Sanz-Hervás, L. Vergara, and M. Aguilar, "Effect of particle bombardment on the orientation and the residual stress of sputtered AlN films for SAW devices," *Ultrasonics, Ferroelectrics, and Frequency Control, IEEE Transactions on*, vol. 51, pp. 352-358, 2004.

Chapter 3: RF Sputtering of Polycrystalline (100), (002) and (101) Oriented AlN on an Epitaxial 3C-SiC (100) on Si(100) Substrate

This chapter is the following paper:

Iqbal, A., Chaik, K., Walker, G., Iacopi, A., Mohd-Yasin, F., & Dimitrijev, S. (2014). RF sputtering of polycrystalline (100),(002), and (101) oriented AlN on an epitaxial 3C-SiC (100) on Si (100) substrate. *Journal of Vacuum Science & Technology B*, 32(6), 06F401.

RF sputtering of polycrystalline (100), (002) and (101) oriented AlN on an epitaxial 3C-SiC (100) on Si(100) substrate

Queensland Micro- and Nanotechnology Centre, Griffith University, Brisbane QLD 4111, Australia

Abstract:

In this paper, the RF sputtering of polycrystalline AlN thin film on epitaxial 3C-SiC(100) on Si(100) substrate is presented. The effect of nitrogen concentration, deposition temperature, and sputtering pressure are studied. These parameters are optimized to improve the crystal quality and deposition rate. Nitrogen concentration was varied from 40 % to 100 %, and it was found that the maximum deposition rate was observed at 40 %. The RF bias power on the substrate was also varied from 100 W to 400 W, and it was observed that the deposition rate increases proportionally. The process temperature was varied from 200-400⁰C to see the effect on the crystal quality and deposition rate; it was found that temperature variation doesn't yield significant shifts. This paper can demonstrate a successful RF sputtering of a polycrystalline AlN (100), (101) and (002) on epitaxial 3C-SiC(100) using RF power supply of 550W.

1. INTRODUCTION

Silicon (Si) based micro-system cannot operate in extreme environments because its mechanical properties fail beyond 500⁰C¹. This is overcome by exploiting silicon carbide (SiC) material because, in addition to its ability to operate above 1000⁰C, it has other excellent mechanical and chemical properties such as extreme hardness, low-friction reducing mechanical wear-out and chemical inertness to corrosive atmospheres². For examples, SiC-based electric micromotors and micro jet-engine power generation sources show SiC's excellent durability where mechanical properties of Si are insufficient³. Another example is for the monitoring and controlling of the combustion engines to improve the fuel efficiency and pollution reduction, which can be conducted by SiC-based harsh environment sensors. One another example is on the development of catalytic metal-SiC and metal insulator- SiC prototype gas sensors for monitoring gas emission and fuel leakage detection⁴. It is very clear from these examples that the automobile and aircraft industries are looking into SiC for coming up with the solutions for their advanced systems. One pertinent question that still needs to be addressed for these future systems is their power supply. The conventional power system will not be able to withstand the extreme environment. Due to the vibratory natures of automotive and aircraft system, piezoelectric energy harvesting is one of the promising candidates to power up these systems in this particular environment.

Piezoelectric materials are available in different forms and are classified into four different types namely polycrystalline ceramics, single crystal material, polymer and thin film⁵. Thin film has a significant range of advantages such as low hysteresis, large deflections, high sensitivity and low power requirements. The selection of these piezoelectric thin film materials also depends on the deposition methods, process complexity and sensor networks node compatibility. The most common piezoelectric thin films are lead zirconate titanate (PZT), zinc oxide (ZnO) and aluminum nitride (AlN). PZT is a common piezoelectric material in energy harvesting applications because of its higher electromechanical coupling coefficient (k) and piezoelectric strain coefficient (d) over ZnO and AlN. However, the presence of lead, which is a hazardous material in PZT, causes contamination in the clean room and also it has low Curie temperature compared to AlN and ZnO. The second candidate, ZnO has better piezoelectric performances i.e. d and k over AlN. Unfortunately, its performance degrades at a higher temperature because of its low Curie temperature⁶ compared to AlN.

AlN is a material of great technological advantages in the microelectronics industry due to its wide bandgap (6.2 eV), high thermal conductivity ($3.3 \text{ WK}^{-1}\text{cm}^{-1}$) and high electrical resistivity ($10^{13} \Omega/\text{cm}$) for applications in high power electronics High-electron-mobility transistor (HEMTs) and optoelectronics (UV LEDs)⁷⁻⁸. The AlN's low permittivity is the key advantage over ZnO as it would allow for higher voltage generation⁹. Due to its comparatively high piezoelectric coefficient, the high acoustic velocity of 12,000 m/s and CMOS compatibility, AlN has been widely used in RF MEMS devices. The piezoelectric property of AlN remains same at high temperatures, thus coupling AlN and 3C-SiC for RF MEMS devices and piezo electric actuators can be made for harsh environment applications¹⁰.

Polycrystalline AlN thin films normally exhibit (002), (100), (101) and (103) oriented hexagonal wurtzite structure. The coupling coefficient of the (100)-oriented AlN thin films is larger than the AlN (002)-oriented thin films. However, AlN with (100) orientation is difficult to deposit using PVD methods¹¹. So generally, AlN (002) orientation is utilized for micro-piezoelectric devices. One of the major applications for the AlN (100), (002) and (101) is for surface acoustic wave (SAW) and bulk acoustic wave (BAW) devices. The (002) oriented AlN is used for longitudinal devices while (100) and (101) provides a pure fast shear mode and a quasi-longitudinal mode and a quasi-shear mode respectively¹¹.

AlN is typically grown on SiC or sapphire to decrease the crystal lattice mismatch. However, these substrates are expensive as compared to Si. The 47% difference in thermal expansion coefficient (TEC) between AlN and Si will generate disruptions and stresses, especially when thin composite structures have to work at very high temperature. One practical solution is to deposit AlN on top of cubic-silicon carbide (3C-SiC)-on-Si since the cost of fabricating the thin layer of 3C-SiC on the Si substrate reduces drastically. The lattice mismatch between AlN (002) orientation and 3C-SiC (100) is 28.6%, but the difference in thermal expansion coefficients is 18 %, which is much smaller than AlN/Si. In one such report¹², the AlN (001) film was grown on a silicon (111) substrate through hydride vapour epitaxy (HVPE) using 3C-SiC as an epitaxial layer. A smoother 5µm thickness of AlN was achieved using a 1 micron thick 3C-SiC intermediate layer, but the crystal quality of the AlN was not evaluated. One research group has successfully deposited AlN (002) film on a 4H-SiC (100) substrate for a SAW transducer¹³. The latest work performed by Lin et al.¹⁴, who deposited highly oriented AlN (002) films on 3C-SiC(100)/Si(100) substrates using AC reactive magnetron sputtering utilizing a very high (5.5 kW) and expensive pulsed power supply.

In this paper we present the successful deposition of polycrystalline AlN (100), (101) and (002) thin films on a doped n-type SiC(100)-on-Si (100) wafer using a typical RF magnetron sputtering system (Surrey sputterer) at the low power of 550W, and without an extra annealing process. RF sputtering is used for AlN deposition because the insulator like AlN deposition causes charge build-up on insulating targets due to DC voltage, which results in arcing on the targets. This can be avoided using an R.F. power supply, where the power is varied at a high rate, i.e. 13.56MHz. Alternatively, the arcing using DC sputtering can be decreased by utilizing a pulsed DC power supply, but the equipment is very expensive. The 250 nm thick AlN film is sputtered for 5 hours with three crystal orientations being able to be deposited successfully on epitaxial 3C-SiC (100) of 1µm thick on Si (100) substrate. The sputtering is done for 5 hours because the prolonged sputtering time results in the formation of particle dust which affects the growth of AlN on the substrate. The whole deposition process was divided into 30 minutes slots while 5 minutes pumping is used to pump the chamber to high vacuum before proceeding for further deposition. The concern of the large TEC mismatch between AlN and 3C-SiC (100) was remedied via optimizing the deposition condition at a low temperature of 300°C and low deposition power of 550 W. The effect of nitrogen concentration, deposition temperature, and sputtering pressure are optimized to improve the crystal quality and deposition rate.

2. Experimental Setup:

Aluminium Nitride is deposited using a physical vapor deposition (PVD) sputtering technique using a Surrey Nanosystems sputter (SNS) as shown in Fig 1. The SiC(100)/Si(100) samples of size 15mm by 15mm were prepared using a Dicso wafer dicer. The SiC(100) thin films are epitaxially deposited onto the Si (100) substrate in-house at the Griffith University. The samples are cleaned via the piranha cleaning process, which removes any organic substance that exists on the samples. A piranha clean was performed using 4 part of 98% H₂SO₄ (sulphuric acid) to 1 part of 30% H₂O₂ (Hydrogen Peroxide) at 90°C for 15 mins.

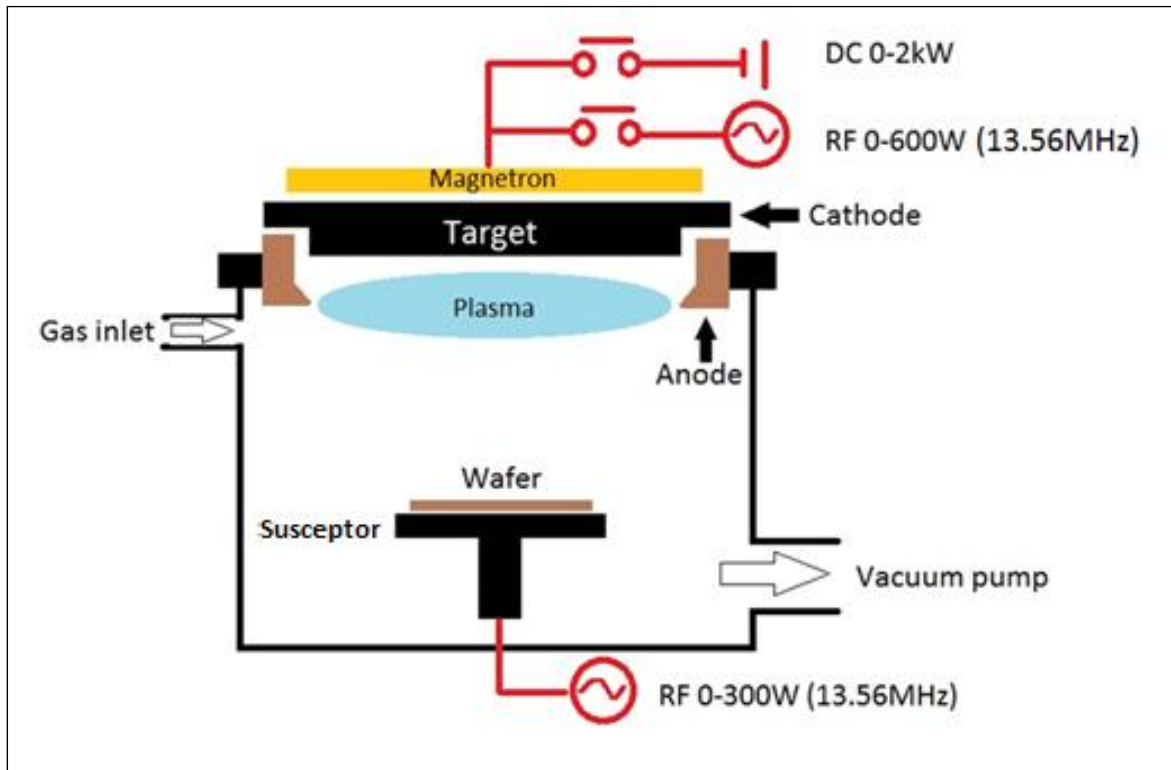


Fig 1 (Color online): Schematic of Nanosurrey PVD sputtering system

The samples were loaded into the loadlock of the two stage loading system of the SNS sputterer. The main chamber of the sputterer was constantly being pumped down to the limit of the cryogenic pump of the sputterer ($1\mu\text{Pa}$) to decrease the contamination. An argon purge process was introduced before the samples were loaded into the main chamber. It purged the main chamber with 15 sccm of 99.999% Ar gas for three mins, while the loadlock

was being pumped down by a turbo molecular pump to achieve low level vacuum. The samples were heated to 300°C with an IR heater for three mins after the low level vacuum is achieved in the loadlock, to remove any moisture on the sample to minimize contamination in the main chamber. The deposition conditions are shown in Table 1.

Table 1: AlN Deposition Parameters

Parameters	Values
Deposition Frequency	13.6 MHz
Ar flow rates	0 to 60 %
N2 flow rates	40 to 100 %
Target to substrate spacing	20 cm
RF power	550 W
Pressure	2 to 10 mTorr
Temperature	200 to 400 °C
Base Pressure	2×10^{-8} Torr
Deposition rate	5 to 9 Å/min

3. Optimization of Process Parameters and Observations

RF instead of DC sputtering is widely used to sputter insulating material, as the insulator causes charge build-up on an insulating target resulting in arcing. This can be avoided by using a RF power supply, where the power is varied at a high rate i.e. 13.56MHz. During RF sputtering, to sustain the plasma for the process, the susceptor (refer to Fig. 1) is R.F. biased, and the matching network for the power supply has to be reconfigured for every different process parameter. The base pressure is one of the important sputtering parameters which affect the crystal quality of AlN. It is observed that low base pressure results in high crystalline quality and vice versa. The low base pressure also prevents the incorporation of oxygen into the growing AlN thin film. Aluminum has a strong chemical affinity for oxygen for the formation of Al_2O_3 which retards the single grain columnar growth and leads to a poor preferred orientation. In our sputtering systems, we utilize the minimum base pressure of 2×10^{-8} Torr.

The decent lattice matches between the substrate and the deposited thin film play a vital role in crystal growth. The majority of the commonly used substrates have a large lattice

mismatch with AlN which affects the c-axis oriented crystal quality. Also, the surface roughness and the grain size influence the growth of AlN thin films. It is observed that a substrate surface roughness below 4nm_{rms} obtain high c-axis oriented AlN.

A. Etching of SiC/Si samples before AlN deposition

In-situ Argon plasma etching before the AlN deposition has been demonstrated to improve the crystal quality ¹¹. The etching rate of the SiC/Si samples were measured at 10 mTorr processing pressure, for 18 minutes. The result shows that the etch rate decreases with the increase of temperature. The etch rate for SiC is measured as 1.5nm/min at 350°C and 1.4nm/min at 500°C.

B. Reactive Mode at Various Deposition Pressures

The deposition of AlN is performed in reactive mode, which means the target is poisoned with the reactive gas to form a thin layer of compound on the surface before being sputtered off for deposition. To reach the reactive mode, the transition point from the metallic to the reactive modes was found by using a dummy wafer loaded into the loadlock, and standard pre-deposition steps are performed to maintain the quality control. Twenty experimental run were performed to figure out the transition point from metallic to reactive modes for AlN deposition at various sputtering pressures. The concentration of nitrogen gas at different base pressure for reaching the reactive mode is shown in Figure 2. The transition point is represented by the thick straight line. The result shows that the transition from the metallic mode to reactive mode sputtering occurs around 40% of the nitrogen concentration at the base pressure of 1 and 2 mTorr. As the base pressures increase to 5 and 10 mTorr, the transition point of the nitrogen concentration decrease to about 40%.

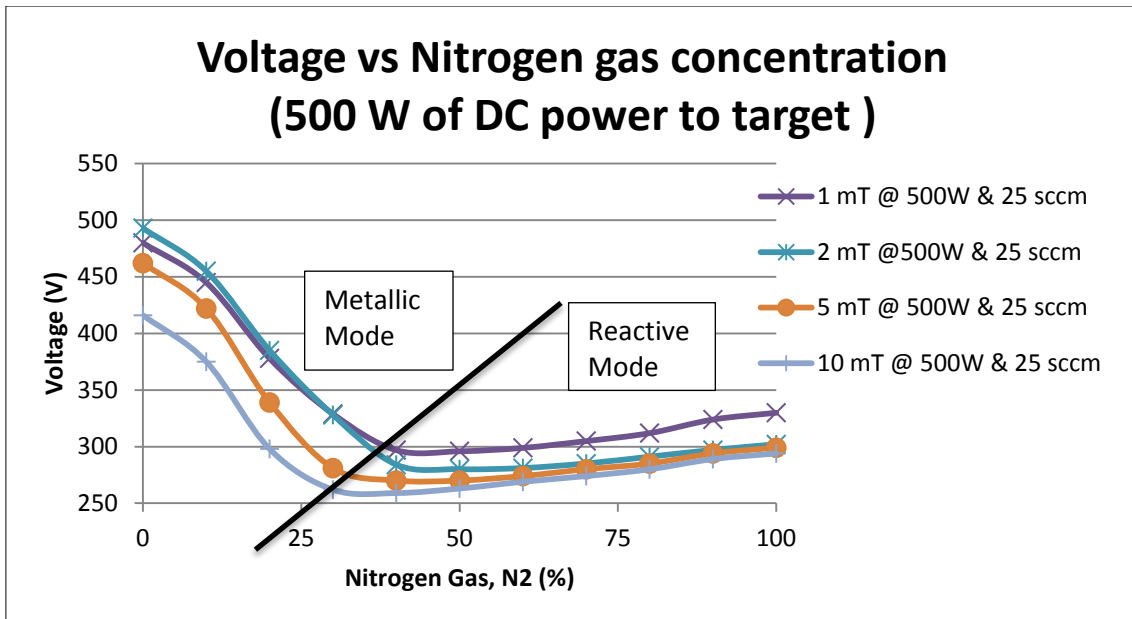


Figure 2 (Color online): Transition point from metallic to reactive modes for AlN deposition

C. The Effect of Nitrogen Concentration on the Deposition Rate and Crystal Quality

The nitrogen concentration plays an important role in determining the crystal quality and orientation of deposited AlN. The literature review shows that various groups have verified the deposition of c- axis oriented AlN at a nitrogen concentration of 30 %, 40 %, and 60 %.

In this work, the nitrogen concentration was varied from 40 % to 100 % to study the effect of nitrogen concentration on the deposition rate and crystal quality. The sputtering was carried out for 5 hours, and the thickness of deposited film is measured on a silicon wafer using an ellipsometer and nanospec. The nitrogen to argon ratio is chosen as 40 % for the starting point as it is the transition point from metallic to reactive modes. The data is plotted in Figure 3, where the base pressure is set at 10 mTorr and the RF power is set at 300W. The deposition rate is observed to be maximum at 40 % and decreasing onwards. In between 60 % to 90 % of the nitrogen concentration, the deposition rate is relatively constant. Afterwards, the increase in deposition rate is observed at 100 % concentration of Nitrogen.

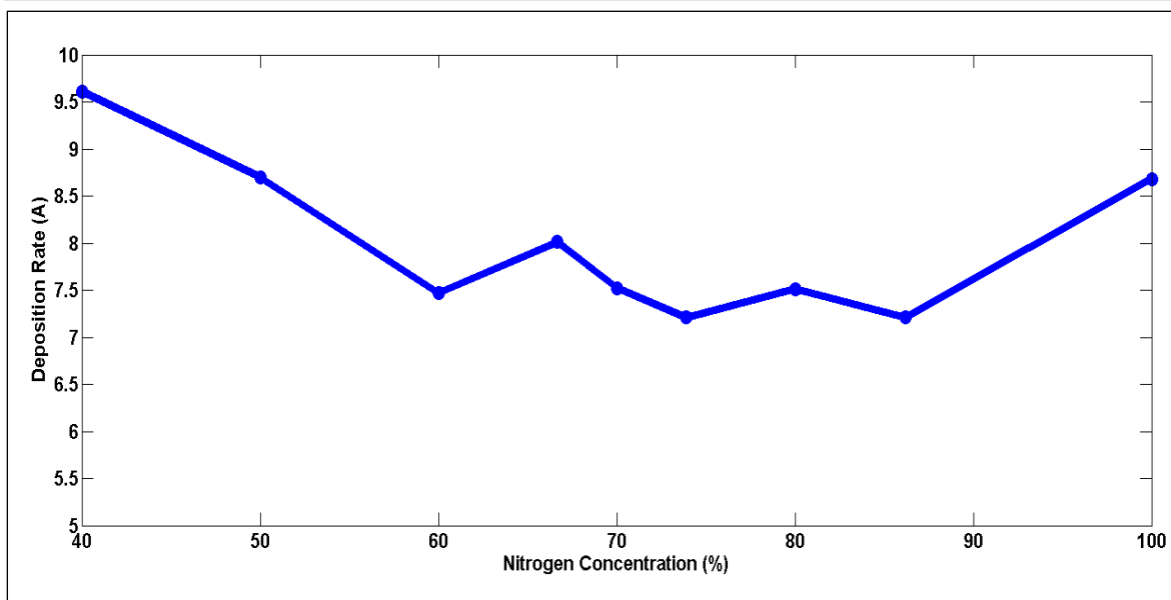


Figure 3: Deposition rate with nitrogen to argon ratio at 10 mTorr sputtering pressure and 300 W Rf power

Figure 4 shows the XRD result of the AlN deposition at different nitrogen concentration. The peak position in the XRD data indicates the phase or orientation of the material present in the sample, while the peak intensity quantifies the amount of each phase present in the sample. The peak width indicates the quality of each phase of material i.e. the sharper the peak is, then the smaller variation of the phase of the material. The 1^0 grazing angle XRD is utilized for the characterization of the deposited AlN thin film due to the small thickness of the film compared to the substrate. The XRD results show the (100), (002) and (101) crystal orientation of AlN at 2θ angles of 33° , 36° and 38° respectively, as can be observed in Fig 4. The maximum peak intensity of the AlN (002) is observed at 67% N_2 to argon ratio. The highly (100) oriented film was deposited at 40 % N_2 to Argon ratio. Also, the Al (101) orientation presents in all samples with relatively similar peaks regardless of the N_2 to Argon ratio, which can be observed in Fig 4.

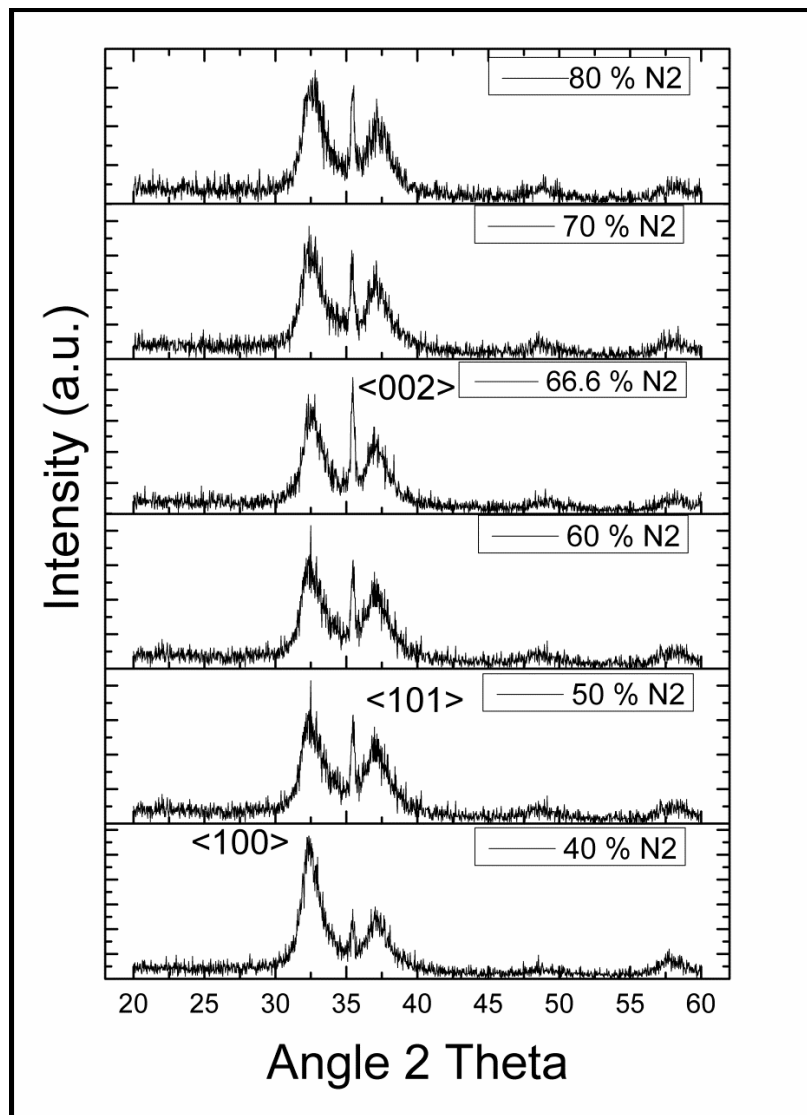


Figure 4: XRD result of AlN deposited with varying percentage of Nitrogen and Argon concentration at 10 mTorr pressure and 300 W RF power

D. The Effect of Deposition Pressure on Crystal Quality

The Kinetic theory of molecular gases states that the mean free path of a gas molecule is inversely proportional to the pressure at constant temperature. Thus the kinetic energy transfers from the plasma to the growing film surface increase with a decrease in pressure. Therefore the chance of getting better crystal deposition increases as the sputtering pressure decreases. Figure 5 shows the XRD data of AlN at different process pressures. As in Figure 4, the peaks of AlN (100), AlN (002) and AlN (101) are present in all the samples. It can be observed that the peak intensity of AlN (002) increases from the process pressure of 10 mTorr down to 3 mTorr, while the reverse is true for the other two AlN orientations.

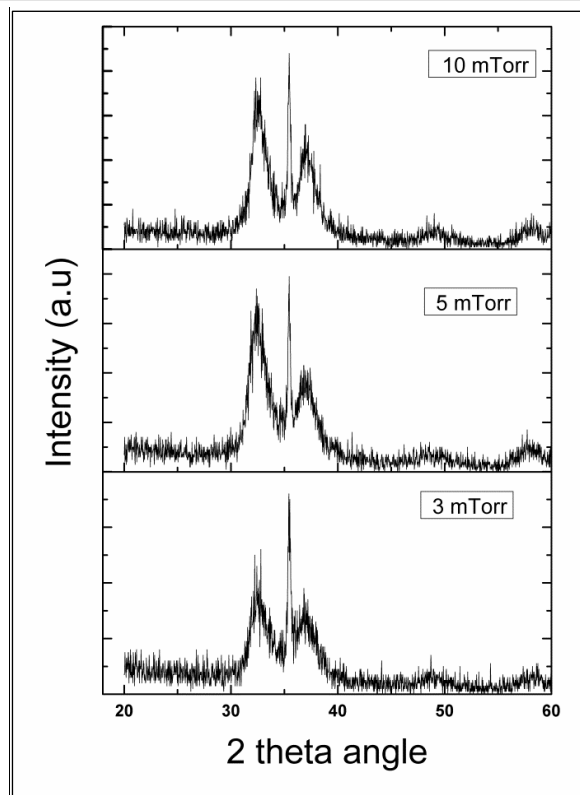


Figure 5: XRD result of AlN deposited at deposition pressure of 3mTorr, 5mTorr, and 10 mTorr pressures

E. Effect of Substrate Temperature and RF Power on Crystal Quality

The effect of substrate temperature on the AlN deposition has been studied by various researchers. The substrate temperature is varied from room temperature to 650°C . In this work, the substrate temperature is varied from $200\text{-}400^{\circ}\text{C}$. Figure 6 shows the XRD data of the AlN deposition at 300°C (blue line) and 400°C (cyan line). It is very clear that there is not much variation in term of the peak intensity of AlN (100), (002) and (101) at both temperatures. That is, temperature variation doesn't provide a significant effect on the crystal orientation.

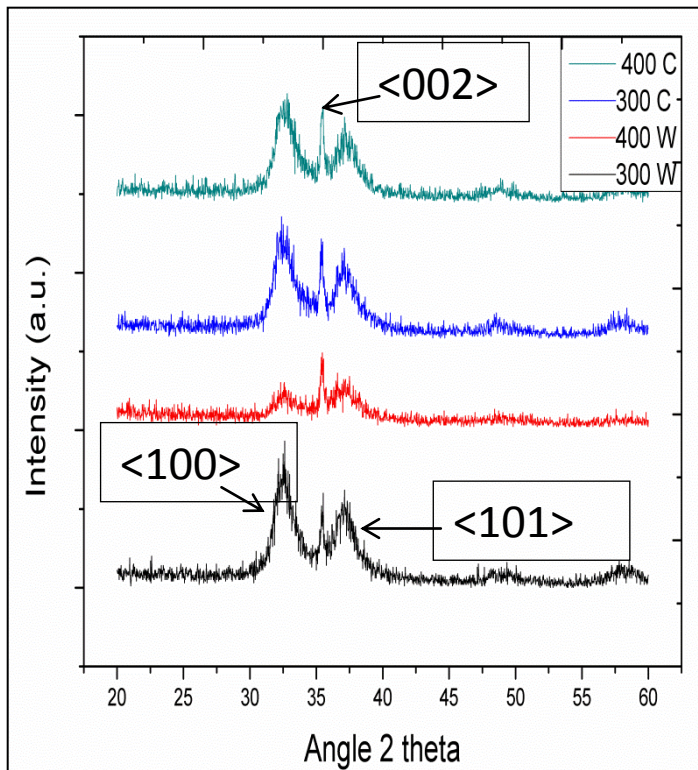


Figure 6 (Color online): XRD result of AlN deposited at 300 W and 400 W rf power and 300 °C and 400 °C substrate temperature

In this particular experiment, the RF bias has been varied from 300W to 400W to observe its effect on the deposition rate. The effect of varying the bias power on the deposition rate has been dramatic, where the latter film thickness decreased from 2609 Å to 1530 Å. The hypothesis is that the argons ions intensity striking at the deposited film is directly proportional to the bias power applied on the susceptor. The intensity of the argons ions sticking on the deposited films increases with an increase in bias voltage that decreases the deposition rate because of high number of Ar atoms sticking at the substrate. Conversely, the intensity of argon ions decreases with a decrease in bias voltage on the substrate that increases the deposition rate because of less number of Argon ions striking on the deposited film.

At the beginning of RF sputtering, it is found that 300W bias power provides the most stable plasma formation during the fabrication process. However, the XRD result shows that by increasing the bias power to 400W, it improves the crystal quality of AlN (002), where AlN (001) and AlN (101) peak intensities are relative lower compare to the other results as

can be observed in Figure 6. The red line represents the XRD data at 400W, and the black line represents the XRD data at 300W.

The AFM image of AlN deposited on 3C-SiC is shown in Figure 7. The mean square roughness rms of the 3C-SiC was measured as 4nm before AlN deposition while the mean square roughness rms value of the AlN layer is measured as 8 nm. Therefore, we can conclude that the 8 nm roughness of the AlN thin film is largely caused by the roughness of the epitaxial 3C-SiC layer beneath it.

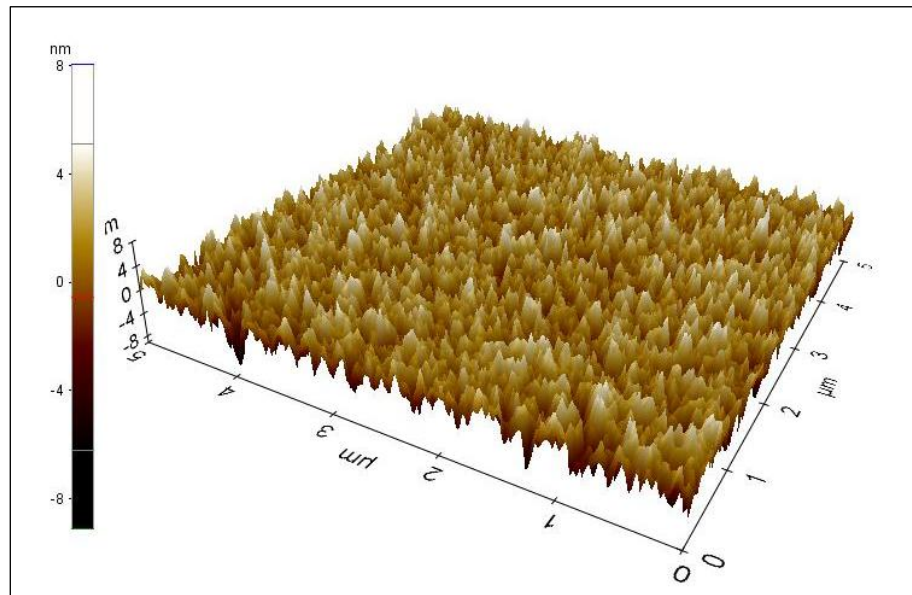


Figure 7: AFM of AlN sputtered on 3C- SiC presenting roughness of the deposited thin film

F. Refractive Index and Stress

The refractive index of the deposited samples is measured using ellipsometer. A wavelength of 632 nm is used for finding the refractive index and the thickness of the AlN deposited on a silicon wafer. The results show the variation of refractive index with nitrogen concentration as shown in Figure 8. The value of refractive index varies from 2.07 to 2.16 depending upon the nitrogen concentration. The theoretical value of refractive index for crystalline AlN is 2.14 at 632nm, which is close enough to our results. Since the theoretical refractive index of 3C-SiC and Si is 2.635 and 3.49 respectively at 632nm, we conclude that the range of 2.07-2.16 indeed belongs to AlN.

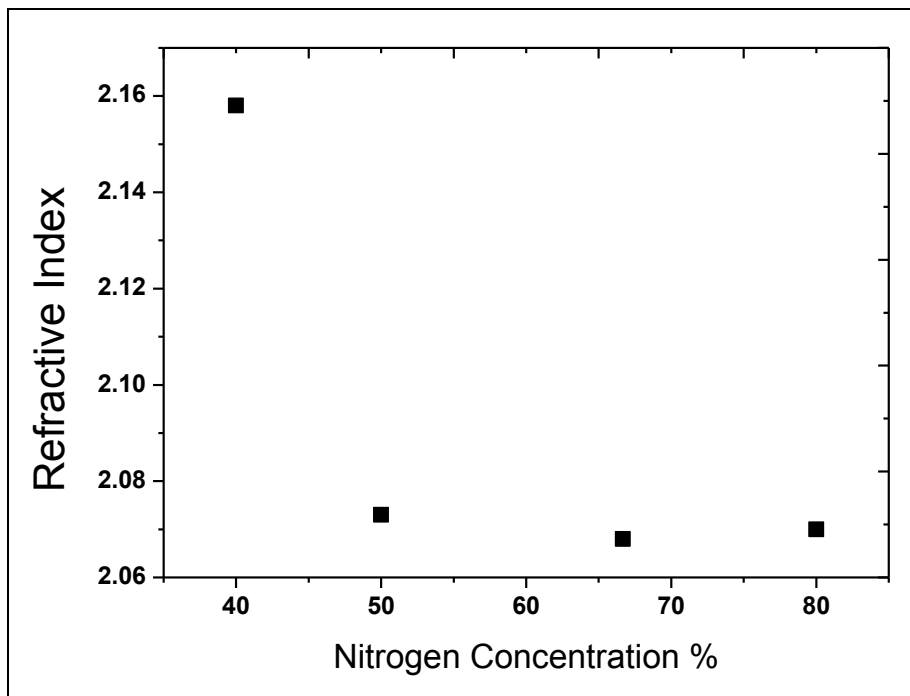


Figure 8: Refractive index of AlN deposited at 10 mTorr at various nitrogen to argon ratio

The residual stress of the deposited film was measured on the 2 inch Si (100) wafer using a Tencor Flexus 2320 system. The stress was then calculated according to the change in curvature using Stoney's equation.

$$\sigma = \frac{E}{6(1-\nu)} \frac{t_s^2}{t_f} \left(\frac{1}{r_c} - \frac{1}{r_u} \right)$$

where E, ν , t_s and t_f are the Young's modulus, Poisson's ratio for the silicon substrate, silicon thickness and film thickness respectively, while r_u and r_c are the radii of curvature of the Si substrates before and after AlN deposition, respectively. The residual stress is found to be 3.2 GPa and is compressive in nature for 100 W RF bias on the substrate. The value of the stress and its nature can be changed from tensile to compressive by modifying the RF biasing on the substrate from 0 W to 100 W.

4. Conclusion

The deposition of polycrystalline AlN (100), (101) and (002) thin film on a SiC (100) thin film as an intermediate layer on a Si (100) substrate is demonstrated using RF sputtering. Various parameters are optimized such as nitrogen concentration, substrate temperature, deposition pressure and RF power. The results revealed that the pressure, RF power, and

nitrogen concentration play an important role in AlN deposition which is revealed from XRD results. The N₂ to Argon ratio plays a vital role in crystal orientation. The (100) crystal orientation was prominent at 40 % N₂ to argon ratio while all other parameters were kept constant. The XRD results also show that (100), (002) and (101) oriented crystal orientation were present in all the samples deposited at different N₂ to argon ratio. Also, it is observed that the high flow rate of argon and nitrogen gases improves the deposition rate. The deposition temperature, however, doesn't play a significant role in increasing the crystal quality of any specific crystal orientation. In general, the low pressure and high RF power result in good AlN at all three orientations. Finally, the measurement of the refractive index verifies the deposition of polycrystalline AlN on the epitaxial 3C-SiC (100) on Si (100) substrate, which will be most useful for SAW and BAW applications.

ACKNOWLEDGMENTS

This work is supported by Queensland Micro- and Nanotechnology Centre (QMNC) and Griffith School of Engineering. This work was performed in part at the Queensland node of the Australian National Fabrication Facility, a company established under the National Collaborative Research Infrastructure Strategy to provide nano and microfabrication facilities for Australia's researchers.

References

- ¹D. Dondi, A. Bertacchini, D. Brunelli, L. Larcher and Luca Benini, IEEE Trans. Ind. Electron. **55**, 2759-2766, (2008)
- ²T. H. Lee, S. Bhunia, and M. Mehregany, Science **329**, 5997 (2010).
- ³A. H. Epstein, J. Eng. Gas. Turb. Power **126**, 205-226, (2004).
- ⁴G. W. Hunter, P. G. Neudeck, J. Xu, D. Lukco, A. Trunek, M. Artale, P. Lampard, MRS Proceedings **815**, J4-4. (2004).
- ⁵P. M. Sarro, Sens. Actuators, An **82**, 210-218, (2000).
- ⁶F. Engelmark, Fredrik, G. Fuentes, I. V. Katardjiev, A. Harsta, Ulf Smith, and Sören Berg, J. Vac. Sci. Technol., An **18**, 1609-1612, (2000).
- ⁷J. A. Ruffner, P. G. Clem, B. A. Tuttle, D. Dimos, and D. M. Gonzales, Thin Solid Films **354**, 256-261, (1999).

- ⁸A. Claudel, Y. Chowanek, E. Blanquet, D. Chaussende, R. Boichot, A. Crisci, G. Berthomé, Phys. Status Solidi A **8**, 2019-2021, (2011).
- ⁹D. Isarakorn, A. Sambri, P. Janphuang, D. Briand, S. Gariglio, J. M. Triscone, F. Guy, J. W. Reiner, C. H. Ahn, and N. F. de Rooij, J Micromech Microeng **20**, 055008, (2010).
- ¹⁰M. Ishihara, H. Yumoto, T. Tsuchiya, K. Akashi, J. Surf. Finish. Soc. Jpn. **47**, 152, (1996).
- ¹¹M.S. Lee, S. Wu, Z.-X. Lin, and R. Ro, Jpn. J. Appl. Phys. **46**, 6719, (2007).
- ¹²J. Komiyama, K. Eriguchi, Y. Abe, S. Suzuki, H. Nakanishi, T. Yamane, H. Murakami, and A. Koukitu, J. Cryst. Growth **310**, 96-100, (2008).
- ¹³Y. Takagaki, P. V. Santos, E. Wiebicke, O. Brandt, H-P. Schönherr, and K. H. Ploog, Appl. Phys. Lett. **81**, 2538-2540, (2002).
- ¹⁴Chih-Ming Lin, Wei-Cheng Lien, Valery V. Felmetsgger, Matthew A. Hopcroft, Debbie G. Senesky, and Albert P. Pisano, Appl. Phys. Lett. **97**, 141907-141907, (2010).

Chapter 4: Controlled Sputtering Of AlN (002) and (101) Crystal Orientations On Epitaxial 3C-SiC- On-Si (100) Substrate

This chapter is the following paper:

- **Iqbal, A.**, Walker, G., Iacopi, A., & Mohd-Yasin, F. (2016). Controlled sputtering of AlN (002) and (101) crystal orientations on epitaxial 3C-SiC-on-Si (100) substrate. *Journal of Crystal Growth*, 440, 76-80.

Controlled Sputtering of AlN (002) and (101) Crystal Orientations on Epitaxial 3C-SiC-on-Si (100) Substrate

A. Iqbal, G. Walker, A. Iacopi and F. Mohd-Yasin^{*1}

Queensland Micro- and Nanotechnology Centre, Griffith University, Nathan, 4111, Australia

Abstract

Aluminum Nitride (AlN) thin films are successfully deposited on epitaxial 3C-SiC-on-Si (100) substrates using DC magnetron sputtering. The sputtered films are characterized by the following parameters: crystal orientations (Siemens D500 X-Ray diffraction tool), deposition rate (Nanospec AFT 180), surface roughness (Park NX20 Atomic Force Microscopy), refractive index (Rudolph AutoEL IV Ellipsometer), in-plane stress (Tencor Flexus 2320 System) and Raman Spectra (Rennishaw InVia Spectrometer). XRD results demonstrate that the orientation of the AlN thin films can be changed from (002) to (101) by increasing the Nitrogen to Argon ratio from 40% to 80% at the total gas flow of 50 sccm. We are also able to tune the in-plane stress via RF biasing on the substrate. Both controlling abilities enable the applications of these thin films for low cost longitudinal piezoelectric devices and a quasi-shear mode devices using (002) and (101) orientations, respectively.

Keywords: A3. Physical vapor deposition processes; A3. Polycrystalline deposition; A1. X-ray diffraction; B1. Nitride; B1. Silicon carbide

1. INTRODUCTION

Thin film- instead of bulk-piezoelectric material is advantageous regarding higher sensitivity, lower hysteresis, larger mechanical deflections and lower power requirements. Lead zirconate titanate (PZT), zinc oxide (ZnO) and aluminum nitride (AlN) are the commonly used thin film materials for piezoelectric devices. PZT is the preferred choice because of its higher piezoelectric coefficient (e_{31} , -6.5C/m³), but it has the risk of contaminating the clean room during the deposition process. The piezoelectric coefficients of AlN and ZnO are comparatively similar i.e. (e_{31} , -0.58 C/m³) and (e_{31} , -0.57 C/m³), respectively.

Piezoelectric sensors are in great demand for use in ultra-high-temperatures (>800 °C), particularly in the automotive, aerospace, and energy industries. In automotive combustion systems, high temperature sensors are being used for recording engine temperature, pressure, and vibration to improve the efficiency and reliability of internal combustion engines. AlN is preferred for high temperature applications because of its high Curie temperature (1200 °C) [1], whereas the performance of the ZnO and PZT degrades significantly [2,3].

Also, AlN has a high figure of merit in term of piezoelectric coefficient per dielectric constant (e_{31}^2/ϵ_r) compared to PZT [3]. Also, the electromechanical coupling (k_2) along the c-

* Corresponding author. E-mail address: f.mohd-yasin@griffith.edu.au.

axis of wurzite AlN is highest for longitudinal deformation [4]. Moreover, the acoustic velocity for the SAW devices is at its maximum along the c-axis [5]. Due to these factors, highly c-axis oriented AlN thin films have been deposited by groups around the world using molecular beam epitaxy [6]-[7], chemical vapor deposition [8], vapor phase epitaxy[9]-[10], ion beam nitridation [11], pulsed laser deposition[12] and reactive sputtering [13]. The lattice matching between the chosen substrates and the deposited AlN thin film plays a vital role in the orientation of the crystal growth. AlN is mostly deposited on Silicon (Si) substrates due to a lower cost per surface unit than other substrates. However, the difference of 47% in the coefficient of thermal expansion (CTE) between AlN ($4.3 \times 10^{-6} \text{ K}^{-1}$)[108] and Si ($2.6 \times 10^{-6} \text{ K}^{-1}$)[14] generates thermal stresses and crystal defects when it is being cooled down from high deposition temperature. Therefore, several researchers investigated AlN growth on other substrates that have lower CTE difference, such as Si (111)[15], sapphire[16, 17], platinum [18, 19], silicon dioxide[20] and aluminum[21]. The best results were obtained using substrates with the closest lattice constant and CTE, namely Silicon carbide (SiC) (4.3596 \AA) and (0001) sapphire, where the latter has a lower lattice mismatch with AlN [22]. However, it has a higher cost per unit area compare to Si.

One practical solution is to deposit AlN on top of a few hundred nanometre thick cubic silicon carbide (3C-SiC) that has been epitaxially grown on Si substrate. The introduction of 3C-SiC intermediate (sometimes referred to as the pseudo) layer reduces the lattice and CTE mismatches between AlN and Si substrate to 28.6% and 18%, respectively. In one such work, an AlN (001) film of 5 microns was deposited on a 3C-SiC-on-Si (111) substrates employing hydride vapour epitaxy (HVPE)[14]. Lin et al. [15] deposited the highest crystal quality AlN (002) film on 3C-SiC-on-Si (100) substrates using reactive magnetron sputtering and achieved a rocking curve Full Width at Half Maximum (FWHM) value of 1.73° . However, the lowest rocking curve FWHM value ever recorded (1.22°) on a similar structures is by Nader et al. This group deposited AlN (002) thin films of 200 nm thickness on a 3C-SiC/Si(111) substrates at 720°C using plasma induced molecular-beam epitaxy (MBE) [23]. Even though MBE provides better crystal quality as compared to sputtering, these systems are being avoided in low cost applications because of low growth rate, expensive instrument setup and a high process temperature [24]. Also, sputtering method is preferred over MBE/MOCVD for AlN thin film application in MEMS because of its ability to tune the in-plane stress via RF biasing on the substrate [25].

Polycrystalline AlN thin films normally exhibit (100), (002), (101) and (103) oriented hexagonal wurtzite structures and are used for SAW and BAW devices. The (002) and (101) oriented AlN thin films are specifically used for longitudinal and quasi-shear mode devices, respectively [26]. In this paper, we present the controlled deposition of (002) and (101) oriented AlN thin film on 3C-SiC-on-Si (100) substrates. The 300 nm thick 3C-SiC(100) film had been epitaxially grown on top of 6 inch Si (100) wafer using a custom-made hot-wall horizontal low pressure chemical vapor deposition (LPCVD) at Griffith University [27]. The main contribution detailed in this paper is the ability to control the crystal orientations of AlN by varying N₂ concentrations. We can change the AlN orientation from (002) to (101) by increasing the Nitrogen to Argon ((N₂/Ar) ratio from 40 % to 80 % with a total gas flow of 50 sccm. We use DC magnetron sputtering because it yields a higher deposition rate compared to our previous work using RF magnetron sputtering[28].

2. Experimental Setup

We employed a D.C. magnetron sputtering system (Surrey NanoSystems Gama 1000) operating at 1200 W to deposit the AlN film on top of the 3C-SiC layer. The Al target was 100 mm in diameter with 99.999 % purity. The target to substrate distance was set to 20 cm. The 3C-SiC-on-Si samples of 15 mm by 15 mm were cut using a Dicso wafer dicer and cleaned via a standard piranha cleaning process to remove organic substances. The oxidation on the samples was removed by submerging it in diluted 1% HF acid for 5 minutes. The sputtering system was turbo-pumped down to the base pressure of 2×10^{-8} Torr, followed by constant pumping through the cryogenic pump. The low base pressure encouraged the formation of highly crystalline AlN by preventing the incorporation of oxygen into the growing AlN thin film. The main chamber was purged with 15 sccm of 99.999 % Ar gas for 3 minutes before the sample loading to avoid contamination. The samples were inserted into the main chamber via a two-stage loading system. The samples were heated to 300 °C with an IR heater for 3 minutes to remove moisture. The sputtering parameters used for the deposition of AlN are given in Table 1. The sputtering pressure was gradually decreased from 20 mTorr to 2 mTorr to avoid the electrical arcing. The N₂/Ar ratio is increased from 40 % to 100 % in a steps of 20 %, with a total gas at a flow rate of 50 sccm to evaluate the effect of N₂ concentration on the following criteria (name of equipment): crystal orientation (Siemens D500 X-Ray diffraction tool) , deposition rate (Nanospec AFT 180), surface roughness (Park NX20 Atomic Force Microscopy), refractive index (Rudolph AutoEL IV Ellipsometer), the

in-plane stress (Tencor Flexus 2320 System) and Raman spectroscopy (Renishaw InVia Spectrometer).

Table 1: AlN Deposition Parameters

Parameters	Values
Total Gas Flow	50 sccm
Ar flows rate	0 to 60 %
N ₂ flow rate	40 to 100 %
Target to substrate spacing	20 cm
DC power	1200 W
Pressure	2 mTorr
Base Pressure	2×10 ⁻⁸ Torr
Temperature	350 °C

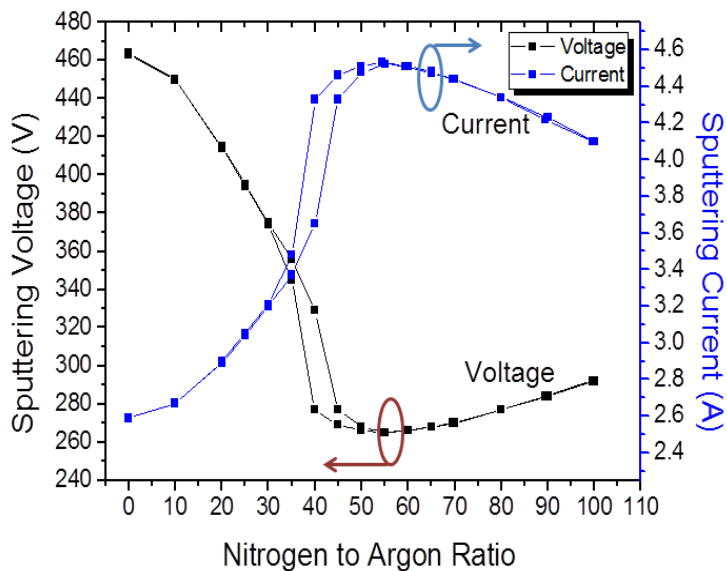


Fig. 1. Poison run for AlN deposition at 2mTorr and 350°C at 50 sccm total gas flow

The AlN was sputtered on top of the substrate in reactive mode. This mode was characterized via a parametric sweep of N₂/Ar ratio while keeping other sputtering parameters constant. The N₂ concentration was swept from 0 % to 100 % and back to 0 % at a flow rate of 50 sccm to measure the hysteresis 50. Fig. 1 shows the parametric sweep of the N₂/Ar ratio to get the voltage and current values for the transition from metal to reactive modes. The higher secondary electron emission of the nitride formed at the cathode surface pulled down the plasma impedance in the reactive mode, resulting in the drop of the cathode voltage at

constant DC power. The voltage then remained approximately the same in the reactive mode. We found that the transition from metal to reactive modes started at 40 % N₂/Ar ratio at 50 sccm total flow of gas. Overall, the deposition current increased from 2.6 A to 4 A, while the deposition voltage decreased from 420 V to 320 V.

3. Results and Discussion

A grazing angle incident X-Ray diffraction (GIXRD) measurement at 1° incidence was employed due to the smaller thickness of AlN film compared to the substrate using a Siemens D500 X-Ray diffraction tool. Figure 2 shows the θ-2θ scan of the four samples at the different N₂/Ar ratio. These X-Ray diffractometry (XRD) data verified the deposition of polycrystalline AlN films. The two major diffraction peaks could be observed at 36° and 38°, indicating (002) and (101) crystal orientations, respectively. The minor peaks at 34° and 50° refer to (100) and (102) orientations of AlN, respectively. The FWHM values were extracted from the diffraction peaks using Gaussian fitting instead of Lorentz fitting, as the former provides better curve fitting for all the curves [19, 26]. This particular technique of extracting the FWHM values from the diffraction peaks had been employed by three similar works on AlN [27-29]. We benchmark our FWHM data against these three. Our lowest FWHM value of 0.285° from the diffraction peaks of (002) crystal orientation at 40 % N₂/Ar ratio is comparable to the lowest FWHM values of 0.29°, 0.22° and 0.32° as reported in [30], [19] and [21], respectively. The values of FWHM from the diffraction peaks of the (002) crystal orientation then increased to 0.285° and 0.305° at 60 % and 80 % N₂/Ar ratio, respectively. On the other hand, the FWHM values of the diffraction peaks of the (101) crystal orientation decreased from 0.305° to 0.266° with an increase in N₂/Ar ratio from 40 % to 100 %. The result also shows that the diffraction peak intensity for the (002) crystal orientation decreased when the N₂/Ar ratio increased from 40 % to 100 %. On the other hand, the diffraction peak intensity of the (101) crystal orientation increases with increase in N₂/Ar ratio from 40 % to 100 %.

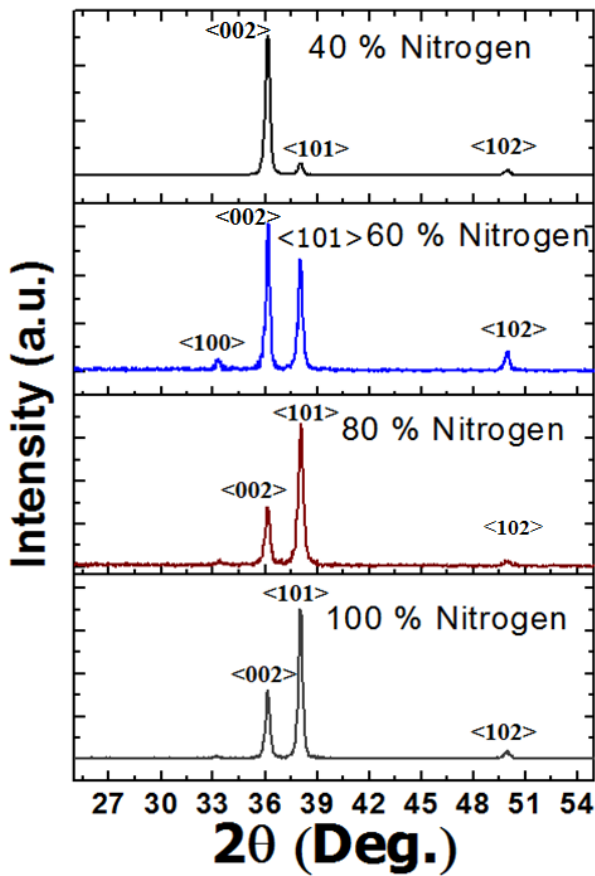


Fig. 2. Grazing angle XRD of AlN deposited on 3C-SiC/Si(100) film at different N_2/Ar ratio

The extracted FWHM values of the diffraction peaks provide evidence that the AlN orientation could be changed from (002) to (101) by increasing the N_2/Ar ratio in the total gas flow of 50 sccm. We attempt to explain this experimental observation as follows [16]. At lower N_2/Ar ratio, Ar+ dominates around the target. Ar+ has heavier atomic mass compare to N_2+ and thus produces larger kinetic energy adatoms, which resulted in the close packed (002) orientation. At 60 % N_2/Ar ratio, nitrogen particles (N_2+ , N_2 , N) with lighter atomic mass dominate and the Ar particle number decreases. Hence the kinetic energy of the adatoms decrease causing the formation of the dominant (1 0 1) and (0 0 2) orientations, and less prominent (100) and (102) mixed oriented films [17]. The kinetic energy of adatoms decreases further with an increase in N_2 concentration to 80 % and 100 %, which results in a more dominant (101) orientation compared to the (002) orientation in the deposited films.

The deposition rate of the AlN layer was determined by preparing separate samples of the sputtered AlN on top of a doped p-type Si (100) wafer using the non-contact, spectro-reflectometry, preprogrammed on Si, employing a Nanospec AFT 180 instrument. The

deposition rate of 8 nm/min was measured at 40 % N₂/Ar ratio. The deposition rate then decreased to 4.8 nm/min and remained the same at the higher N₂/Ar ratio. This is because of a decrease in the higher mass of the single-charged ion (i.e. Ar⁺) compared to the nitrogen particles (N₂⁺, N₂, N), which decreases the number of adatoms and hence results in a decrease in deposition rate.

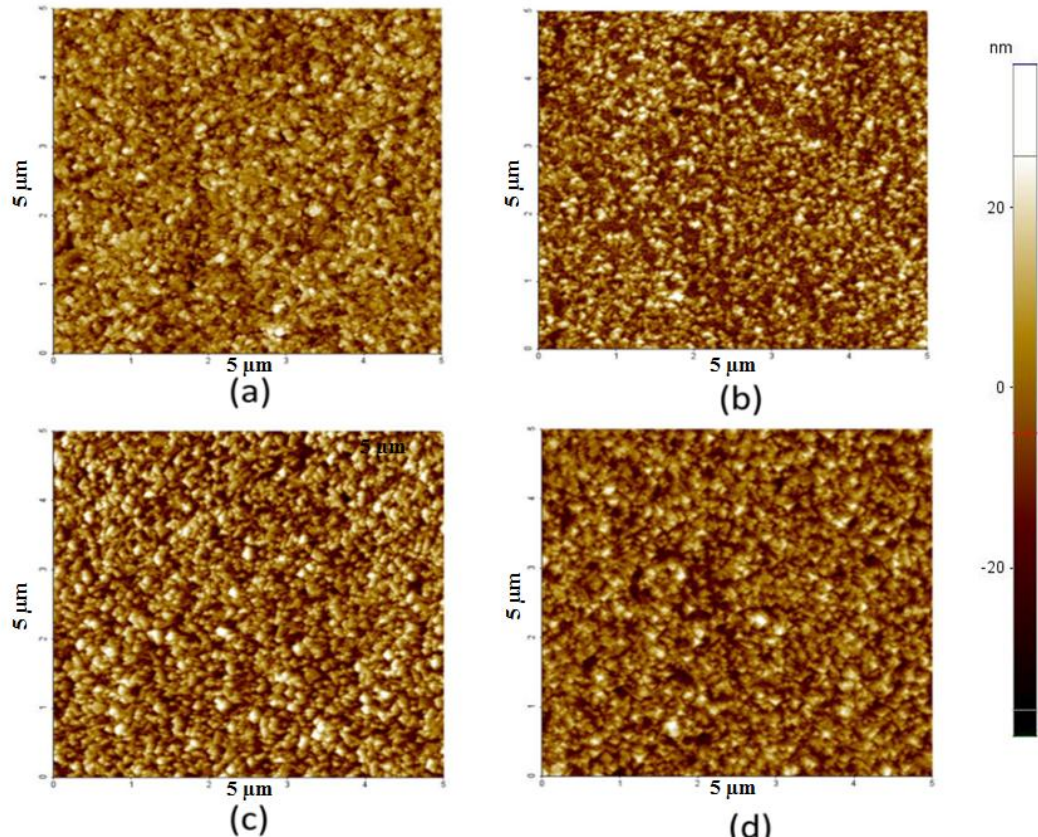


Fig. 3. AFM images of AlN sputtered on 3C-SiC (100) at different N₂/Ar ratio: (a) at 40 % Nitrogen (b) at 60% Nitrogen (c) at 80 % Nitrogen (d) at 100 % Nitrogen.

The morphology of the films was evaluated using atomic force microscopy (AFM) as shown in Figure 3. The r.m.s. roughness (in Root Mean Square (rms)) of the AlN layer increased from 7 nm to 12 nm with increasing N₂/Ar ratio. The higher nitrogen concentration increased the number of energetic nitrogen particles (N₂⁺, N₂, N) being reflected from the target surface. These N₂⁺, N₂, and N particles have lower kinetic energy compared to the heavier Ar⁺ atoms. This kinetic energy is needed to transfer the atoms from the target to the substrate. Consequently, the lower energy provided more time for Al and N atoms to diffuse into the substrate and hence to make the surface rougher at higher N₂ concentration. Also, the crystal orientation of the deposited films changes to polycrystalline (101) and (002) with an

increase in N₂ concentration (as explained above) which may increase the surface roughness and changes surface morphology of the deposited films.

The refractive index of the AlN layer was determined using a Rudolph AutoEL IV Ellipsometer for all samples prepared at the different N₂/Ar ratio. All the measurements were carried out at a wavelength of 632 nm. The values of refractive index were measured in the range of 2.07 to 2.18 for all the samples, which is close to the theoretical value of 2.14 at the said wavelength [34].

The in-plane stresses of the deposited AlN thin films were measured by preparing separate AlN samples that were sputtered on top of a 2 inch Si (100) wafer for all the samples prepared at different N₂ concentration. A Tencor Flexus 2320 system measured the change in the wafer's curvature before and after AlN deposition. This value is then inserted into Stoney equation to calculate the stress as expressed in equation 1:

$$\sigma = \frac{E}{6(1-\nu)} \frac{t_s^2}{t_f} \left(\frac{1}{r_c} - \frac{1}{r_u} \right) \quad (1)$$

where E, ν , t_s and t_f are the Young's modulus, Poisson's ratio for the silicon substrate, silicon thickness and film thickness, respectively. r_u and r_c are the radii of curvature of the Si substrates before and after AlN deposition, respectively. The stresses for all the samples were measured in the range of 320 MPa to 392 MPa, and where tensile in nature.

This stress is inversely proportional to the thickness of the deposited films as stated in Eq 1. The stress values decrease from 392 MPa to 320 MPa when the thickness of the deposited films are changed from 1122 nm to 1600 nm respectively. The thermal gradient of 325 °C between the substrate and room temperatures resulted in in-plane stress due to CTE between AlN thin film and the silicon substrate. We found experimentally that this stress could be tuned from tensile to compressive by varying the DC bias on the substrate. All the samples were prepared at 40 % N₂ concentrations while keeping all the other parameters constant as given in Table 1. Figure 4 shows the change in stress from 500 MPa tensile to 1800 MPa compressive when the RF bias voltage was applied from 0 V to 100 V in steps of 25 V. The transition from tensile stress to a compressive stress with increase in negative bias is attributed to the energetic plasma species bombardment of the growing layer. The ionic bombardment becomes more energetic with an increase in substrate bias which causes the effects of resputtering, defect formation, and ion entrapments, i.e. "collisionally-induced defect formation". This causes the destruction of the columnar growth morphologies and an increase in the compressive stress of the films [35]. Figure 4 shows that a stress free AlN thin

film can be deposited at -40 V bias voltages. This ability is especially critical in tuning the stresses of the thin films to avoid cracking for high temperature applications.

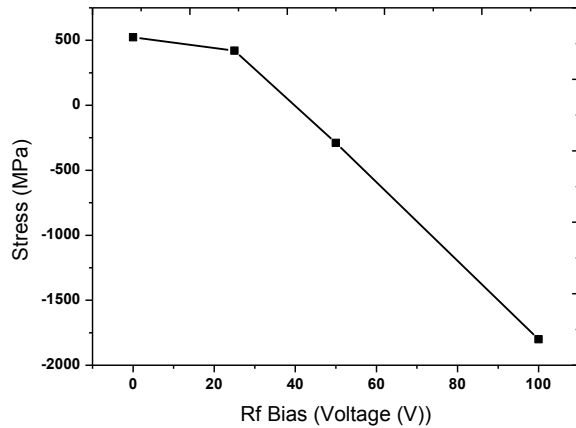


Fig. 4. The plot of residual stress vs. RF bias voltage being applied to the substrate during the sputtering process. A positive value represents tensile stress, and negative values correspond to compressive stress.

The Raman spectroscopy in back scattering configuration was performed for two samples prepared at 40 % and 100 % N₂ concentrations. Figure 5 shows the Raman spectra depicting a major peak E₂ at 654 cm⁻¹ and a minor peak A1(TO) mode at approximately 618 cm⁻¹. The spectra for both samples at two different N₂/Ar ratios are almost identical. The FWHM value of E₂ was calculated as 11.12 cm⁻¹ and 13.75 cm⁻¹ for 40 % and 100 % N₂/Ar ratio, respectively. Those values are between the FWHM values of the AlN bulk single crystal and deposited crystalline AlN. The former is 3 cm⁻¹ as reported by Kuball et al. [36], while the latter is reported to be 50 cm⁻¹ as reported by Perlin et al. [37].

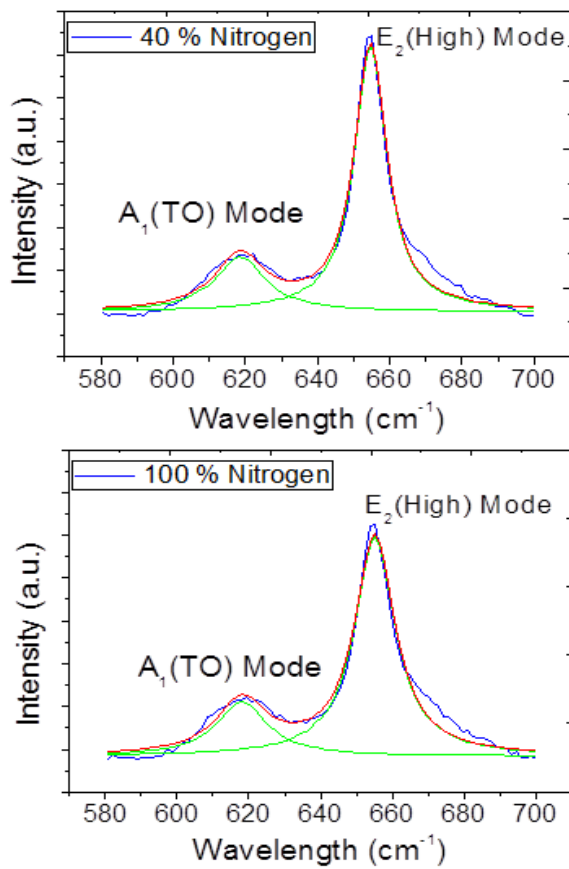


Fig. 5. Raman spectroscopy of AlN at 40 % N₂ flow rate (top) and 100 % N₂ flow rate (bottom)

Table II: Summary of Results of AlN Sputtered at different Nitrogen Concentration

Sample ID	Nitrogen %	Thickness (Å)	Maximum Peaks Intensity of <002> orientation	Maximum Peaks Intensity of <101> orientation	FWHM of Diffraction peak <002> and <101> orientation	Refractive Index	Surface roughness (nm)	Deposition Rate (nm/min)	Stress (MPa) (Tensile)
D1 SiC(100)	40%	16000	2375	220	0.285 ° and 0.305 °	2.18	6.85	8.26	320
D3 SiC(100)	60 %	13420	253.2	204.7	0.263 ° and 0.293 °	2.068	7.85	4.88	344.1
D2 SiC(100)	80 %	11228	124.4	283.60	0.314 ° and 0.320 °	2.085	9.645	4.46	392.8
D4 SiC(100)	100 %	15755	277.6	637.90	0.305 ° and 0.266 °	2.181	12.46	4.45	372.4

*The thickness and Refractive index is measured on Si(100) wafer using ellipsometer and nanospec

4. Conclusion

This paper presented the DC sputtering of AlN (002) and AlN (101) thin films on epitaxial 3C-SiC-on-Si (100) substrates. The crystal orientation can be controllably changed from (002) to (101) by increasing the N₂/Ar flow rate from 40 % to 100 %. The ability of DC sputtering to deposit thick AlN films while maintaining the same crystal quality, and 2) The ability to control the in-plane stress in the deposited thin film would be very useful in piezoelectric MEMS applications. The contributions from this work can especially be employed to produce longitudinal piezoelectric devices and a quasi-shear mode devices using (002) and (101) AlN orientations of AlN film.

ACKNOWLEDGMENTS

This work is supported by Queensland Micro- and Nanotechnology Centre (QMNC) and Griffith School of Engineering. This work was performed in part at the Queensland node of the Australian National Fabrication Facility, a company established under the National Collaborative Research Infrastructure Strategy to provide nano and microfabrication facilities for Australia's researchers. The authors would like to acknowledge The National University of Malaysia and Blue Glass (Sydney) for the XRD measurements, and Leonie Hold at QMNC for the AFM measurement.

References:

- [1] S. Trolier-McKinstry, P. Muralt, Journal of Electroceramics 12 (2004) 7.
- [2] X. Jiang, K. Kim, S. Zhang, J. Johnson, G. Salazar, Sensors 14 (2013) 144.
- [3] R. Elfrink, T. Kamel, M. Goedbloed, S. Matova, D. Hohlfeld, Y. Van Andel, R. Van Schaijk, Journal of Micromechanics and Microengineering 19 (2009) 094005.
- [4] E. Iborra, J. Olivares, M. Clement, L. Vergara, A. Sanz-Hervás, J. Sangrador, Sensors and Actuators A: Physical 115 (2004) 501.
- [5] V. Cimalla, J. Pezoldt, O. Ambacher, Journal of Physics D: Applied Physics 40 (2007) 6386.
- [6] S. Dasgupta, F. Wu, J. Speck, U. Mishra, Applied Physics Letters 94 (2009) 151906.
- [7] Y. Fu, Y. Zhang, W. Yang, H. He, X. Shen, Journal of Crystal Growth 343 (2012) 28.
- [8] C. Chiang, K. Chen, Y. Wu, Y. Yeh, W. Lee, J. Chen, K. Lin, Y. Hsiao, W. Huang, E. Chang, Applied Surface Science 257 (2011) 2415.
- [9] A. Volkova, V. Ivantsov, L. Leung, Journal of Crystal Growth 314 (2011) 113.
- [10] S. Kuchibhatla, L. Rodak, D. Korakakis, Thin Solid Films 519 (2010) 117.
- [11] C. Ribeiro, F. Alvarez, A. Zanatta, Applied Physics letters 81 (2002) 1005.
- [12] A. Szekeres, Z. Fogarassy, P. Petrik, E. Vlaikova, A. Cziraki, G. Socol, C. Ristoscu, S. Grigorescu, I. Mihailescu, Applied Surface Science 257 (2011) 5370.
- [13] Z. Vashaei, T. Aikawa, M. Ohtsuka, H. Kobatake, H. Fukuyama, S. Ikeda, K. Takada, Journal of Crystal Growth 311 (2009) 459.

-
- [14] Y. Kurokawa, K. Utsumi, H. Takamizawa, T. Kamata, S. Noguchi, Components, Hybrids, and Manufacturing Technology, *IEEE Transactions on* 8 (1985) 247.
 - [15] H. Watanabe, N. Yamada, M. Okaji, *International Journal of Thermophysics* 25 (2004) 221.
 - [16] X.-H. Xu, H.-S. Wu, C.-J. Zhang, Z.-H. Jin, *Thin Solid Films* 388 (2001) 62.
 - [17] S. Six, J. Gerlach, B. Rauschenbach, *Thin Solid Films* 370 (2000) 1.
 - [18] M. Akiyama, K. Nagao, N. Ueno, H. Tateyama, T. Yamada, *Vacuum* 74 (2004) 699.
 - [19] G.F. Iriarte, J. Bjurstrom, J. Westlinder, F. Engelmark, I.V. Katardjiev, *Ultrasonics, Ferroelectrics, and Frequency Control, IEEE Transactions on* 52 (2005) 1170.
 - [20] K.-S. Kao, C.-C. Cheng, Y.-C. Chen, *Japanese Journal of Applied Physics* 40 (2001) 4969.
 - [21] T. Aubert, M. Assouar, O. Legrani, O. Elmazria, C. Tiusan, S. Robert, *Journal of Vacuum Science & Technology A* 29 (2011) 021010.
 - [22] J. Komiyama, K. Eriguchi, Y. Abe, S. Suzuki, H. Nakanishi, T. Yamane, H. Murakami, A. Koukitu, *Journal of Crystal Growth* 310 (2008) 96.
 - [23] C.-M. Lin, W.-C. Lien, V.V. Felmetser, M.A. Hopcroft, D.G. Senesky, A.P. Pisano, *Applied Physics Letters* 97 (2010) 141907.
 - [24] R. Nader, J. Pezoldt, *Diamond and Related Materials* 20 (2011) 717.
 - [25] F. Semond, Y. Cordier, N. Grandjean, F. Natali, B. Damilano, S. Vézian, J. Massies, *physica status solidi (a)* 188 (2001) 501.
 - [26] M.-S. Lee, S. Wu, Z.-X. Lin, R. Ro, *Japanese Journal of Applied Physics* 46 (2007) 6719.
 - [27] L. Wang, S. Dimitrijev, J. Han, A. Iacopi, L. Hold, P. Tanner, H.B. Harrison, *Thin Solid Films* 519 (2011) 6443.
 - [28] A. Iqbal, K. Chaik, G. Walker, A. Iacopi, F. Mohd-Yasin, S. Dimitrijev, *Journal of Vacuum Science & Technology B* 32 (2014) 06F401.
 - [29] M. Assouar, O. Elmazria, L. Le Brizoual, P. Alnot, *Diamond and related materials* 11 (2002) 413.
 - [30] S. Cho, *Journal of Crystal Growth* 326 (2011) 179.
 - [31] A. Ababneh, U. Schmid, J. Hernando, J. Sánchez-Rojas, H. Seidel, *Materials Science, and Engineering: B* 172 (2010) 253.
 - [32] A.V. Singh, S. Chandra, G. Bose, *Thin Solid Films* 519 (2011) 5846.
 - [33] H. Cheng, Y. Sun, P. Hing, *Surface and coatings technology* 166 (2003) 231.
 - [34] J. Pastrňák, L. Roskovcová, *physica status solidi (b)* 14 (1966) K5.
 - [35] H.-C. Lee, J.-Y. Lee, *Journal of Materials Science: Materials in Electronics* 8 (1997) 385.
 - [36] M. Kuball, J. Hayes, A. Prins, N. Van Uden, D. Dunstan, Y. Shi, J.H. Edgar, *Applied Physics Letters* 78 (2001) 724.
 - [37] P. Perlin, A. Polian, T. Suski, *Physical Review B* 47 (1993) 2874.

Chapter 5: Highly C-axis Oriented AlN on 3C-SiC-on-Si (111) Substrates by DC Reactive Magnetron Sputtering

This chapter has been submitted as manuscript in Journal of Crystal Growth (under review).

Highly c-axis oriented AlN on 3C-SiC-on-Si (111) substrates by DC reactive magnetron sputtering

A. Iqbal¹, G. Walker¹, L. Hold¹, A. Fernandes², A. Iacopi¹ and F. Mohd-Yasin^{1,2}

¹*Queensland Micro- and Nanotechnology Centre, Griffith University, Nathan, 4111, QLD, Australia*

²*Bluglass Ltd., 74 Asquith Street, Silverwater, 2128, NSW, Australia*

Abstract

This article reports a direct current reactive magnetron sputtering of Aluminum Nitride (AlN) thin films on epitaxial cubic-silicon carbide (111) on silicon (111) substrates. The grazing angle incident x-ray diffraction results on all samples show that the AlN thin-films are highly oriented along the (002) crystalline direction between the N₂/Ar ratio of 40 % to 100 %, at a total gas flow of 50 sccm. This observation is in contrast to the prevailing practices that require either a low or a high N₂/Ar ratio. Four parameters show minimal variations across all samples, namely (a) the extracted FWHM of the (002) diffraction peak with median of 0.28° and standard deviation of 0.012°, (b) area of AlN (002) under the curve is between 92 to 97 %, (c) grain sizes between 30.11 to 32.3 nm, and (d) refractive index values between 2.06 to 2.18. The omega scan rocking curve of two samples at 40 % and 80 % provides evidence of a good quality AlN (002) film with the FWHM values of 1.5° and 2°, respectively. We credit the small lattice mismatch of 1 % between AlN (002) and 3C-SiC (111) as the main factor and provide further analysis to support the claim. Finally, the relationship between the sputtering parameters and the AlN film's properties are elucidated.

Keywords: A1. X-ray diffraction, A3. Physical vapor deposition processes, A3. Polycrystalline deposition, B1. Silicon carbide, B1. Nitride

1. Introduction

Aluminum nitride (AlN) is a potential candidate for use in the power electronics due to its suitable electrical properties such as high electrical resistivity ($10^{15} \Omega\text{.cm}$), high thermal conductivity ($3.3 \text{ WK}^{-1}\text{cm}^{-1}$) and wide bandgap (6.2 eV) [1-3]. AlN grown on a Silicon (Si) substrate is used in RF MEMS because of the high acoustic velocity (12,000 m/s) [4]. Another important use of the AlN thin-films is to make piezoelectric sensors and actuators [5].

AlN thin-films are typically deposited onto Si substrates because of the low cost per surface area and the ease in the fabrication processes. However, the 43 % difference in the coefficient of thermal expansion (CTE) between AlN ($4.6 \times 10^{-6} \text{ K}^{-1}$) and Si ($2.6 \times 10^{-6} \text{ K}^{-1}$) generates cracks in the thin film. These cracks are largely due to the induced stress from the thermal expansion when the film is being cooled down from the high deposition temperature. Also, the lattice mismatch of 19 % between AlN and Si generates dislocations and stresses during the deposition and annealing processes that ultimately results in the deterioration of the AlN crystal quality [6].

* Corresponding author. E-mail address: f.mohd-yasin@griffith.edu.au.

The depositions of AlN on different substrates with lower CTE difference and smaller lattice mismatches have been investigated. Among them, a single crystal cubic silicon carbide-on-Si in <111> plane (3C-SiC(111)-on-Si(111)) with a lattice constant of 4.3596 °A is one of the best substrates for the c-axis oriented AlN (with a lattice constant of 4.978 °A) crystal deposition. Both materials have a lattice mismatch and CTE difference of 1% and 18% [7], respectively. The only reported AlN/3C-SiC (111)/Si (111) structure in the literature was by Nader [8]. This group used the molecular beam epitaxy (MBE) process at a constant nitrogen (N_2) flow and a deposition temperature of 720 °C. They were able to produce AlN (002) with a full width at half maximum (FWHM) of omega scan rocking curve value of 1.18°.

However, MBE has the limitations of a low growth rate, an expensive instrument setup and a high process temperature. For the deposition of materials that are targeted for a low-cost applications, the physical vapor deposition method is preferred because of its high growth rate [9] and the ability to tune the in-plane stress via radio frequency (RF) bias on the substrates [10]. In the specific case of an AlN thin film deposition on top of 3C-SiC(111)-on-Si(111) substrate, direct current (DC) is preferred over the RF sputtering because of the faster deposition rate. This is based on our experience when we performed both sputtering methods using the same equipment [11].

In term of the AlN (002) crystal quality, the lowest reported FWHM value using the omega scan rocking curve is by Lin et al. [12]. This Berkeley group employed DC sputtering and achieved the minimum FWHM value of 1.73°. However, their work utilised a 3C-SiC (100)-on-Si (100) substrate. Due to the higher lattice mismatch of 28.6 % between 3C-SiC(100)-on-Si(100) substrate and AlN (002) film, they used a special technique to achieve a highly c-axis orientation. They first deposited a 50-nm-thick AlN film seed layer with high nitrogen concentration and relatively low AC power of 3 KW, to reduce the negative effect of lattice mismatch between the AlN thin film and the 3C-SiC substrate. The nitrogen concentration was decreased, and the sputtering power was increased to 5.5 KW respectively, during the deposition of the remaining AlN film. This technique was originally proposed by Cheng et al. in their 2003 systematic studies on the relationship between the c-axis AlN and the high N_2/Ar ratio [13]. Xu et al. explain the physics by stating that the crystal orientation of deposited films depends on the kinetic energy of sputtering particles, deposition rate and adatoms mobility, which can be modified via the sputtering parameters. The adatoms with high mobility arrange themselves in the close packed (002) orientation because of its lowest

surface energy and the maximum atomic density state [14]. At the other extreme, there are also published works that could only manage to achieve a highly c-axis AlN orientation at lower N₂ concentration. Amongst them, Meng et al. reported the use of a 30 % N₂/Ar ratio to achieve AlN(002) on top of the ZnO/Si structure [15]. The most recent example is our work on an AlN/3C-SiC-on-Si (100) substrate [16]. We could only achieve a highly c-axis AlN at 40% N₂/Ar ratio, with the total gas flow of 50 sccm. Pellegrini et al. [17] offered the explanation on the need for the lower N₂/Ar ratio to achieve the highly c-axis AlN film. They explained that at a lower N₂/Ar ratio, Argon atoms with heavier mass compared to nitrogen atoms were dominant. Due to their higher masses, they provided higher kinetic energies for the adatoms, which consequently assisted the formation of AlN (002) film.

In our previous publication [16], we reported the formation of AlN (002) on top of 3C-SiC(100)-on-Si (100) substrates at 40 % N₂/Ar ratio. When the N₂/Ar ratio was increased to 80%, AlN (101) dominated. In this work that used the 3C-SiC(111)-on-Si (111) substrates, we achieved a highly c-axis AlN thin film with reasonable consistency from 40 to 100 % N₂/Ar ratio. The samples for both works were batch-fabricated with the same equipment and process parameters. We offer technical insights for this interesting result in section 3.

2. Experimental Details:

The experimental details were already presented in [16], but worth repeating here for the continuity of this article. Some additional information has also been added. Before the AlN deposition, a 300 nm thick 3C-SiC thin film in (111) plane was epitaxially grown on top of a 150 mm diameter of 4° off-axis Si (111) wafer. A custom-made hot-wall horizontal low-pressure chemical vapour deposition (LPCVD) system that employed alternating supply epitaxy performed the deposition of the 3C-SiC thin film at a temperature at 1000 °C. The details of these epitaxial depositions are documented in [18]. The surface roughness of the 3C-SiC(111) was measured to be about 2 nm (RMS). Artieda et al. [19] reported that the substrate condition, especially the surface roughness of substrate affects the crystal quality of the deposited AlN film. Therefore, all AlN depositions were performed using the samples that were sourced from the same substrate wafer.

The DC sputtering of the AlN thin-film on top of the 3C-SiC (111)-on-Si (111) substrate was performed using a magnetron sputtering system (Surrey Nano Systems Gama 1000) at a

substrate temperature of 350 °C and a sputtering power of 1200 W. 350 °C is the optimized temperature to obtain a highly c-axis oriented AlN-based on preliminary X-ray diffraction (XRD) data. 1200 W is the maximum power to sustain the stable plasma operation in our deposition system. An Aluminum (Al) target with 99.999 % purity was employed. Initially, the 3C-SiC(111)-on-Si(111) samples of 15 mm by 15 mm in dimension were cut via a disco wafer dicer. They were then cleaned via a standard piranha cleaning process to remove the organic substances. The oxidation on the samples was removed by submerging them in a diluted 1% HF acid for 5 minutes. The sputtering system was turbo-pumped down to the base pressure of 2×10^{-8} Torr, followed by a constant pumping through the cryogenic pump. The low base pressure prevented the incorporation of oxygen into the AlN thin films. The main chamber was purged with 15 sccm of 99.999 % Ar gas for 3 minutes prior to the samples loading to avoid contamination. The samples were inserted into the main chamber via a two-stage loading system. The samples were then heated to 300 °C with an IR heater for 3 minutes to remove moisture. The sputtering systems base pressure of 2×10^{-8} Torr is maintained with a cryogenic pump. The 99.999% Ar and 99.999% N₂ process gases were passed through gas purifiers (SAES, Italy). The samples were then placed on a susceptor. Prior to loading, the samples were heated in a turbo-pumped vacuum load lock at 200 °C for 3 minutes to reduce moisture, and the main chamber was purged with Ar for 3 minutes to reduce contamination. The face of the 4" diameter Al target was set at 20 degrees off perpendicular to the susceptor. The distance between the centres of the target and susceptor was 20 cm. The susceptor was rotated at 10 rpm during deposition. The plasma was struck at 20 mT and reduced gradually to 2 mT before opening the target shutter and commencing deposition. We found that the deposition pressure of 2 mT was the lowest pressure at which stable plasma could be maintained. The total gas flow for all ratios of Ar and N₂ was 50 sccm. By performing a parametric sweep (Refer to Figure 1 of [16]), it was determined that at a 40 % N₂/Ar ratio the sputtering process became reactive. Four AlN samples were produced at a different N₂/Ar ratio in the following order: 40 % (sample F1), 80 % (sample F2), 60 % (sample F3) and 100 % (sample F4). The samples were ordered in non-increment N₂/Ar ratio to ensure that the setup in the sputtering system did not influence the results. The deposition times ranged from 3 to 6 hours to achieve the film's thickness of over 1 μm.

The deposited AlN films were characterized by the following analytical tools: grazing angle incident x-ray diffraction (Bruker D8 using Cu Kα1 beam with $\lambda=1.5405980$ Å, grazing angle of 1°, voltage of 40 kV and current of 40 mA), omega scan rocking curve (Panalytical

Empyrean XRD a high resolution four-crystal Ge (220) asymmetrical incident beam monochromator, using Cu K α 1 radiation with $\lambda = 1.5405980 \text{ \AA}$, a PIXcel-3D detector with a fixed anti-scatter slit; the PIXcel detector is used in the open detector mode for the rocking curve and phi scan measurements), refractive index (Rudolph AutoEL IV Ellipsometer), deposition rate (Nanospec AFT 180) and surface roughness (Park NX20 AFM).

3. Results and Discussions:

Table I. Summary of the characterization results

Sample on SiC(111)	Nitrogen %	AlN (002) Peak position*	FWHM of <002> Diffraction Peak (°)	Percentage of Area under curve <002>** %	Grain size (nm)	Surface roughness (nm)	Refractive Index	Thickness (nm)	Deposition Rate (nm/min)	Stress*** (GPa)
F1	40%	36.16	0.28	92	31.18	6.85	2.18	1600	8.26	2.55
F3	60 %	36.14	0.28	92.3	31.18	7.85	2.068	1342	4.88	2.12
F2	80 %	36.17	0.3	97	30.11	9.65	2.085	1122	4.46	2.77
F4	100 %	36.2	0.27	93.6	32.3	12.46	2.181	1575	4.45	3.42

*The observed XRD peaks can be assigned to wurtzite AlN phase (Card # 01-070-2545) with AlN (002) peak at $2\theta = 36.023^\circ$ [20]

** Percentage of <002> is calculated by measuring the area under curve for all AlN orientations in the XRD spectra

***Biaxial stress values were extracted from the XRD diffraction peak position

Table I summarizes the characterization results for all the samples. The general trends are the followings: the N₂/Ar ratio has a small influence on the FWHM of the diffraction peak, the percentage of <002> area under the curve, grain sizes, and refractive index. The deposition rate and thickness decrease with an increasing N₂/Ar ratio, while the surface roughness and biaxial stress increase with an increasing N₂/Ar ratio.

The details of the different types of characterizations are explained below. The grazing angle incident x-ray diffraction (GIXRD) measurement at 1° incidence was employed due to the smaller thickness of AlN film and SiC(111) compared to the Si substrate. The GIXRD scan for all samples is shown in Figure 1. A major diffraction peak is observed between $2\theta = 36.14$ to 36.2° . The peak position for wurtzite AlN phase from the Joint Committee of Powder Diffraction (Card # 01-070-2545) is 36.023° [20]. Therefore, the measured peak position from Figure 1 can be attributed to AlN (002) orientation. The minor peaks at 34° , 38° and 50° refer to (100), (101) and (102) orientations of AlN, respectively.

We extracted the FWHM of the (002) diffraction peak values from Figure 2 using Gaussian fitting instead of Lorentz fitting, as the former provides better curve fitting for all

the curves [21,22]. This particular technique of extracting the FWHM values from the diffraction peaks had been employed by three similar works on AlN [11,18,23]. The extracted FWHM of diffraction peak values were similar with a median of 0.28° and standard deviation of 0.012° . This observation is corroborated by another parameter. The percentage of (002) to other AlN crystal orientations is calculated to be between 92-97 % for all samples by measuring the area under the curve.

We sent two samples for the omega scan rocking curve measurement to assess the quality of the two films. The insets of Figure 1 show the FWHM values from the omega scan rocking curve for samples that were deposited at 40% and 80% N₂/Ar ratio. The AlN (002) omega-scan FWHM values at 1.5° and 2° are close to the reported 1.73° FWHM using DC sputtering on 3C-SiC on Si(100)[12]. This Berkeley group DC sputtered AlN(002) on top of 3C-SiC-on-Si(100) substrate using a commercial substrate from NovaSiC (France). It must be noted that the diffraction peaks of 3C-SiC (111) and AlN(002) are very close, and they might overlap in rocking curve measurements. However, we assume that the rocking curve diffraction peaks are from AlN (002) films because of the relatively 4 to 5 times larger film thickness of AlN, compared to 3C-SiC(111) film.

After assessing all samples, the minimum FWHM value of rocking curve at 40 % of N₂ to Ar ratio provides the best result in terms of c-axis oriented AlN crystal quality growth on 3C-SiC(111) substrate, while keeping all other sputtering parameters constant at sputtering temperature of 350°C , sputtering pressure of 2 mTorr, and sputtering power of 1200W. These parameters are the optimised process conditions.

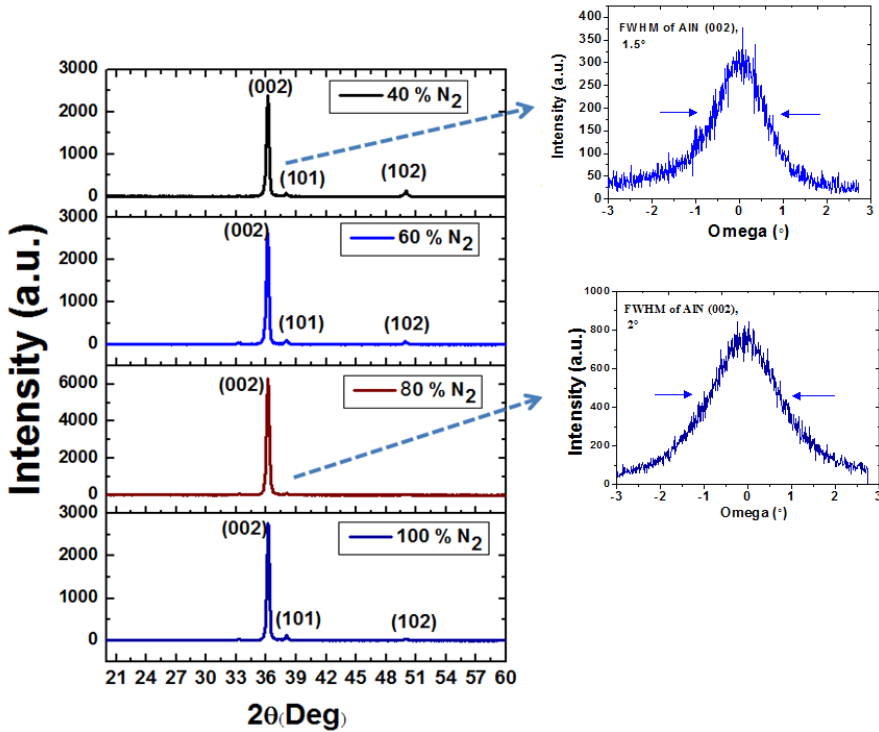


FIG. 1. Grazing angle XRD of AlN deposited on 3C-SiC/Si (111) film at the different N₂/Ar ratio. The inset figures show the omega scan rocking curve measurement of the (002) peaks for the samples at 40% and 80% N₂/Ar ratio

The grain size was calculated using Scherrer's equation. The values at 40 %, 60 %, 80 % and 100 % N₂/Ar ratios are 31.18 nm, 31.18 nm, 30.11 nm and 32.3 nm, respectively. There is only a 7 % difference between the highest and the lowest values. As a comparison, Meng et al. found a 100% variation in the grain size of AlN(002) films being deposited on Si (111) and on ZnO/Si(100) substrates [15].

The refractive index of the AlN layer was determined using a Rudolph AutoEL IV Ellipsometer for all samples prepared at the different N₂/Ar ratio. All the measurements were carried out at a wavelength of 632 nm. The values of refractive index were measured in the range of 2.07 to 2.18 for all the samples, which is close to the theoretical value of 2.14 at the said wavelength. There is only a 5 % difference between the highest and the lowest values of refractive index for these samples.

It is very clear from Figure 1 and the four parameters (FWHM of diffraction peak, the percentage of <002> area under the curve, grain sizes and refractive index) that a highly c-axis oriented AlN films had been achieved on all samples from 40 % to 100 % N₂/Ar ratio. This is in contrast to the existing practices that need either a very high or a very low N₂/Ar ratio, both with different theories for doing so as described in section 1. In order to appreciate the value of this interesting result, Figure 2 reproduces two GIXRD scans from the literature

on the deposition of AlN (002) at varying N₂/Ar ratios. The graph on the left shows the deposition of the AlN (002) at a 40 % N₂/Ar ratio on the 3C-SiC-on-Si (100) substrate. This figure was published in [16]. It is important to note that this is our work, and the samples were batch-processed using the same equipment and process parameters. The graph on the right shows the deposition of AlN (002) on Si (100) substrate at 100 % N₂/Ar ratio, which is not our work. This figure was originally published in [13].

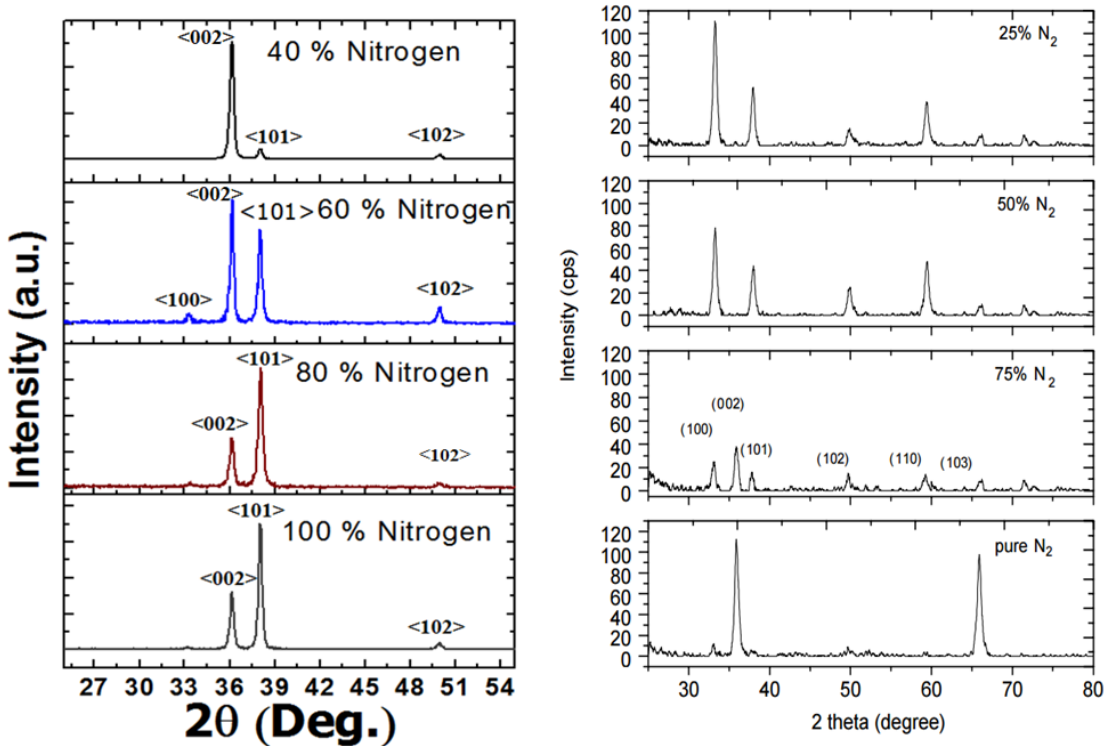


FIG. 2. The XRD plot on the left characterized the deposition of AlN on top of 3C-SiC-on-Si (100) by Iqbal et al. [16]. The XRD plot on the right characterized the deposition of AlN on top of Si (100) by Cheng et al. [13].

In our opinion, the main factor for the growth of highly c-axis oriented AlN films impervious to the N₂ concentration is due to the smaller lattice mismatch of 1 % between the AlN (002) and the 3C-SiC (111) layer. Both have similar hexagonal structure, which greatly assists the formation of the former on top of the latter. We refer to the work of Lim et al. [24], which performed RF sputtering and compared the structural properties between AlN/Si, AlN/Ru/Si, and AlN/ZnO/Si substrates. They observed that AlN/Ru/Si and AlN/ZnO/Si substrates produced better AlN(002) crystal quality than AlN/Si substrate because of AlN, Ru, and ZnO have hexagonal-closed-pack structure. They further observed an AlN/ZnO/Si substrate produced better AlN(002) crystal quality than the AlN/Ru/Si substrate due to

smaller lattice mismatch of 4% between AlN and ZnO, compared to 15% lattice mismatch between AlN and Ru. We also refer to the work of Meng et al. that observed highly c-axis oriented AlN(002) films with better crystal quality on top of the ZnO/Si substrate, compared to AlN/Si substrate [15] due to smaller lattice mismatch and similar crystal structure of AlN and ZnO.

By applying the same logic here, another work of ours [16] required 40 % N₂/Ar ratio to form highly c-axis AlN on 3C-SiC-on-Si (100) substrate (with a lattice mismatch of 28.6 % [12]). That work employed the same sputtering system and process parameters as the one presented in this work. Since the 3C-SiC (111) substrate has even smaller lattice mismatch with AlN (002) of 1 % and similar crystal structure [7], this factor assists the formation of highly c-axis oriented AlN from the start of reactive mode at 40 % all the way to 100 % N₂/Ar ratio. In the next three paragraphs, we attempt to provide more analysis and insights to verify the role of the smaller lattice mismatch.

Xu et al. observed that the mobility of adatoms can be increased by increasing their kinetic energies, which assists them to arrange in the close packed (002) orientation [14]. According to Lee et al., there are three common methods to do this i.e. by decreasing the sputtering pressure, by increasing the sputtering power or by decreasing the nitrogen concentration [25]. As mentioned earlier, we have found the optimised parameters for our specific sputtering system at the pressure of 2 mTorr and power of 1200 W.

The crystal structure of c-axis oriented AlN [26], superimposed on 3C-SiC (100)[27], is shown in Fig 3(a). It can be observed that the 3C-SiC (100) has a fourfold symmetry and has a large lattice mismatch of 28 % with c-axis oriented AlN, which is not suitable for growing c-axis oriented AlN. The Berkeley group overcame this problem by sputtering a nucleation layer on top of a 3C-SiC(100) before the sputtering of c-axis oriented AlN [12]. Another method is by increasing the kinetic energy of the adatoms by decreasing the N₂ concentration, which was performed by us in [16]. In that work, we successfully deposited (002) oriented AlN at only 40 % N₂/Ar ratio on top of 3C-SiC (100) substrate. The low N₂/Ar ratio favours the highly c-axis oriented AlN because, at lower N₂/Ar ratio, Ar⁺ dominates around the target, Ar⁺ has heavier atomic mass compare to N₂⁺ and thus produce larger kinetic energy of adatoms, and enhances the adatoms mobility, resulting in the close packed (002) orientation. However, at a high N₂/Ar ratio, the nitrogen particles (N₂⁺, N₂, N) with lighter atomic mass dominate and the Ar particle numbers decreases. Hence the kinetic

energy of the adatoms and mobility decreases which favour other crystal orientation e.g. (101).

In the case of a 3C-SiC (111) substrate (which is presented in this article), the low N₂/Ar ratio still favours the highly c-axis oriented AlN. However, the XRD results from Figure 2 reveal that (002) oriented AlN remains dominant at a higher N₂/Ar ratio as well, up to a 100 % N₂ environment. Therefore, there must be another factor for this change, that is the smaller lattice mismatch (1 %) between 3C-SiC (111) and AlN (002), as opposed to 18 % lattice mismatch between 3C-SiC (100) and AlN (002). It is well-known that the crystallinity of the deposited films depends on the quality of the nucleation layer and the nature of the bonding between the substrate and deposited film [28]. The crystal structure of the c-axis oriented AlN superimposed over the 3C-SiC (111) crystal structure [29] is shown in Fig 3(b). The 3C-SiC (111) has a sixfold atomic arrangement (three-fold symmetry) that provides a better template and lattice matching for the c-axis oriented AlN. At the beginning of sputtering, the AlN seed layer is grown along the (002) orientation via making a bond with the three-fold symmetrical hexagonal 3C-SiC (111) substrate. The AlN layer follows the seed layer for the rest of sputtering and grows in a well-aligned manner on the seed layer in close packed (002) orientation, irrespective of the kinetic energy of adatoms modified by the N₂ concentration during sputtering. Similar results were observed by Dadgar et al. [30], in which they observed better GaN film quality on Si(110) orientation because of the existence of the inherent seed layer.

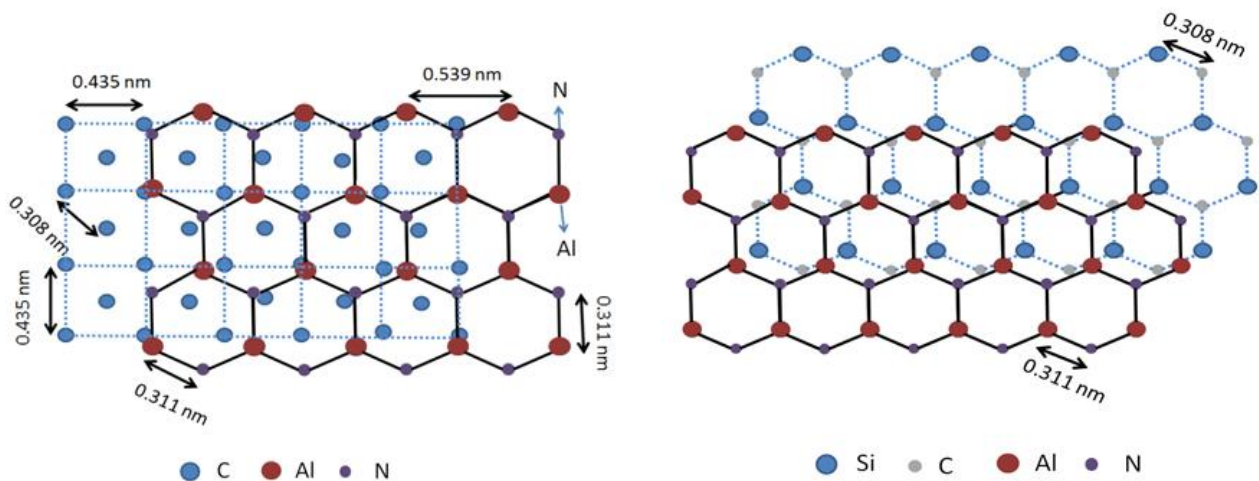


FIG. 3. Crystal structures of (a) AlN (002) on 3C-SiC (100), and (b) AlN (002) on 3C-SiC (111)

If we refer to Table I, there are four parameters that show variations in their values on the samples at different N₂/Ar ratios. These are the deposition rate, thickness, surface roughness and biaxial stress. The values of the deposition rate and thickness are very similar to the ones that we obtained on 3C-SiC-on-Si (100) substrate as reported in [16]. This was because they were batch-deposited and characterized together. The main factor for the variation in the values of these parameters is due to the different deposition times (between 3 to 6 hours) for samples at different N₂/Ar ratio. We had to vary the deposition times to achieve the AlN film's minimum thickness of 1 μm. The effect of the deposition time on all four parameters will be elucidated in the subsequent paragraphs. It is important to stress at this point that the variation in the film thicknesses does not affect the main thesis of this article. That is, we achieve highly c-axis AlN films between 40 to 100 % N₂/Ar ratio as evidenced by the consistent values of the peak position, the FWHM of the diffraction peak, percentage of <002> area under the curve, grain sizes and refractive index. It is equally important to emphasize the fact that we did not get similar XRD results for the deposition on the 3C-SiC-on Si (100) substrate, as shown in Figure 2 (left).

The root mean square (RMS) roughness of the deposited films was measured in a 5 μm × 5 μm area using non-contact mode Atomic Force Microscopy (Park AFM). Figure 4 shows the AFM images for all the samples. In section 2, we already stated that all four samples used the same 3C-SiC (111)/Si (111) substrate with a surface roughness of about 2 nm. The results from Table 1 demonstrate an increase of the surface roughness with an increase of N₂/Ar ratio from 7 nm to 12 nm. This can be explained as follows. The growth rate depends primarily on the number of adatoms with high kinetic energies. As the nitrogen concentration becomes 100 %, the number of these highly energetic adatoms decreases. This is due to the decrease in the heavier mass of the single-charged ion (i.e. Ar+) compare to the lighter-mass nitrogen particles (N₂⁺, N₂, N). This results in the decrease in the deposition rate, which provides more time for Al and N atoms to diffuse on the substrate, and hence lead to an increase in surface roughness [31].

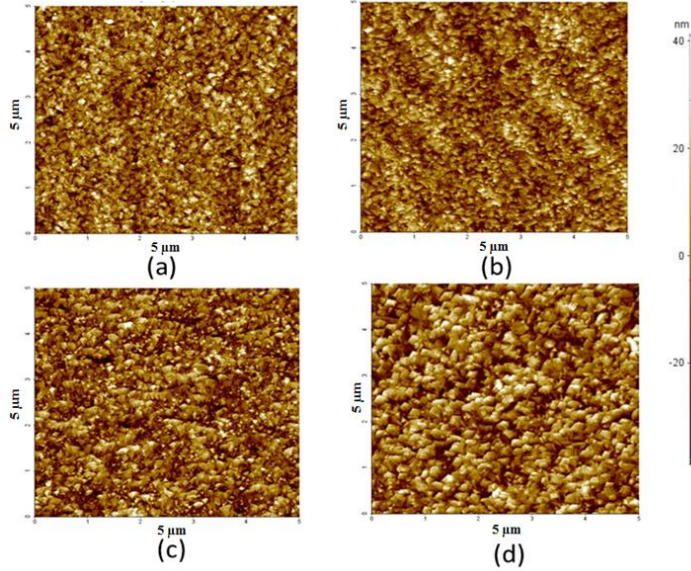


FIG. 4. AFM of AlN sputtered on 3C- SiC(111) at different N₂ flow rate: (a) 40 % Nitrogen, (b) 60% Nitrogen, (c) 80 % Nitrogen and (d) 100 % Nitrogen

The deposition rate and the thickness of the AlN layer were obtained via separate AlN sputtered samples on top of a doped p-type Si (100) wafer employing Nanospec AFT 180 instrument spectroscopic reflectometer. The deposition rate of 8.26 nm/min was measured at 40 % N₂/Ar ratio, which decreased to 4.88 nm/min at 60 % N₂/Ar ratio. The deposition rate further decreased to 4.46 nm/min at 80 % N₂/Ar ratio. This rate remained for the 100 % N₂/Ar ratio. In general, it can be observed that the deposition rate decreases with an increase in N₂/Ar ratio. That is, less deposition time will be required for a depositing film of the same thickness in the case of lower N₂/Ar ratio. The pattern is due largely to the decrease of the single-charged ion (i.e. Ar⁺) with the higher mass at the higher N₂/Ar ratio. At the same time, there is an increase of the lower-mass nitrogen particles (N₂⁺, N₂, N), which subsequently decreases the number of highly energetic adatoms, resulting in the decrease in the deposition rate. The thicknesses of the deposited films are found to be in the range 1.1 to 1.6 μm .

We could not measure the in-plane stress of the AlN samples deposited on 3C-SiC(111)/Si(111) substrates using Tencor Flexus 2320 System because of the unavailability of 50 mm 3C- SiC(111)/Si(111) wafers. As an alternative, we measured the biaxial stress deduced from the XRD data as given in Table 1. This alternate method is proposed by Tanaka et al. [32]. The biaxial stress of the AlN films was calculated by extracting the c-lattice constant from the diffraction peak position depicting a (002) orientation in the θ -2 θ diffraction spectra. The biaxial stress (σ) is normally given by the equation: $\sigma = -812.41 \times 10^9 ((c - c_0)/c_0)$, where c_0 is the strain-free lattice parameter ($c_0 = 4.9795 \text{ \AA}$) that is measured from AlN powder sample [32]. The value of c (lattice constant) was extracted from

the experimental data as “c” is equal to two times the interplanar spacing d , where $d = \lambda/2 * \sin \theta$ from Bragg’s law, where $\lambda = 1.5405980 \text{ \AA}$ and θ is diffraction angle from XRD 2θ plot.

The biaxial stress can be attributed to three sources: the epitaxial stress i.e. lattice mismatch between the substrate and the film, thermal stress i.e. the difference in thermal coefficient of expansion between the substrate and the film, and microstructure and the intrinsic stress i.e. growth stress [33]. In our experiment, the thermal stress and the intrinsic stress are the major sources of biaxial stress, while the epitaxial stress has minimum value because of the 1 % lattice mismatch. Further, the values of the thermal stress remain approximately the same for all samples as the sputtering was performed at the same substrate temperature of $350 \text{ }^{\circ}\text{C}$. Therefore, the intrinsic stress is the component that is changing at the different N_2/Ar ratio.

The calculated values of the biaxial stress of all four samples are given in Table 1. The overall trend is that the stress increases with increasing N_2/Ar ratio. As discussed before, the deposition rate decreases with an increase in N_2 concentration, which provides more time for Al and N atoms to diffuse into the substrate and hence, the small crystallite coalesce to make larger crystals. The collision between these large crystal generates the tensile stress [34]. This hypothesis is corroborated by the increase in the surface roughness with an increase in N_2/Ar ratio [35].

Conclusion:

We have successfully DC-sputtered AlN (002) thin films on top of the 3C-SiC(111)-on-Si(111) substrate over a wide range of N_2/Ar ratio. We are able to relate the effect of the varying gas ratio to the thin film’s properties as follows: (1) The N_2/Ar ratio has a small influence on the FWHM of 2θ peak position, the FWHM of the diffraction peak, the percentage of $<002>$ area under the curve, grain sizes and refractive index. (2) The deposition rate and thickness decrease with an increasing N_2/Ar ratio. (3) The surface roughness and biaxial stress increase with an increasing N_2/Ar ratio. Finally, the omega scan rocking curve measurement on two samples show that we have produced high crystal quality AlN (002) films with FWHM of 1.5 ° and 2 ° . Out of four samples, sample F1 emerges as the overall winner. It has the lowest FWHM of rocking curve, lowest surface roughness, second lowest in-plane stress, highest thickness, highest deposition rate, and the best matched refractive index. The optimised deposition parameters are the following: sputtering power of 1200W, sputtering temperature of $350 \text{ }^{\circ}\text{C}$, sputtering pressure of 2 mTorr, the N_2/Ar ratio of 40 % at

the total gas flow of 50 sccm, and target to substrate distance of 20 cm. The recipe from this article can be used to produce low-cost piezoelectric devices such as an energy harvesters [36-38].

Acknowledgments

This work is supported by Queensland Micro- and Nanotechnology Centre (QMNC) and Griffith School of Engineering. This work was performed in part at the Queensland node of the Australian National Fabrication Facility, a company established under the National Collaborative Research Infrastructure Strategy to provide nano and microfabrication facilities for Australia's researchers. The authors would like to acknowledge Mr. Zailan Mohd Yusof of The National University of Malaysia (Bangi, Malaysia) for the grazing-incident XRD measurements. In addition, the author would like to express gratitude to Dr. David Massoubre of InfiniLED (Cork, Ireland) for helpful comments and suggestions on this manuscript.

References

- [1] J. Ruffner, P. Clem, B. Tuttle, D. Dimos, D. Gonzales, *Thin Solid Films* 354 (1999) 256.
- [2] A. Claudel, Y. Chowanek, E. Blanquet, D. Chaussende, R. Boichot, A. Crisci, G. Berthomé, H. Mank, S. Luca, D. Pique, *physica status solidi (c)* 8 (2011) 2019.
- [3] D. Isarakorn, A. Sambri, P. Janphuang, D. Briand, S. Gariglio, J. Triscone, F. Guy, J. Reiner, C. Ahn, N. de Rooij, *Journal of Micromechanics and Microengineering* 20 (2010) 055008.
- [4] V. Cimalla, J. Pezoldt, O. Ambacher, *Journal of Physics D: Applied Physics* 40 (2007) 6386.
- [5] C. Zuo, N. Sinha, J. Van der Spiegel, G. Piazza, *Microelectromechanical Systems, Journal of* 19 (2010) 570.
- [6] J. Komiyama, K. Eriguchi, Y. Abe, S. Suzuki, H. Nakanishi, T. Yamane, H. Murakami, A. Koukitu, *Journal of Crystal Growth* 310 (2008) 96.
- [7] Z. Yong-Mei, S. Guo-Sheng, L. Jia-Ye, L. Xing-Fang, W. Lei, Z. Wan-Shun, L. Jin-Min, *Chinese Physics Letters* 24 (2007) 1753.
- [8] R. Nader, J. Pezoldt, *Diamond and Related Materials* 20 (2011) 717.
- [9] E. Iborra, J. Olivares, M. Clement, L. Vergara, A. Sanz-Hervás, J. Sangrador, *Sensors and Actuators A: Physical* 115 (2004) 501.
- [10] Y.-J. Lai, W.-C. Li, C.-M. Lin, V. Felmetser, A.P. Pisano, *High-temperature stable piezoelectric aluminum nitride energy harvesters utilizing elastically supported diaphragms, Solid-State Sensors, Actuators and Microsystems (TRANSDUCERS & EUROSENSORS XXVII), 2013 Transducers & Eurosensors XXVII: The 17th International Conference on*. IEEE, 2013, p. 2268.
- [11] A. Iqbal, K. Chaik, G. Walker, A. Iacopi, F. Mohd-Yasin, S. Dimitrijev, *Journal of Vacuum Science & Technology B* 32 (2014) 06F401.
- [12] C.-M. Lin, W.-C. Lien, V.V. Felmetser, M.A. Hopcroft, D.G. Senesky, A.P. Pisano, *Applied Physics Letters* 97 (2010) 141907.
- [13] H. Cheng, Y. Sun, J. Zhang, Y. Zhang, S. Yuan, P. Hing, *Journal of crystal growth* 254 (2003) 46.
- [14] X.-H. Xu, H.-S. Wu, C.-J. Zhang, Z.-H. Jin, *Thin Solid Films* 388 (2001) 62.
- [15] X. Meng, C. Yang, Q. Chen, Y. Gao, J. Yang, *Materials Letters* 90 (2013) 49.
- [16] A. Iqbal, G. Walker, A. Iacopi, F. Mohd-Yasin, *Journal of Crystal Growth* Submitted to (2016).
- [17] M.V. Pelegrini, I. Pereyra, *physica status solidi (c)* 7 (2010) 840.
- [18] L. Wang, S. Dimitrijev, J. Han, A. Iacopi, L. Hold, P. Tanner, H.B. Harrison, *Thin Solid Films* 519 (2011) 6443.

- [19] A. Artieda, M. Barbieri, C.S. Sandu, P. Muralt, *Journal of applied physics* 105 (2009) 024504.
- [20] S. Khan, M. Shahid, A. Mahmood, A. Shah, I. Ahmed, M. Mehmood, U. Aziz, Q. Raza, M. Alam, *Progress in Natural Science: Materials International* 25 (2015) 282.
- [21] S. Dasgupta, F. Wu, J. Speck, U. Mishra, *Applied Physics Letters* 94 (2009) 151906.
- [22] M. Akiyama, K. Nagao, N. Ueno, H. Tateyama, T. Yamada, *Vacuum* 74 (2004) 699.
- [23] M. Assouar, O. Elmazria, L. Le Brizoual, P. Alnot, *Diamond and related materials* 11 (2002) 413.
- [24] W.T. Lim, B.K. Son, D.H. Kang, C.H. Lee, *Thin Solid Films* 382 (2001) 56.
- [25] M.-S. Lee, S. Wu, Z.-X. Lin, R. Ro, *Japanese Journal of Applied Physics* 46 (2007) 6719.
- [26] W. Wang, W. Yang, Z. Liu, H. Wang, L. Wen, G. Li, *Scientific reports* 5 (2015).
- [27] M.A. Fraga, M. Bosi, M. Negri, (2015).
- [28] R. Liu, F. Ponce, A. Dadgar, A. Krost, *Applied physics letters* 83 (2003) 860.
- [29] A. Gupta, D. Paramanik, S. Varma, C. Jacob, *Bulletin of Materials Science* 27 (2004) 445.
- [30] A. Dadgar, F. Schulze, M. Wienecke, A. Gadanecz, J. Bläsing, P. Veit, T. Hempel, A. Diez, J. Christen, A. Krost, *New Journal of Physics* 9 (2007) 389.
- [31] H. Liu, G. Tang, F. Zeng, F. Pan, *Journal of Crystal Growth* 363 (2013) 80.
- [32] M. Tanaka, S. Nakahata, K. Sogabe, H. Nakata, M. Tobioka, *Japanese journal of applied physics* 36 (1997) L1062.
- [33] P. Panda, R. Ramaseshan, N. Ravi, G. Mangamma, F. Jose, S. Dash, K. Suzuki, H. Suematsu, *arXiv preprint arXiv:1507.08113* (2015).
- [34] Z. Fang, Z. Yan, Y. Tan, X. Liu, Y. Wang, *Applied Surface Science* 241 (2005) 303.
- [35] M.-A. Dubois, P. Muralt, *Journal of Applied Physics* 89 (2001) 6389.
- [36] V. Mastronardi, F. Guido, M. Amato, M. De Vittorio & S. Petroni, *Microelectronic Engineering* 121 59-63 (2014).
- [37] R. B. Karabalin, M. H. Matheny, X. L. Feng, E. Defaÿ, G. Le Rhun, C. Marcoux, ... & M. L. Roukes, *Applied Physics Letters* 95(10) 103111. (2009).
- [38] R. Mahameed, N. Sinha, M. B. Pisani, & G. Piazza, *Journal of Micromechanics and Microengineering* 18(10) 105011 (2008).

Chapter 6: The Sputtering Of C-axis Oriented AlN Films on Top of On-and Off-axis 3C-SiC/Si Substrates at different Deposition Temperatures

This chapter will be submitted as a manuscript in the Journal of Thin Films or equivalent.

The sputtering of c-axis oriented AlN films on top of on- and off-axis 3C-SiC/Si (111) substrates at different deposition temperatures

A. Iqbal¹, G. Walker¹, L. Hold¹, A. Fernandes², P. Tanner¹, A. Iacopi¹ and F. Mohd-Yasin¹

¹*Queensland Micro- and Nanotechnology Centre, Griffith University, Nathan, 4111, QLD, Australia*

²*Bluglass Ltd., 74 Asquith Street, Silverwater, 2128, NSW, Australia*

Abstract

The AlN thin films have been sputtered on top of on-axis and 4° off-axis 3C-SiC/Si (111) substrates at five deposition temperatures. The grazing angle incident XRD and FWHM rocking curve values provide evidence that the films are highly oriented along the (002) direction. The data indicates that the off-axis substrates provide a better template for the successful deposition, where the crystal quality is better in term of the FWHM of rocking curve values. Furthermore, the said values are quite consistent across different deposition temperatures. We perform further characterization in term of surface morphology, in-plane stress and deposition rate. We also extracted the values for the bi-axial stress, grain size and piezoelectric coefficient of the films.

Keywords: Physical vapour deposition processes; Polycrystalline deposition; X-ray diffraction; Aluminum Nitride; Silicon carbide

1. Introduction

Aluminum nitride (AlN) has excellent electrical properties, such as high electrical resistivity (10^{15} $\Omega\text{.cm}$), high thermal conductivity ($3.3 \text{ WK}^{-1}\text{cm}^{-1}$) and wide bandgap (6.2 eV) [1-3], which makes it a potential candidate for power electronics applications. AlN is also used in RF MEMS because of high acoustic velocity (12,000 m/s) [4]. Another significant use of AlN thin-films is to fabricate piezoelectric sensors and actuators [5].

The piezoelectric properties of AlN strongly depend on the crystallographic orientation. Highly c-axis oriented AlN ((002) texture) thin films are preferred for piezoelectric applications because of a high d_{33} (5.0961 pm) [6, 7]. Furthermore, the coupling coefficient of AlN thin film-based devices is closely related to the c-axis orientation of the deposited film [8].

In order to yield a highly c-axis AlN films, numerous research groups investigated the influence of deposition parameters on the crystal orientation of the deposited films. The process parameters such as sputtering power, gas ratio, process pressure, and the substrate temperature directly affect the film quality and texture of the deposited films [9].

The substrate temperature largely influences the kinetic energy available to the adatoms on the surface of the deposited films. This energy increases proportionally with an increase in substrate temperature, which helps in depositing highly c-axis oriented films [10, 11]. However, after the optimal temperature range, a further increase in the substrate temperature increases the thermal stresses in the film because of the coefficient of thermal expansion (CTE) difference when cooling down to room temperature, and the number of impurity inclusions from the sputtering systems [8]. From the literature review, several researchers discussed the influence of substrate temperature on the AlN (002) thin film on different substrates. Barshiha et al. [12] were able to deposit a highly c-axis oriented AlN film at a substrate temperature of 100 °C on the Si and glass substrates. They observed the decrease in (002) diffraction peaks while other diffraction peaks (100), (101), and (102) started to appear when the substrate temperature was increased to 200 °C and 350 °C on Si substrate. Ababneh et al. [13] observed the deposition of highly c-axis oriented on AlN thin films on silicon substrates. The substrate temperature was measured as 150 °C at a plasma power of 500W under low sputtering pressure (1.5 mTorr) and pure nitrogen atmosphere. Hao et al. [10] studied the influence of substrate temperature on the AlN films as the substrate temperature was increased from 60 °C to 520 °C. They observed significant effects on crystal orientation, surface morphology and the deposition rate, with optimal substrate temperature of 430 °C.

Kar et al. [14] studied the correlation between electrical properties (insulator charge density and interface state density) and surface morphology of AlN films on p-type Si substrates at substrate temperature of 100 °C to 400 °C. They observed that highly c-axis films were deposited between 200 °C and 300 °C with a FTIR absorption peak at 682 cm⁻¹. Chiu et al. [6] deposited AlN (002) on the Pt electrode in the substrate temperature range between 250–450 °C and observed the minimum rocking curve FWHM value of 2.7 ° at a substrate temperature of 400 °C. They explained that high adatom mobility increased its surface diffusion length, which helped the adatom to migrate to the proper site of the (002) plane. Kuang et al. [7] investigated the influences of deposition temperature in the range of 30–700 °C on the chemical composition, crystalline structure, and surface morphology of the AlN (002) films on a sapphire substrate. They concluded that a substrate temperature of 300 °C assists in highly c-axis oriented crystalline structure and surface morphology of deposited films.

It is clear from the literature review that highly c-axis oriented AlN thin films were successfully produced at some ranges of substrate temperatures on various substrates. What is lacking is an investigation of deposition temperature in work that used buffer layers between the AlN (002) and the substrates to reduce the CTE difference. In our previous publication [15], we achieved a highly c-axis oriented AlN thin film on top of a Si (111) substrate with a 3C-SiC (111) buffer layer. We achieved consistent crystal quality using from 40 % to 100 % N₂/Ar ratio, which has been attributed to the lower lattice mismatch of 1 %. In this work, the first aim is to investigate the role of deposition temperature on the deposition of AlN (002) on top of a Si (111) substrate with 3C-SiC (111) as a buffer layer. It should be noted that the CTE difference between AlN (002) and 3C-SiC (111) is 18 % [16].

The second aim of this paper is to investigate the role of the deposition temperature to deposit an AlN (002) film on top of the on-axis and the 4° off-axis 3C-SiC-on-Si (111) substrates. From a literature review, the 3C-SiC layer being grown on Si substrates has structural defects because of the lattice mismatch (~20 %) and the CTE difference (~8 %) [17]. Therefore, several groups grew a 3C-SiC layer on top of an off-axis Si substrate to mitigate the problem, as described herein. Powell et al. [18] observed that all traces of anti-phase disorder were eliminated in 3C-SiC films grown on off-axis substrates, whereas all of the as-grown on-axis films exhibited an irregular shaped line. Wang et al. [19] reported that the 3C-SiC film grown on 4° off-axis Si substrates had smaller surface roughness, narrower FWHM peak and smaller bow magnitude compared to the ones that were grown on on-axis Si substrates. Severino et al. [20] deposited a 3C-SiC (111) film on top of a 3° off-axis Si substrate. They observed that the stacking fault density decreased dramatically compared to the films grown on top of the on-axis Si (111) substrates. They also concluded that the off-axis Si substrate helps in the suppression of double positioning boundaries. The same group grew 3C-SiC films on top of 150 mm (111) Si wafers 4° off-axis towards the [110] direction. They reported an extremely flat surface and interface of SiC film that can be potentially used for electrical and mechanical device applications [21]. Based on this literature review, the expectation is that the 4° off-axis 3C-SiC-on-Si (111) substrate provides a better template compared to an on-axis 3C-SiC-on-Si (111) template for the deposition of highly c-axis oriented AlN because of the lower surface roughness and stacking fault density of the 3C-SiC layer.

2. Experimental Details:

Prior to the AlN deposition, the 3C-SiC thin film of 80 nm thick was epitaxially grown on both on-axis (off-cut angle 0.5°) and off-axis Si (111) with the off-cut angle of 3.5 ± 0.5° towards [110] plane of 150 mm diameter in a custom-made hot-wall horizontal low pressure chemical vapour deposition (LPCVD) system at 1000 °C using alternating supply epitaxy method at Griffith University [22]. The rms value of surface roughness of the on- and off-axis SiC/Si substrate was measured as 2.386 nm and 0.93 nm, respectively. Initially, the 3C-SiC/Si wafers were cut to the size of 15 mm by 15 mm samples using a Dico dicer. The samples were then cleaned via a standard piranha cleaning process to remove the organic substances, followed by submersion in a diluted 1% HF acid for 5 minutes to remove oxidation.

The pulsed DC sputtering of the AlN thin film on top of the 3C-SiC-on-Si (111) substrate was performed using a magnetron sputtering system (Surrey NanoSystems Gama 1000) at 1800 W sputtering power. The pulsed DC power supply (Pinnacle Plus, Advanced energy) was utilized at 250 KHz with time off of 0.4 μs

to avoid electrical arcing. The sputtering system was turbo-pumped down to the base pressure of 2×10^{-8} Torr, using the cryogenic pump, followed by constant pumping throughout the sputtering. The low base pressure prevented the incorporation of oxygen into the AlN thin films. The main chamber was purged with 15 sccm of 99.999 % Ar gas for 3 minutes before the samples loading to avoid contamination. The samples were inserted into the main chamber via a two-stage loading system. The samples were then heated to 300 °C with an IR heater for 3 minutes to remove moisture. We employed an aluminum target of 100 mm in diameter with 99.999 % purity while the target to substrate spacing was set to 20 cm. R.F. reactive ion etching was carried out on the SiC surface to clean it to improve adhesion with AlN film [23]. All the sputtering was performed at a process pressure of 2 mTorr and 58 % of N₂/Ar ratio in reactive mode at a total flow rate of 60 sccm, which was determined via a poison run as explained in one of our previous works [24]. The substrate temperature was increased from 250 °C to 450 °C in a steps of 50 °C. Depositions lasted for 44 minutes, resulting in AlN thicknesses of 548 nm to 686 nm, depending on the deposition rate.

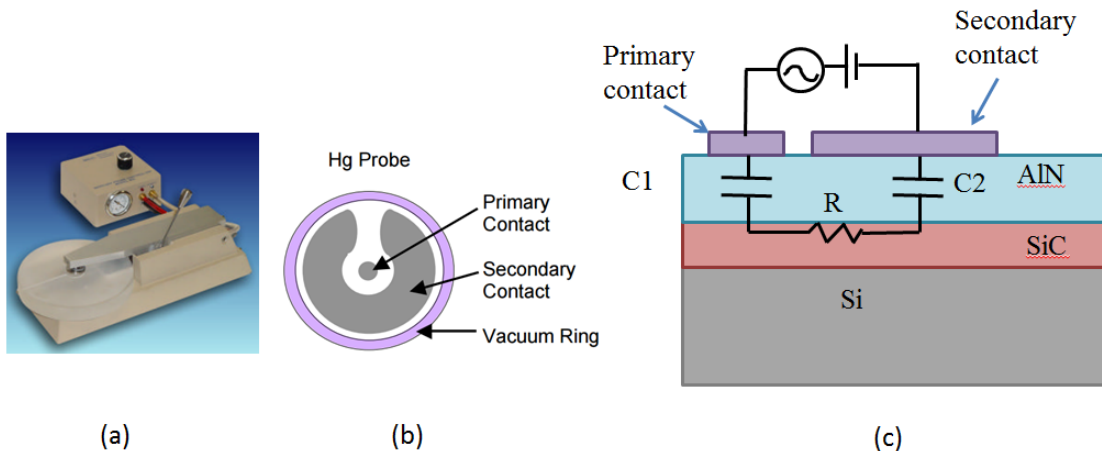


Fig. 1 (a) MDC Mercury Probe equipment (b) Head description of Mercury probe (c) Schematic of capacitance measurement

After the successful deposition of c-axis AlN films, we also extracted the piezoelectric coefficient (d_{33}) of the films from the capacitance-voltage (C-V) measurement. This measurement was performed using MDC mercury probes in dual front contact mode that was connected to C-V plotter. MDC Mercury probes were used to form contacts and served as top and bottom electrodes to the AlN film. Fig 1(a) shows the image of the MDC probe equipment.

The schematic of the head of the mercury probe unit is shown in Fig 1 (b). It consists of an outer vacuum ring, and two mercury probes. The area of the primary probe is much smaller compared to the secondary probe. The schematic of the capacitance measurement is shown in Fig 1 (c). The mercury probes are connected in dual front contact mode on the AlN as shown in Fig 1(c). The AlN is an insulator which acts as a dielectric while the mercury probes and the SiC acts as a parallel plate capacitor. The electric field develops across the dielectric AlN when the electric potential is applied on the mercury probes as shown by C1 and C2. The magnitude of C1 is smaller (because of smaller electrode area) compared to the value of C2. However, the net capacitance is approximately equal to the value of C1 because both capacitors are connected in series. When a DC voltage of -20V to +20V in increments of 10 V were applied, the thickness of the AlN piezoelectric layer contracted or expanded, respectively. The capacitance value can be calculated as follows. Given that AlN dielectric constant = $9.5 \times 8.85 \times 10^{-12}$ F/m, thickness = 475 nm, and area = 4.8×10^{-7} m², the value of the capacitance (C_0) = 84.75×10^{-12} F at zero DC bias. The change in the capacitance value (C_V) can be calculated using the capacitance parallel plate formula [25, 26]:

$$C_V = C_0 \left(\left(1 - \left(\frac{\Delta A}{A} \right) \right) / \left(1 + \left(\frac{\Delta d}{d} \right) \right) \right) \quad (1)$$

where both the vertical extension of the AlN material Δd , and the variation in area ΔA are correlated with the magnitudes of both the longitudinal d_{33} and the transverse d_{31} charge constants as follows [27]:

$$\Delta d = V|d_{33}| \quad (2)$$

$$\Delta A = \frac{V|d_{31}|A}{d} \quad (3)$$

Moreover, the magnitude of the d_{33} coefficient is about twice the value of d_{31} [27]; therefore,

$$|d_{33}| = 2|d_{31}| \quad (4)$$

Solving for Δd , we get equation 5:

$$\Delta d = d \left(\frac{1-C_r}{0.5+C_r} \right) \quad (5)$$

where C_r is the ratio between C_V and C_o , V is the voltage applied on the capacitor plates.

The deposited AlN films were characterized by the following parameters (the names of equipment): grazing angle incident X-ray diffraction (Bruker D8) using monochromator Cu K α 1 beam with $\lambda=1.5405980$ Å, rocking curve X-ray diffraction (Panalytical Empyrean XRD), deposition rate (Nanospec AFT 180); residual stress (Tencor Flexus 2320 system), surface roughness (Park NX20 AFM), surface morphology (Raith150 TWO) and C-V measurement (MDC mercury probes connected with CV plotter).

3. Results and Discussion:

Table I summarizes the characterization results for all samples. The data are divided into two different categories. Samples Y1 to Y5 correspond to AlN deposition on on-axis 3C/Si substrates, while samples Z1 to Z5 correspond to AlN deposition on off-axis 3C/Si substrates. The general trends are the followings. The deposition temperature has a major influence on the characteristics of the AlN films on top of on-axis SiC/Si substrates. The deposition temperature of 400 Celcius is the optimal value. Interestingly, the characteristic of the AlN films on top of off-axis SiC/Si substrates remains relatively constant at different deposition temperatures. Furthermore, the AlN film on top of the off-axis substrates has better quality compare to the one on top of on-axis substrates. The characterized parameters are the peak position, FWHM of the diffraction peak, percentage of <002> area under the curve, FWHM of rocking curve, surface roughness, in-plain stress, grain sizes, refractive index, deposition rate and thickness. The detailed discussion for each parameter is provided in the subsequent paragraphs, with supporting graphical evidence.

Figure 1 (a) shows the 1° incidence grazing angle x-ray diffraction (GIXRD) scan for the samples deposited on on-axis 3C-SiC/Si substrates. The GIXRD measurement at 1° incidence was employed due to the lower thickness of AlN films compared to the substrates. A major diffraction peak is observed at 36.2 ° in all samples depicting the (002) orientation. Other minor diffraction peaks can be seen at 38 ° and 50 ° associated with (101) and (102) orientations, respectively. The percentage of (002) to other AlN crystal orientations is calculated as being between 77–98 % for all samples by measuring the area under the curve. The XRD diffraction peaks reveal that the crystalline quality increases with increase in deposition temperature from 250 to 350 °C. The FWHM values are extracted from the diffraction peaks using Gaussian fitting because of better curve fitting for all the curves compared to Lorentz fitting [29, 30]. Highly c-axis oriented AlN is deposited at 350 °C and 400 °C based on the FWHM of the diffraction peak and the area under the curve for (002) orientation. The crystalline quality of deposited films degrades with a further increase in substrate temperature of 450 °C, as the other minor peaks are visible in XRD diffraction spectra and there is a decrease in the area under the curve for (002) orientation. Figure 2 (b) shows the FWHM of the rocking curve indicating a (002) orientation for samples deposited on on-axis 3C-SiC/Si substrates. The values are 3.84° and 3.71° for the

samples deposited at 250 °C and 300 °C, respectively, as given in Table 1. The values decrease to 3.47° and 2.58° with further increase in substrate temperature from 350 °C and 400 °C, revealing the improvement in AlN (002) crystal quality. Finally, the FWHM value decreases to 3.04 ° at the substrate temperature of 450 °C, in agreement with the literature [6] [10].

Table I. Result of the samples prepared at different deposition parameters

Sample On SiC(111)	Sample ID	Substrate temp	Peaks position <36° <002>>	FWHM Of Diffraction peak (O)	FWHM Of Rocking Curve (O)	Percentag e of <002>*	Grain size (nm)	Surface Rough ness (nm)	Biaxial stress from XRD (GPa)	Deposition rate (nm/min)	Thickness (nm)	Stress** (MPa) (Tensile)
On-Axis SiC(111)	Y1	250	36.18	0.30	3.84	77.3	29.11	3.46	2.906	15.1	665	333.9
	Y2	300	36.183	0.32	3.71	78.3	27.29	3.82	2.905	14.6	648	336.4
	Y3	350	36.16	0.29	3.47	97	30.11	3.99	2.47	14.8	657	342
	Y4	400	36.17	0.276	2.58	99	31.63	3.35	2.69	15.4	686	326.5
	Y5	450	36.19	0.295	3.04	78.3	30	3.86	3.13	15.3	680	317.9
Off-Axis SiC(111)	Z1	250	36.15	0.31	2.78	93.25	28.16	2.63	2.26	15.1	665	-
	Z2	300	36.19	0.31	2.75	90.5	28.16	2.92	3.13	14.6	648	-
	Z3	350	36.15	0.32	2.34	95	27.29	2.65	2.26	14.8	657	-
	Z4	400	36.13	0.33	2.6	100	26.46	2.38	1.824	15.4	686	-
	Z5	450	36.16	0.31	1.91	100	28.16	2.82	2.47	15.3	680	-

*The observed XRD peaks can be assigned to wurtzite AlN phase (Card # 01-070-2545). The peak at $2\theta = 36.023^\circ$ [28]

** Percentage of <002> is calculated by measuring the area under curve for all AlN orientations in the XRD spectra

***In-plane stresses are measured without applying RF bias voltage on the substrate

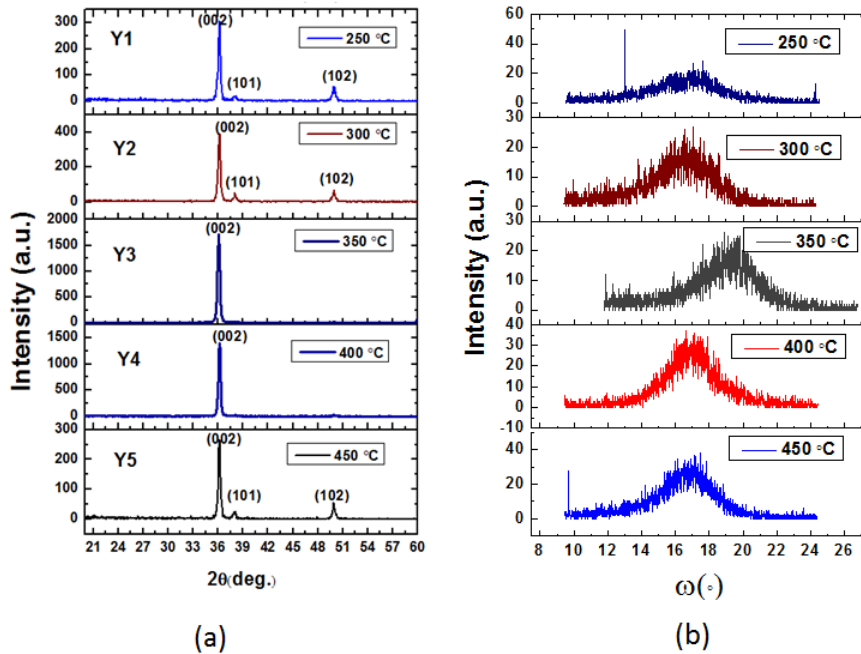


Fig. 2 (a) GIXRD spectra of AlN deposited on top of on-axis 3C-SiC/Si substrates

Fig. 2 (b) FWHM of rocking curve of AlN (002) deposited on top of on-axis 3C-SiC/Si substrates

Figure 3(a) shows the GIXRD spectra of the AlN films sputtered on top of 4° off-axis 3C-SiC/Si substrates at different substrate temperatures. The major diffraction peak is observed around a 2θ angle of 36.2° indicating a (002) orientation. The percentage of (002) to other AlN crystal orientations is calculated to lie between 90–100 % for all samples. Figure 3(b) shows the FWHM of the rocking curve indicating a (002)

orientation. The values are 2.78° and 2.75° at a substrate temperature of $250\text{ }^\circ\text{C}$ and $300\text{ }^\circ\text{C}$, respectively. Then, the rocking curve values decrease to 2.34° , 2.6° and 1.91° with an increase in substrate temperatures of $350\text{ }^\circ\text{C}$, $400\text{ }^\circ\text{C}$ and $450\text{ }^\circ\text{C}$, respectively. The XRD results reveals that the substrate temperature in the range of $350\text{ }^\circ\text{C}$ to $450\text{ }^\circ\text{C}$ provides the optimum range of kinetic energy and adatoms mobility that assists in obtaining highly c-axis oriented AlN(002) material suitable. This is the main difference from the results found for the AlN films deposited on on-axis 3C-SiC/Si substrates. The physical explanation for this remains unclear and has not been discussed in the literature.

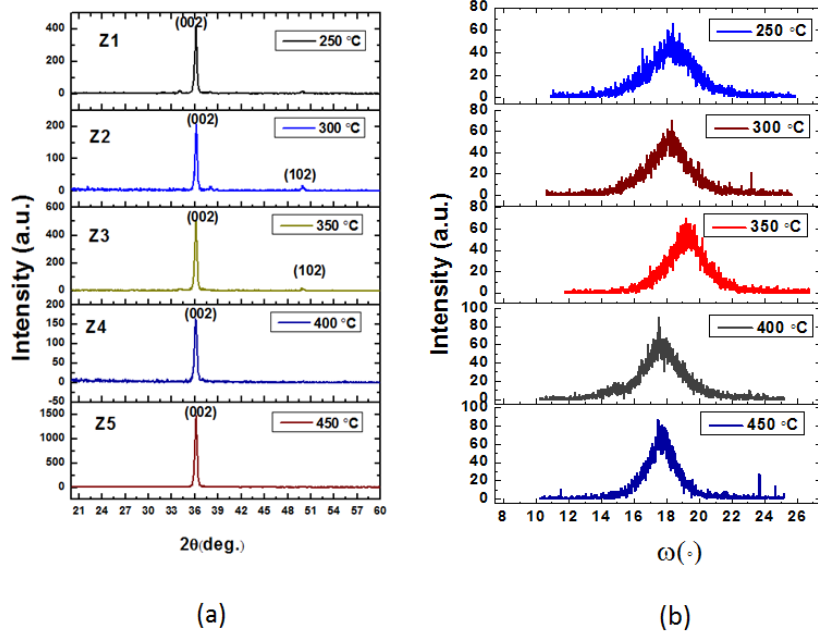


Fig. 3 Grazing angle XRD of AlN deposited on (a) Off-axis 3C-SiC-on-Si (111) (b) FWHM of rocking curve of AlN(002) on Off-axis 3C-SiC-on-Si (111) film.

We calculate the grain sizes of all samples using the Scherrer's equation [31]. The values are provided in Table I. There is 15.7 % difference between the highest and the lowest values of the grain size of the samples on the on-axis substrates, while the difference decreases to 6.4 % in the case of samples on top of the off-axis substrates.

Figure 4 shows the top-view SEM images of the surface of AlN films deposited on on-axis SiC/Si substrates at various deposition temperatures. All the film has some hillocks (rough surface structure) that probably originated from low adatom mobility due to tensile stress [32, 33]. This hypothesis is supported by the stress values in Table 1, as the decrease in hillock number is observed in Figure 4 (d) and 3 (e) due to the low in-plane stress at the deposition temperature of $400\text{ }^\circ\text{C}$ and $450\text{ }^\circ\text{C}$. Most importantly, at $400\text{ }^\circ\text{C}$, the films show dense microstructures and the uniform pebble-like grains, indicating the typical growth the (002) orientation.

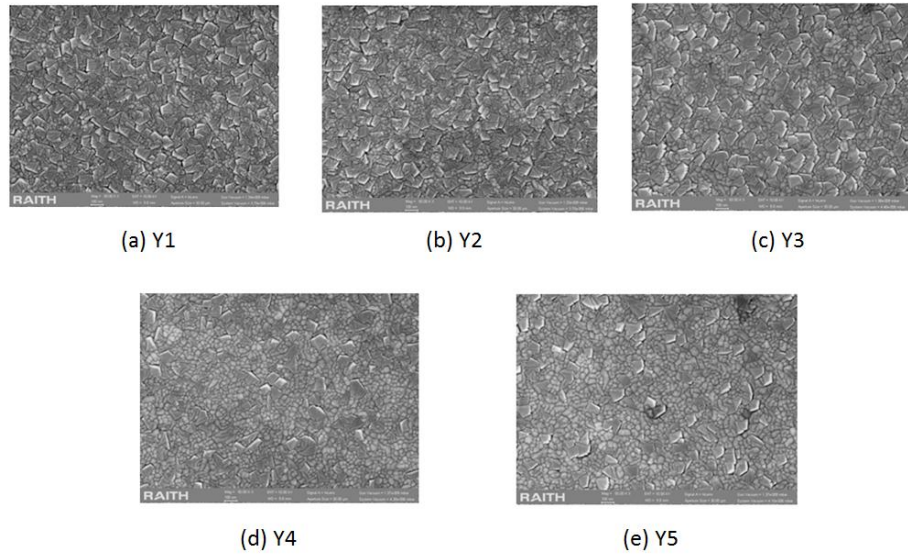


Fig. 4 SEM images of AlN deposited on top of on-axis 3C-SiC/Si substrate at (a) 250°C (b) 300°C (c) 350°C (d) 400°C (e) 450°C

The root mean square (RMS) roughness of the deposited films was measured in a $5 \mu\text{m} \times 5 \mu\text{m}$ area using contact mode Atomic Force Microscopy (Park AFM) with a silicon cantilever. Figure 5 shows the scan images of AFM for all the samples. The results from Table 1 demonstrate that the roughness (in root mean square) of the AlN layer was measured in the range of 3.40 nm to 3.99 with no specific trend as a function of substrate temperature.

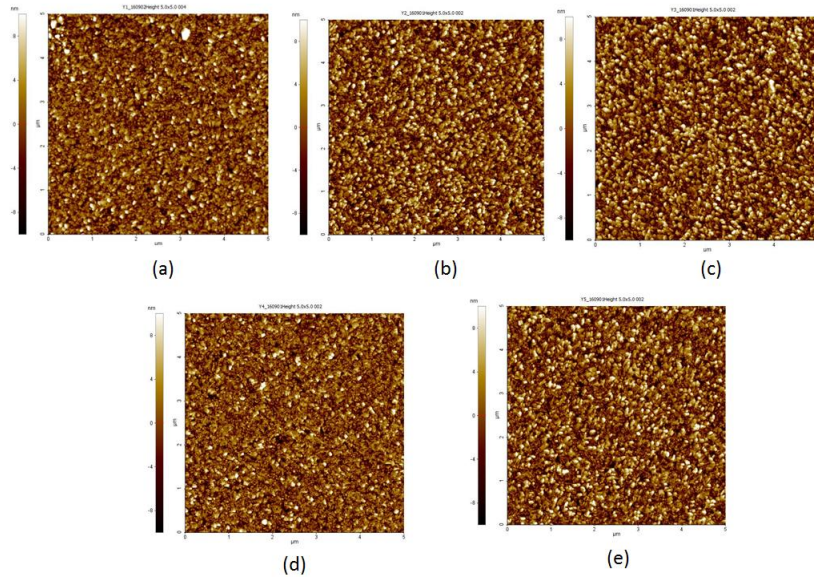


Fig. 5 AFM scan of AlN deposited on top of on-axis 3C-SiC/Si substrate at (a) 250°C (b) 300°C (c) 350°C (d) 400°C (e) 450°C

The SEM images of AlN films deposited on top of off-axis SiC/Si substrate at various substrate temperatures are shown in Figure 6. All the film has growth hillock (rough surface structure) that are probably originated from low adatoms mobility due to tensile stress [32]. However, the hillocks are still less in number compared to the ones that were deposited on top of on-axis SiC/Si substrates. The hillock formation is correlated

with the residual stress during the deposition process [33]. However, due to unavailability of 150 mm off-axis SiC/Si wafer, we weren't able to measure and relate the residual stress in AlN film deposited on Off-axis SiC/Si substrate to the hillock density. The AFM images give information about surface roughness while the SEM images gives us more information about grain size and shape (hill locks).

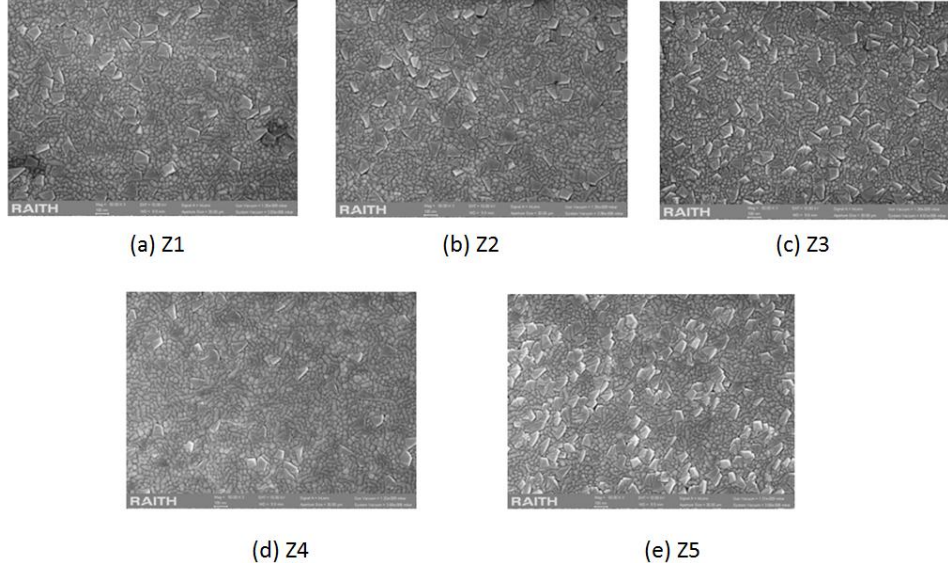


Fig. 6 SEM images of AlN deposited on top of off-axis 3C-SiC/Si substrate at (a) 250°C (b) 300°C (c) 350°C (d) 400°C (e) 450°C

The AFM scan of the AlN films deposited at different substrate temperatures on top of off-axis 3C-SiC/Si substrates is shown in Figure 7. The results from Table 1 demonstrate that the roughness (in root mean square) was in the range of 2.38 nm to 2.82 nm for the substrate temperature from 250 °C to 450 °C. The surface roughness of AlN films deposited on top of off-axis 3C-SiC/Si substrates is relatively lower compared to the ones deposited on top of on-axis 3C-SiC/Si substrates. This is due to relatively lower surface roughness of the off-axis SiC/Si substrate compared to the On-axis SiC/Si substrate.

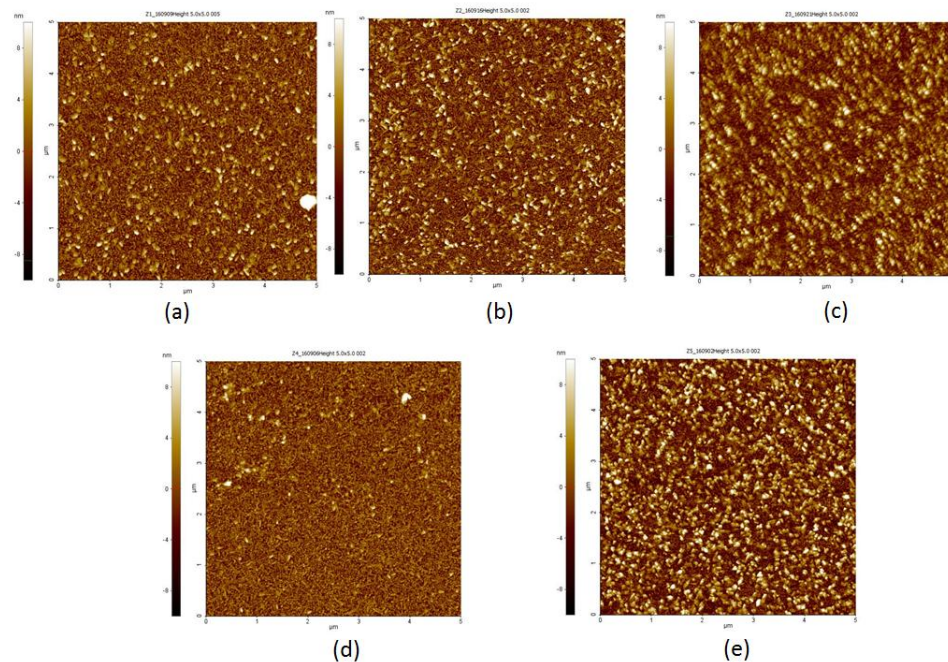


Fig. 7 AFM scan of AlN deposited on top of off-axis 3C-SiC/Si substrate at (a) 250°C (b) 300°C (c) 350°C (d) 400°C (e) 450°C

In order to provide additional evidence on the successful deposition, cross-section SEM image of AlN film of Z3 on top of off-axis 3C-SiC/Si substrate is shown in Figure 8 deposited at substrate temperature of 350 °C. This image clearly shows columnar growth of an AlN thin film along the c-axis orientation that is perpendicular to the plane of the substrate. The SEM image also shows that the 3C-SiC layer grown on top of off-axis Si substrate is tilted towards the left direction.

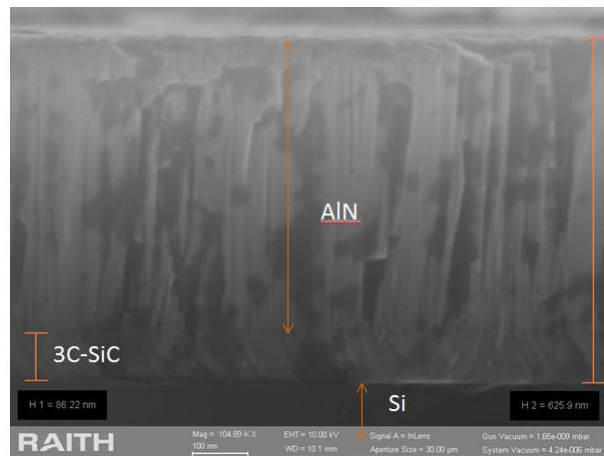


Fig. 8 Cross-section SEM image of AlN grown on Off axis 3C-SiC/Si(111) substrate

The in-plane stress of the AlN films were performed using separate samples that were deposited on top of the 50 mm wafers. The change in the wafer's curvature before and after AlN deposition was measured using the

Tencor Flexus 2320 system. This value is then inserted into Stoney equation to calculate the stress:

$$\sigma = \frac{E}{6(1-\nu)} \frac{t_s^2}{t_f} \left(\frac{1}{r_c} - \frac{1}{r_u} \right) \quad (6)$$

where E, ν , t_s and t_f are the Young's modulus, Poisson's ratio for the silicon substrate, silicon thickness and AlN film thickness, respectively. r_u and r_c are the radii of curvature of the substrates before and after AlN deposition, respectively. The stresses for all the five samples prepared on top of on-axis SiC/Si substrate, are measured in range of 317 MPa to 342 MPa and are tensile in nature. We could not perform the same measurements for the samples on top of the off-axis substrates due to the unavailability of the 50 mm wafer for them.

The deposition rate and the thickness of the AlN layers were measured via separate AlN sputtered samples on top of doped p-type Si (100) wafers employing a Nanospec AFT 180 instrument in non-contact mode. The values are identical for samples on both on-axis and off-axis substrates since they are batch-fabricated. The deposition rate was measured as 15.1 nm/min at 250 °C, which was decreased to 14.6 nm/min and 14.8 nm/min at 300 °C and 350 °C. The deposition rate increased again to 15.4 nm/min at 400 °C. There is 5.47 % difference between the highest and the lowest values, which indicates that the deposition rate is independent of substrate temperature. All the sputtering was carried out for 45 min, which results in the film thickness from 648 to 686 nm.

The biaxial stress (σ) was calculated using the following equation:

$$\sigma = -812.41 \times 10^9 ((c - c_0)/c_0) \quad (7)$$

where c_0 is the strain-free lattice parameter ($c_0 = 4.9795 \text{ \AA}$) measured of AlN powder sample [33]. The value of c was extracted from the experimental data as follows: $c = 2d$, where $d = \lambda/2 * \sin \theta$ from Braggs law, where $\lambda = 1.5405980 \text{ \AA}$ and θ is diffraction angle from XRD 2θ plot.

The biaxial stress was calculated as 2.906 GPa at 250 °C deposition temperature for the AlN film on top of on-axis 3C-SiC/Si substrate, which then decreases to 2.47 GPa at 350 °C deposition temperature, as shown in Table 1. This biaxial stress increases again to 3.13 GPa at 450 °C substrate temperature. This trend is consistent with the trend for the crystal quality in term of the FWHM of rocking curve, where the optimum deposition temperature is around 350 °C. Compared to the bi-axial stress of the AlN films on top of off -axis 3C-SiC/Si substrates, the latter have lower values between 2.26 GPa and 1.824. Again, this is consistent with the lower values of the FWHM of rocking curve.

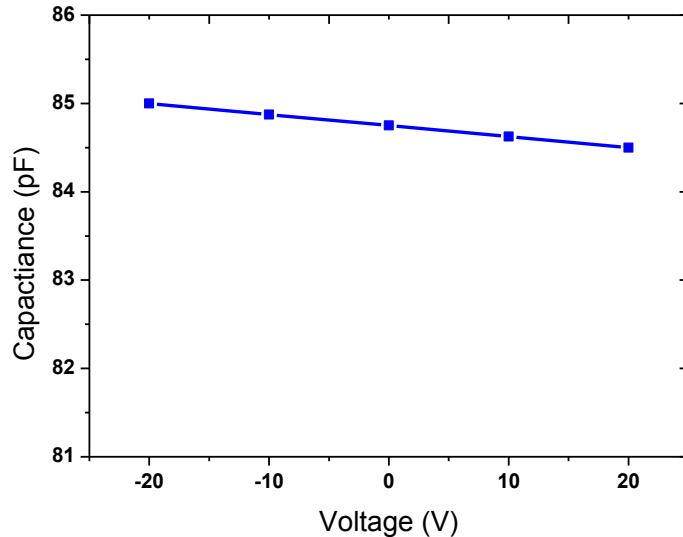


Fig. 9 The plot of capacitance vs. DC bias voltages at 1 KHz frequency

Figure 9 shows the plot of capacitance versus DC voltages at frequency of 1 kHz for the Z3 sample. The capacitance value is measured around 85.75×10^{-12} F at zero applied DC voltage, which matches the calculation for the C_o . We calculate the longitudinal charge constant d_{33} based on Equation 2 [26]. The change in vertical extension Δd (thickness) was calculated from Equation 5, where the value of C_r , which is 0.997 and 1.002 for +25 V and -25 V, respectively, and the value of d (thickness) = 657×10^{-9} m. We obtained the d_{33} values of 47 pm/V, which is approximately 10 times higher than the value reported for an AlN (5.31 pm/V) [34]. Even though there is a big disparity between our measured value and the bulk AlN, similar range of d_{33} values were reported by Jackson et al. [35] and Hemert et al. [36]. Further work needs to be performed to identify the source of this large difference.

4. Conclusion:

Based on the experimental data, we found that the off-axis 3C-SiC/Si(111) substrate provides a better template compared to on-axis substrate for the successful sputtering of c-axis oriented AlN films. We achieved highly c-axis AlN thin films with FWHM rocking values of 3.84 to 3.04 and 2.78 to 1.9 on on- and off-axis SiC substrates, respectively in the deposition temperature of 250 °C to 450 °C. The surface roughness and the stress values were also smaller for the films deposited on off-axis substrates. This can be attributed to the lower surface roughness and stacking fault density of the 3C-SiC layer, as well as smaller bow magnitude of the off-axis 3C-SiC/Si substrates. These advantages are crucial for the application of AlN (002) thin films in MEMS devices.

References:

- [1] J. Ruffner, P. Clem, B. Tuttle, D. Dimos, and D. Gonzales, "Effect of substrate composition on the piezoelectric response of reactively sputtered AlN thin films," *Thin Solid Films*, vol. 354, pp. 256-261, 1999.
- [2] A. Claudel, Y. Chowanek, E. Blanquet, D. Chaussende, R. Boichot, A. Crisci, *et al.*, "Aluminum nitride homoepitaxial growth on polar and non-polar AlN PVT substrates by high temperature CVD (HTCVD)," *physica status solidi (c)*, vol. 8, pp. 2019-2021, 2011.
- [3] D. Isarakorn, A. Sambri, P. Janphuang, D. Briand, S. Gariglio, J. Triscone, *et al.*, "Epitaxial piezoelectric MEMS on silicon," *Journal of Micromechanics and Microengineering*, vol. 20, p. 055008, 2010.
- [4] V. Cimalla, J. Pezoldt, and O. Ambacher, "Group III nitride and SiC based MEMS and NEMS: materials properties, technology and applications," *Journal of Physics D: Applied Physics*, vol. 40, p. 6386, 2007.
- [5] C. Zuo, N. Sinha, J. Van der Spiegel, and G. Piazza, "Multifrequency pierce oscillators based on piezoelectric AlN contour-mode MEMS technology," *Microelectromechanical Systems, Journal of*, vol. 19, pp. 570-580, 2010.
- [6] K.-H. Chiu, J.-H. Chen, H.-R. Chen, and R.-S. Huang, "Deposition and characterization of reactive magnetron sputtered aluminum nitride thin films for film bulk acoustic wave resonator," *Thin Solid Films*, vol. 515, pp. 4819-4825, 2007.
- [7] X.-P. Kuang, H.-Y. Zhang, G.-G. Wang, L. Cui, C. Zhu, L. Jin, *et al.*, "Effect of deposition temperature on the microstructure and surface morphology of c-axis oriented AlN films deposited on sapphire substrate by RF reactive magnetron sputtering," *Superlattices and Microstructures*, vol. 52, pp. 931-940, 2012.
- [8] G. Iriarte, J. Rodriguez, and F. Calle, "Synthesis of c-axis oriented AlN thin films on different substrates: A review," *Materials Research Bulletin*, vol. 45, pp. 1039-1045, 2010.
- [9] M. Benetti, D. Cannata, F. Di Pietrantonio, E. Verona, A. Generosi, B. Paci, *et al.*, "Growth and characterization of piezoelectric AlN thin films for diamond-based surface acoustic wave devices," *Thin solid films*, vol. 497, pp. 304-308, 2006.
- [10] H. Jin, B. Feng, S. Dong, C. Zhou, J. Zhou, Y. Yang, *et al.*, "Influence of Substrate Temperature on Structural Properties and Deposition Rate of AlN Thin Film Deposited by Reactive Magnetron Sputtering," *Journal of electronic materials*, vol. 41, pp. 1948-1954, 2012.

- [11] W.-J. Liu, S.-J. Wu, C.-M. Chen, Y.-C. Lai, and C.-H. Chuang, "Microstructural evolution and formation of highly c-axis-oriented aluminum nitride films by reactively magnetron sputtering deposition," *Journal of crystal growth*, vol. 276, pp. 525-533, 2005.
- [12] H. C. Barshilia, B. Deepthi, and K. Rajam, "Growth and characterization of aluminum nitride coatings prepared by pulsed-direct current reactive unbalanced magnetron sputtering," *Thin Solid Films*, vol. 516, pp. 4168-4174, 2008.
- [13] A. Ababneh, U. Schmid, J. Hernando, J. Sánchez-Rojas, and H. Seidel, "The influence of sputter deposition parameters on piezoelectric and mechanical properties of AlN thin films," *Materials Science and Engineering: B*, vol. 172, pp. 253-258, 2010.
- [14] J. Kar, G. Bose, and S. Tuli, "Correlation of electrical and morphological properties of sputtered aluminum nitride films with deposition temperature," *Current Applied Physics*, vol. 6, pp. 873-876, 2006.
- [15] A. Iqbal, G. Walker, A. Iacopi, and F. Mohd-Yasin, "Highly c-axis oriented AlN on 3C-SiC-on-Si (111) substrates by DC reactive magnetron sputtering," *Journal of Crystal Growth*, vol. Submitted to, 2016.
- [16] Z. Yong-Mei, S. Guo-Sheng, L. Jia-Ye, L. Xing-Fang, W. Lei, Z. Wan-Shun, *et al.*, "Growth of a Novel Periodic Structure of SiC/AlN Multilayers by Low Pressure Chemical Vapour Deposition," *Chinese Physics Letters*, vol. 24, p. 1753, 2007.
- [17] H.-S. Kong, B. Jiang, J. T. Glass, G. Rozgonyi, and K. More, "An examination of double positioning boundaries and interface misfit in beta-SiC films on alpha-SiC substrates," *Journal of applied physics*, vol. 63, pp. 2645-2650, 1988.
- [18] J. Powell, L. Matus, M. Kuczmarski, C. M. Choref, T. Cheng, and P. Pirouz, "Improved β -SiC heteroepitaxial films using off-axis Si substrates," *Applied physics letters*, vol. 51, pp. 823-825, 1987.
- [19] L. Wang, G. Walker, J. Chai, A. Iacopi, A. Fernandes, and S. Dimitrijev, "Kinetic surface roughening and wafer bow control in heteroepitaxial growth of 3C-SiC on Si (111) substrates," *Scientific reports*, vol. 5, 2015.
- [20] A. Severino, R. Anzalone, C. Bongiorno, M. Italia, G. Abbondanza, M. Camarda, *et al.*, "Towards Large Area (111) 3C-SiC Films Grown on Off-Oriented (111) Si," in *Materials Science Forum*, 2009, pp. 149-152.
- [21] A. Severino, C. Bongiorno, N. Piluso, M. Italia, M. Camarda, M. Mauceri, *et al.*, "High-quality 6inch (111) 3C-SiC films grown on off-axis (111) Si substrates," *Thin Solid Films*, vol. 518, pp. S165-S169, 2010.
- [22] L. Wang, S. Dimitrijev, J. Han, A. Iacopi, L. Hold, P. Tanner, *et al.*, "Growth of 3C-SiC on 150-mm Si (100) substrates by alternating supply epitaxy at 1000 C," *Thin Solid Films*, vol. 519, pp. 6443-6446, 2011.
- [23] C.-M. Lin, W.-C. Lien, V. V. Felmettsger, M. A. Hopcroft, D. G. Senesky, and A. P. Pisano, "AlN thin films grown on epitaxial 3C-SiC (100) for piezoelectric resonant devices," *Applied Physics Letters*, vol. 97, pp. 141907-141907-3, 2010.
- [24] A. Iqbal, G. Walker, A. Iacopi, and F. Mohd-Yasin, "Controlled sputtering of AlN (002) and (101) crystal orientations on epitaxial 3C-SiC-on-Si (100) substrate," *Journal of Crystal Growth*, vol. 440, pp. 76-80, 2016.
- [25] A. Ababneh, M. Alsumady, H. Seidel, T. Manzaneque, J. Hernando-García, J. Sánchez-Rojas, *et al.*, "c-axis orientation and piezoelectric coefficients of AlN thin films sputter-deposited on titanium bottom electrodes," *Applied Surface Science*, vol. 259, pp. 59-65, 2012.
- [26] M. Al Ahmad and R. Plana, "Piezoelectric coefficients of thin film aluminum nitride characterizations using capacitance measurements," *Microwave and Wireless Components Letters, IEEE*, vol. 19, pp. 140-142, 2009.
- [27] N. N. Rogacheva, *The theory of piezoelectric shells and plates*: CRC Press, 1994.
- [28] S. Khan, M. Shahid, A. Mahmood, A. Shah, I. Ahmed, M. Mehmood, *et al.*, "Texture of the nanocrystalline AlN thin films and the growth conditions in DC magnetron sputtering," *Progress in Natural Science: Materials International*, vol. 25, pp. 282-290, 2015.
- [29] J. Komiyama, K. Eriguchi, Y. Abe, S. Suzuki, H. Nakanishi, T. Yamane, *et al.*, "Polarities of AlN films and underlying 3C-SiC intermediate layers grown on (111) Si substrates," *Journal of Crystal Growth*, vol. 310, pp. 96-100, 2008.
- [30] M. Assouar, O. Elmazria, L. Le Brizoual, and P. Alnot, "Reactive DC magnetron sputtering of aluminum nitride films for surface acoustic wave devices," *Diamond and related materials*, vol. 11, pp. 413-417, 2002.

- [31] D. Song, P. Widenborg, W. Chin, and A. G. Aberle, "Investigation of lateral parameter variations of Al-doped zinc oxide films prepared on glass substrates by rf magnetron sputtering," *Solar energy materials and solar cells*, vol. 73, pp. 1-20, 2002.
- [32] S.-H. Lee, K. H. Yoon, D.-S. Cheong, and J.-K. Lee, "Relationship between residual stress and structural properties of AlN films deposited by rf reactive sputtering," *Thin Solid Films*, vol. 435, pp. 193-198, 2003.
- [33] J. A. Thornton and D. Hoffman, "Stress-related effects in thin films," *Thin solid films*, vol. 171, pp. 5-31, 1989.
- [34] M. Tanaka, S. Nakahata, K. Sogabe, H. Nakata, and M. Tobioka, "Morphology and X-ray diffraction peak widths of Aluminum Nitride single crystals prepared by the sublimation method," *Japanese journal of applied physics*, vol. 36, p. L1062, 1997.
- [35] K. Tonisch, V. Cimalla, C. Foerster, H. Romanus, O. Ambacher, and D. Dontsov, "Piezoelectric properties of polycrystalline AlN thin films for MEMS application," *Sensors and Actuators A: Physical*, vol. 132, pp. 658-663, 2006.
- [36] N. Jackson, O. Z. Olszewski, L. Keeney, A. Blake, and A. Mathewson, "A capacitive based piezoelectric AlN film quality test structure," in *Microelectronic Test Structures (ICMTS), 2015 International Conference on*, 2015, pp. 193-197.
- [37] T. van Hemert, D. Sarakiotis, S. Jose, R. Huetting, and J. Schmitz, "Exploring capacitance-voltage measurements to find the piezoelectric coefficient of aluminum nitride," in *Microelectronic Test Structures (ICMTS), 2011 IEEE International Conference on*, 2011, pp. 69-73.

Chapter 7: Effect of Substrate Temperature and Sputtering Power on the Quality of AlN (002) films Sputtered on Top of 3C-SiC(100)/Si (100) Substrates

Chapter 7: Effect of substrate temperature and sputtering power on the quality of AlN (002) films sputtered on top of 3C-SiC(100)/Si (100) substrates

A. Iqbal¹, G. Walker¹, L. Hold¹, A. Fernandes², A. Iacopi¹ and F. Mohd-Yasin¹

¹*Queensland Micro- and Nanotechnology Centre, Griffith University, Nathan, 4111, QLD, Australia*

²*Bluglass Ltd., 74 Asquith Street, Silverwater, 2128, NSW, Australia*

Abstract

Aluminum nitride (AlN) thin films are successfully deposited on 3C-SiC/Si (100) substrates using a pulsed DC magnetron sputterer. The sputtered films are characterised the following parameters: FWHM of diffraction peak and FWHM of the rocking curve (Panalytical Empyrean X-Ray diffraction tool), deposition rate (Nanospec AFT 180), surface roughness (Park AFM), surface morphology (Raith150 Two) and in-plane stress (Tencor Flexus 2320 System). The data shows that a substrate temperature of 350 °C and high sputtering power between 1800 to 2400 W produce highly c-axis oriented films with the lowest FWHM of the rocking curve value of 2.12° and the lowest residual stress of 230 MPa (tensile). Such advances are crucial for the application of AlN film for piezoelectric MEMS devices.

Keywords: A3. Physical vapour deposition processes; A3. Polycrystalline deposition; A1. X-ray diffraction; B1. Nitride; B1. Silicon carbide

1. Introduction

Aluminum Nitride (AlN) could potentially be used in high power electronics because of its wide bandgap (6.2 eV), high thermal conductivity ($3.3 \text{ WK}^{-1}\text{cm}^{-1}$) and high electrical resistivity ($10^{15} \Omega\text{.cm}$) [1-3]. AlN could also be used to fabricate RF MEMS, piezoelectric sensors and actuators because of its high acoustic velocity (12,000 m/s) [4, 5]. AlN is preferred as the piezoelectric material in potential high-temperature applications in the automotive, aerospace, and energy industries because of its high Curie temperature (1200 °C) [6], whereas the performance of ZnO and PZT degrade significantly at such temperature [6, 7]. The piezoelectric properties of AlN intensely depend on crystallographic orientation. C-axis oriented AlN i.e. in (002) plane has higher piezoelectric property d_{33} (5.0961 pm/V) compared to other crystal orientations [8, 9]. Also, the electromechanical coupling coefficient (kr^2) (6.5%) of AlN-based devices is closely related to the c-axis orientation of the deposited films [10]. Many research groups have investigated the influence of sputtering parameters on AlN films. They observed the direct effect of sputtering power, gas ratio, process pressure, and substrate temperature on the crystal orientation of the deposited films [11].

The kinetic energy that is available to the adatoms on the surface of the deposited films is directly proportional to the sputtering power. This energy increases the mobility of adatoms and assists them to arrange themselves in the lowest energy state of c-axis-orientation. Several publications have documented this effect. Kusaka et al. [12] observed the increase of the grain size and the enhancement of c-axis oriented AlN films deposited on glass substrate with an increasing DC power. Similarly, Vashaei et al. [13], noted an improvement in the crystal quality of AlN (002) films on c-sapphire substrate and its growth rate with increasing RF power. However, both researchers reported the adverse effect of increasing the sputtering power. After the kinetic energy of the adatoms reached the optimum value, the kinetic energy of the secondary atoms was increased as well. These high-energy secondary atoms then attack the substrate surface, causing surface damage and prompting deterioration in the preferred c-axis orientation of the films [12].

In contrast, the kinetic energy and the mobility of adatoms increase with increasing substrate temperature [14, 15]. However, further increase of the substrate temperature after the optimum value deteriorates the quality of the films due to thermal stresses and the number of impurity inclusions from the sputtering systems [10]. Several research groups investigated the influence of substrate temperature on the AlN deposition. Kuang et al. [9] reported the optimum substrate temperature of 300 °C to produce highly c-axis oriented AlN films on top of sapphire substrates. Hao et al. [14] also studied the role of substrate temperature in

the range of 60 °C to 520 °C on the deposition of AlN film on Si (100) substrates. They reported 430 °C as the optimal substrate temperature, achieving a FWHM rocking curve value of 2.25° for AlN (002) films.

Sputtered thin film have both extrinsic- and intrinsic-stresses. The extrinsic (or thermal) stress results from the difference in coefficient of thermal expansion (CTE) between the substrate and deposited film, which is induced by the deposition temperature. The intrinsic stress arises from the lattice mismatch and structural ordering processes that occur during the film growth [16]. Kusaka et al. [12] studied the effect of sputtering power on the residual stress of AlN films deposited on a glass substrate by dc magnetron sputtering. They observed that the residual stresses were obtained at low input power, but changed to compressive stresses at high sputtering power. Zhong et al. [17] investigated the effect of sputtering parameters on the residual stress of AlN films deposited on Si(111) substrates using RF sputtering. They observed that the stress changed from compressive to tensile with a decrease in N₂ concentration and an increase in sputtering pressure, while the substrate temperature and RF power have a minimum effect.

Another method to reduce the residual stress of AlN films is by reducing the CTE difference between the film and the substrates. AlN is typically deposited on a Si substrate due to a lower cost per surface unit area and compatibility with CMOS. However, the difference in CTE between both materials is 47 %. Cubic silicon carbide (3C-SiC) is one such potential substrate. It can be epitaxially grown on a Si substrate as a buffer layer to reduce the lattice mismatch and CTE difference to 28.6% and 18%, respectively. The only reported work in the literature on the DC sputtering of AlN (002) on top of Si (100) substrate with 3C-SiC (100) buffer layer is by the Berkeley group [18]. They ramped up the DC power to 5500 W and employ pure nitrogen to achieve a FWHM of rocking curve of 1.73 degree. In our previous work, we have reported the deposition of polycrystal AlN thin films with (002), (100) and (101) orientations on top of the same structure [19]. In the follow up, we are able to control the deposition of (002) and (101) oriented films by tuning the nitrogen concentration [20].

The main contribution of this work is the successful DC sputtering of a highly c-axis AlN film on top of a 3C-SiC/Si (100) substrate, as evidenced by the rocking curve measurement with the lowest value of 2.12°. In contrast to the Berkeley work [18], we are able to achieve the results at a low nitrogen concentration of 58 % and a total gas flow of 60 sccm. Furthermore, we elucidate the role of sputtering power and substrate temperature on the film's crystal quality, morphology and residual stress.

2. Experimental Details:

Prior to this experiment, a 80 nm thick 3C-SiC thin film in (100) plane was epitaxially grown on top of an on-axis Si (100) wafer, which is 150 mm in diameter. A custom-made hot-wall horizontal low-pressure chemical vapour deposition (LPCVD) reactor that employed alternating supply epitaxy performed the said deposition at a temperature of 1000 °C [21]. The surface roughness of the 3C-SiC (100) film was measured to be about 2 nm (rms). For maintaining the base uniformity in our experiment, AlN depositions were performed using the 3C-SiC/Si (100) samples that were diced from the same wafer.

The DC sputtering of the AlN films on top of the 3C-SiC/Si (100) substrates was performed using a DC magnetron sputtering system (Surrey NanoSystems Gama 1000) with a pulsed DC supply (Pinnacle Plus). Initially, the samples of 15 mm by 15 mm in dimension were passed through a standard piranha cleaning process to remove the organic substances. The oxidation on the samples was removed by submerging them in a diluted 1% HF acid for 5 minutes. The sputtering system was turbo-pumped down to the base pressure of 2×10^{-8} Torr, followed by a constant pumping through the cryogenic pump to prevent the incorporation of oxygen into the chamber. The samples were inserted into the main chamber via a two-stage loading system. Before loading into the main chamber, the samples were placed on a susceptor and heated in a turbo-pumped vacuum load lock at 200 °C for 3 minutes to reduce moisture, while the main chamber was purged with Ar for 3 minutes to reduce contamination. The face of the 100 mm diameter 99.999% Al target was set at 20 ° off perpendicular to the susceptor. The distance between the centre of the target and susceptor was 20 cm. The susceptor was rotated at 10 rpm during all depositions. All the sputtering was performed at a process pressure of 2 mTorr and a 58 % of N₂/Ar ratio in reactive mode at a total flow rate of 60 sccm, which was determined via a poison run as explained in our previous article [20].

In the first part of the experiment, we performed all the sputtering at 1800 W while keeping all other sputtering parameters constant. We increased the substrate temperature from 250 °C to 450 °C in steps of 50 °C. All these depositions lasted for 44 minutes, resulting in AlN thicknesses of 548 nm to 686 nm, depending on the deposition rate. In the second part of the experiment, we set the substrate temperature at 350 °C, while increasing the sputtering power from 1200 W to 2400 W in steps of 300 W. All other sputtering parameters were kept constant. The sputtering was performed from 28 to 44 minutes as given in Table 1, resulting in AlN thicknesses of 504 nm to 647 nm, respectively.

The deposited AlN films were characterized by the following parameters (the names of equipment): normal scan X-ray diffraction (Panalytical Empyrean XRD using monochromatized Cu K α 1 beam with $\lambda=1.5405980 \text{ \AA}$); omega scan rocking curve (Panalytical Empyrean XRD with a fixed anti-scatter slit PIXcel-3D detector: the open detector mode was used with an increment of 0.1°/step and the duration of each step is 0.352 s); surface roughness (Park AFM); deposition rate (Nanospec AFT 180); residual stress (Tencor Flexus 2320 system); and surface morphology (Raith150 Two).

3. Results and Discussion:

Table I. Results of the samples prepared at different deposition parameters

Sample ID	Substrate temp (°C)	Sputtering Power (W)	Peaks position (36° <002>)	FWHM of Diffraction Peak (°)	FWHM of Rocking Curve (°)	Deposition rate (nm/min)	Thickness (nm)	Surface Roughness (nm)	Grain size (nm)	Stress** (MPa) (tensile)
X1	250	1800	36.18	0.18	3.38	15.1	665	3.40	48.51	380.1
X2	300	1800	36.18	0.18	2.85	14.7	648	3.109	48.5	313.6
X3	350	1800	36.16	0.13	2.37	14.9	657	2.899	67.1	322.6
X4	400	1800	36.19	0.12	2.38	15.6	686	2.57	72.7	315
X5	450	1800	35.6	0.11	2.12	15.4	680	2.67	79.3	308
X6	350	1200	36.17	0.11	2.6	10.3	620	3.99	79.3	432.7
X7	350	1500	36.18	0.15	2.7	12.4	623	3.7	58.2	333.5
X3	350	1800	36.16	0.13	2.37	14.9	657	2.89	67.1	322.6
X8	350	2100	36.19	0.18	2.51	15.9	620	2.30	48.2	300
X9	350	2400	35.7	0.15	2.22	18	504	2.63	58.2	230

*The observed XRD peaks can be assigned to wurtzite AlN phase (Card # 01-070-2545) with AlN (002) peak at $2\theta = 36.023^\circ$ [22]

** In-plane stresses are measured without applying RF bias voltage on the substrate

Table I summarizes the characterization results for all samples. The table represents two sets of experiments. The top part shows the characterized samples produced as a function of the substrate temperature. The bottom part shows the characterized samples as a function of the sputtering power. Several trends can be spotted from the top part of the table. The FWHM of the rocking curve values, the surface roughness (in rms) and the residual stress decrease with increasing substrate temperature. On the other hand, the grain size increases with increasing substrate temperature. In the bottom part of table 1, it can be observed that the FWHM rocking curve value, surface roughness and residual stress decrease with an increasing sputtering power. However, no pattern can be observed in the case of grain size.

Figure 1(a) shows the normal scan XRD of the samples that were deposited 250 °C to 450 °C substrate temperature. The major diffraction peak is observed at 36.2 ° and 69.2 ° depicting AlN (002) and Si (400) crystal orientation, respectively. The other minor diffraction peaks can be seen at 41.5 ° depicting SiC (200) orientation. The FWHM of the diffraction peak depicting to (002) orientation is extracted using a Gaussian fitting because of better curve fitting for all the curves compared to Lorentz fitting [23, 24]. The results reveal that the FWHM of the diffraction peak decreases from 0.18° to 0.13° with an increase in substrate temperature from 250 °C to 350 °C. The FWHM value further decreases to 0.11 ° with an increase of substrate temperature to 450 °C. Figure 1(b) shows the FWHM of the rocking curve indicating a (002) orientation. The rocking curve value decreases from 3.38° to 2.85° and 2.37 ° with an increase in substrate temperature from 250 °C to 350 °C. Then, the rocking curve values decrease to 2.12° with further increase in substrate temperatures to 450 °C. Both the FWHM of diffraction peaks and rocking curve measurement consistently shows improvement in the crystal quality of the AlN (002) film at increasing substrate temperature. This trend is in agreement with the theoretical explanation [14,15]. It can be attributed to an increase in the kinetic energy available to the adatoms that ultimately increases their mobility, with an increase in substrate temperature and assists them in arranging along the c-axis orientation [14, 15].

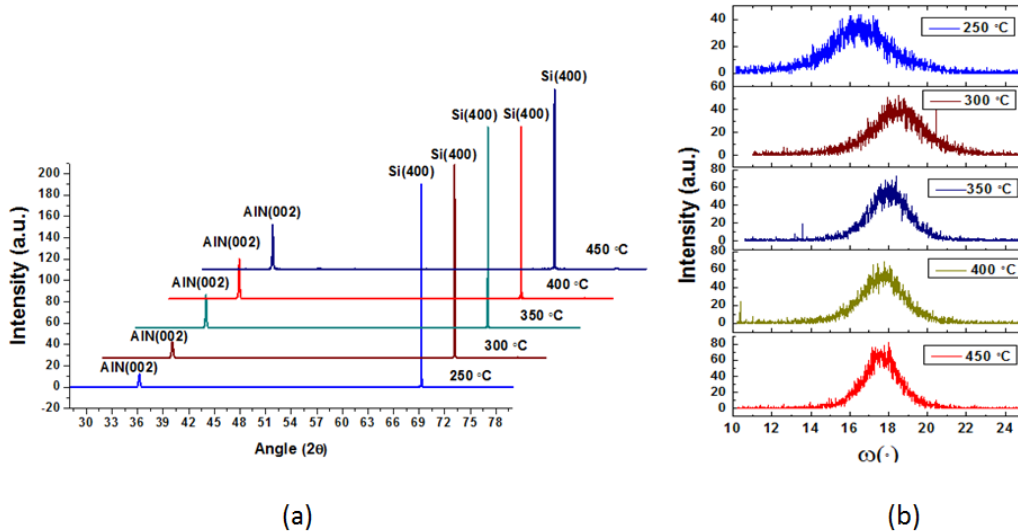


FIG. 1(a) Normal scan XRD of AlN/3C-SiC/Si (100) substrates at different deposition temperatures

FIG. 1(b) Rocking curve measurement of AlN/3C-SiC/Si (100) substrates at different deposition temperatures

The XRD scans of the samples prepared at different sputtering powers from 1200 W to 2400 W are shown in Figure 2(a). The major diffraction peak is observed at 36.2 ° and 69.2 ° depicting AlN (002) and Si (400) crystal orientation, respectively. The value of the FWHM of diffraction peak depicting AlN(002) orientation is given in Table 1. The results show that the FWHM diffraction peak increases from 0.11 ° to 0.15 °, when the sputtering power was increased from 1200 W to 1500 W. This trends follow the results reported in the literature [12] [25]. The FWHM diffraction peak value decreases to 0.13 °, with an increase in sputtering power to 1800 W. The FWHM of the rocking curve depicting to (002) orientation. The values are 2.6° and 2.7° at the sputtering power of 1200 W and 1500 W, respectively. Then, the rocking curve values decrease to 2.37°, 2.51° and 2.22° with an increase in sputtering power at the sputtering power 1800 W, 2100 W and 2500 W. This trend is in agreement with the literature. The crystal quality of the AlN films improve with an increasing sputtering power that can be attributed to increase in adatoms mobility, so that they can move to the lowest energy state and arrange themselves in the c-axis orientation.

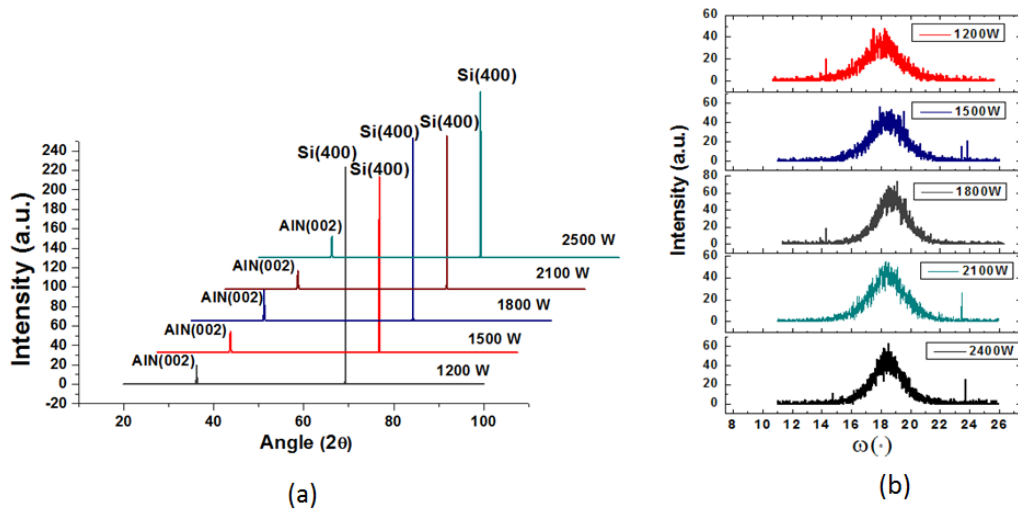


FIG. 2(a) Normal scan XRD of AlN/3C-SiC/Si (100) substrates at different sputtering power

FIG. 2(b) Rocking curve measurement of AlN/3C-SiC/Si (100) substrates at different sputtering temperatures

In order to measure the residual stress, AlN thin films were separately sputtered on top of 50 mm diameter SiC/Si (100) wafer for different substrate temperatures and sputtering powers. A Tencor Flexus 2320 system measures the change in the wafer's curvature before and after the AlN film deposition. This value is then inserted into Stoney's equation to calculate the stress (σ):

$$\sigma = \frac{E}{6(1-\nu)} \frac{t_s^2}{r_c} \left(\frac{1}{r_u} - \frac{1}{r_c} \right) \quad (1)$$

where E , ν , t_s and r_f are the Young's modulus, Poisson's ratio for the silicon substrate, silicon thickness and film thickness, respectively. r_u and r_c are the radii of curvature of the Si substrates before and after AlN deposition, respectively.

According to the literature, the residual stress of the film should increase with increasing substrate temperature due to CTE differences between the AlN film and 3C-SiC/Si substrate [16]. However, Figure 3 reveals that the stress is tensile in nature, and it decreases from 380 MPa to 308 MPa with an increase in substrate temperature from 250 °C to 450 °C. These results can be understood using the mechanism of compressive stress generation at increasing deposition temperature as provided by Chason et al. [26]. They explained that the non-equilibrium nature of the surface during the deposition drives the adatoms into the grain boundary and induces compressive stress [27]. Increasing the substrate temperature ultimately increases the mobility of adatoms, which causes the diffusions of atoms into the grain boundaries and results in a compressive stress in deposited films.

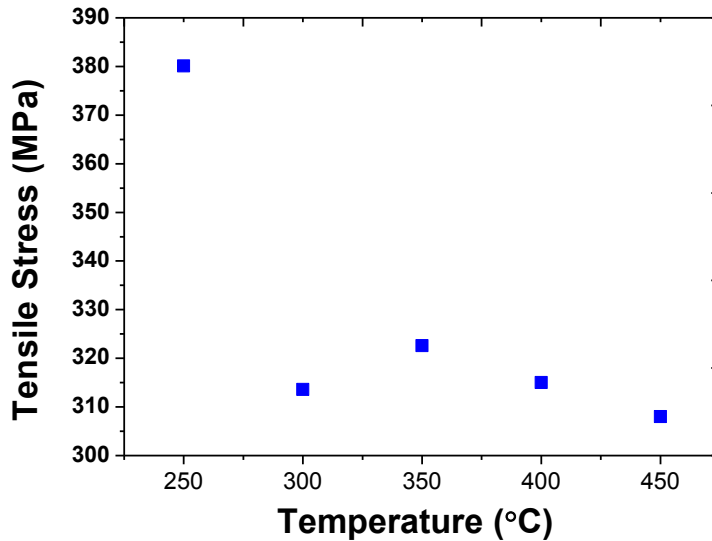


FIG. 3 Plot of tensile stress vs substrate temperature

The plot of residual stress of AlN thin films as a function of deposition power is shown in Figure 4. Interestingly, the stress, which is tensile in nature decreases with an increase in sputtering power. This phenomena can be explained with the help of the kinetic energies of the deposited species and inert gas ions, which are normally significantly greater than the thermal energy [28]. At low sputtering power, the sputtered particles (ejected Al atoms) have low kinetic energy, so the tensile stress is prominent because of the atomic self-shadowing effect and the gas scattering effect [29]. The kinetic energies of the ejected Al particles increase with increase in sputtering power, leading to the dissociation of the loosely packed plane, which causes the effects of re-sputtering, defect formation, and ion entrapments, that is, “collisionally - induced defects” [30]. Also, the momentum transfer from the energetic particle at high sputtering power increases the adatoms' mobility and drives the atoms in the film into more dense configurations or creates stress-inducing defects, which are normally referred as “atomic peening effects”. Hence, a dense and compact film is formed, leading to compressive stress [31].

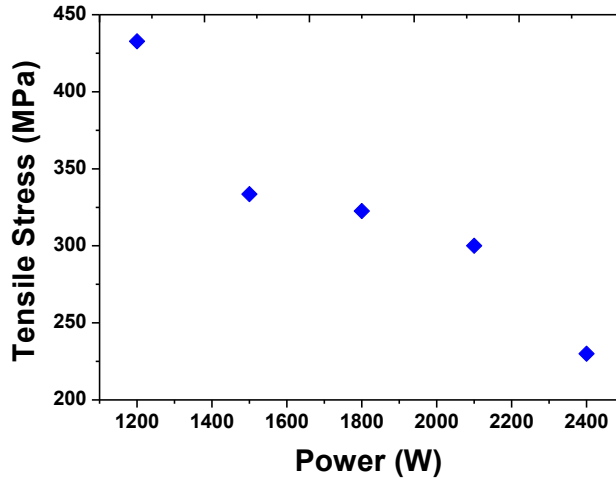


FIG. 4 Plot of in-plane stress vs sputtering power

Figure 5 presents the SEM images that show the surface microstructure of AlN films deposited at various substrate temperatures. It is evident that the grain size increases with an increase in substrate temperature because the small crystallites coalesce to form larger crystallites, increase the grain size [32].

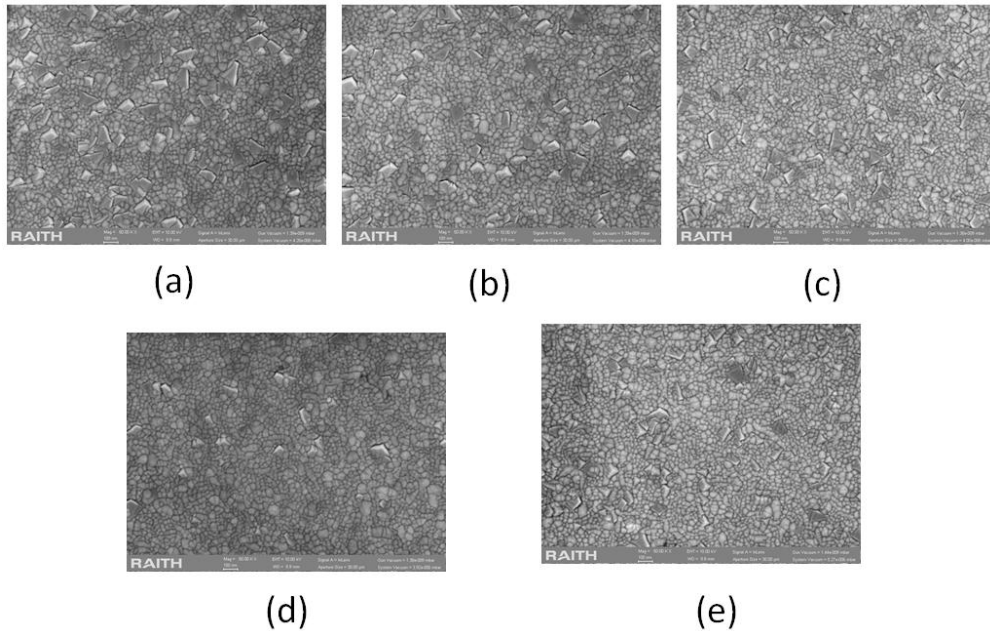


FIG. 5 SEM images of AlN deposited at substrate temperature of (a) 250 °C (b) 300 °C (c) 350 °C (d) 400 °C (e) 450 °C

The surface roughness of the deposited films was measured in a $5 \mu\text{m} \times 5 \mu\text{m}$ area using contact mode Atomic Force Microscopy using a silicon cantilever. Figure 6 shows the scan AFM images for all the samples. The results from Table 1 demonstrate that the roughness (in root mean square) of the AlN layer was 3.40 nm which decrease to 2.67 nm with an increase in substrate temperature from 250 °C to 450 °C, which is attributed to the improved surface adatoms migration caused by increasing the substrate temperature [21].

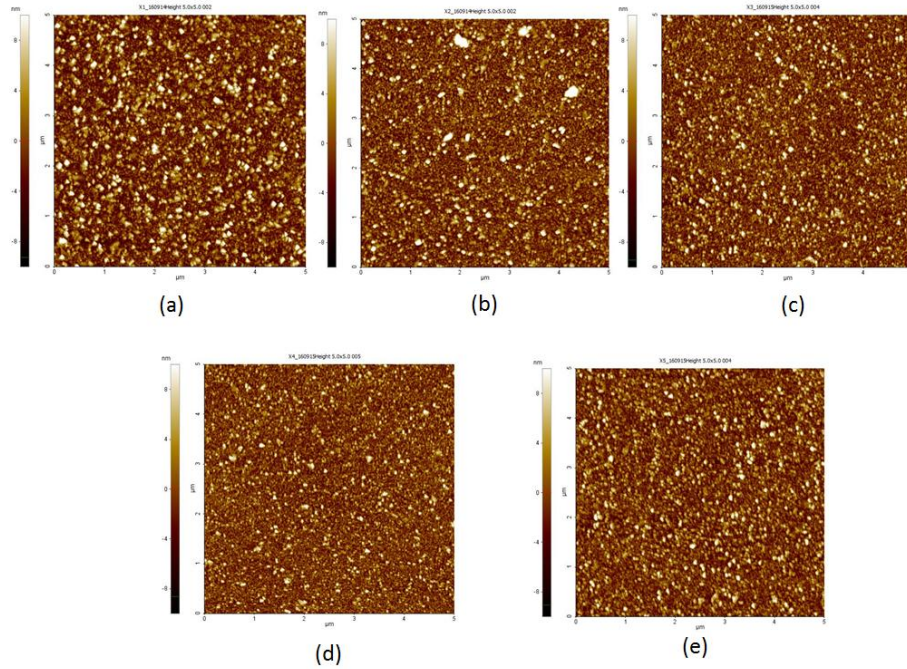


FIG. 6 AFM images of AlN deposited at substrate temperature of (a) 250 °C (b) 300 °C (c) 350 °C (d) 400 °C (e) 450 °C

The sputtering power plays a major role in the deposition rate. It is evident from Table 1 that deposition rate increases proportionally from 10.33 nm/min to 18 nm/min with an increase in sputtering power from 1200 W to 2400 W. The deposition rate increases with an increase in sputtering power because of an increase in Al atoms sputtered from the target [12].

Figure 7 shows the surface microstructure of AlN films deposited at different sputtering powers. It can be observed that the grain size decreases from 79 nm to 58 nm with an increase in sputtering power from 1200W to 1500 W. The grain size increases to 67 nm with further increase in sputtering power to 1800 W. It decreases again to 48 nm and finally increases again to 58 nm with further increase in sputtering power to 2100 W and 2400 W respectively. Further investigation needs to be performed to investigate this seemingly random pattern.

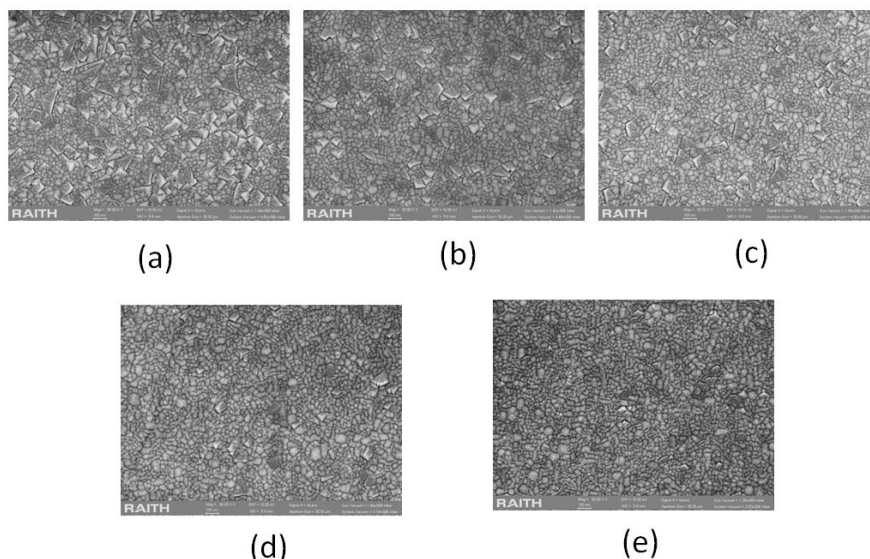


FIG. 7 SEM images of AlN deposited at sputtering power of (a) 1200 W (b) 1500 W (c) 1800 W (d) 2100 W (e) 2400 W

Figure 8 shows the AFM scan of the deposited films with an increase in sputtering power from 1200 W to 2400 W. The results from Table 1 demonstrate that the roughness (in root mean square) of the AlN layer was measured as 3.9 nm which decrease to 2.3 nm with an increase in sputtering power from 1800 W and 2400 W, respectively. This can be attributed to the improved surface mobility of adatoms because of an increase in kinetic energy that is proportional to the sputtering power. These adatoms are able to diffuse from grain boundary to lower-energy positions with the introduction of vacancies and voids at the grain interface that reduces the surface roughness [9].

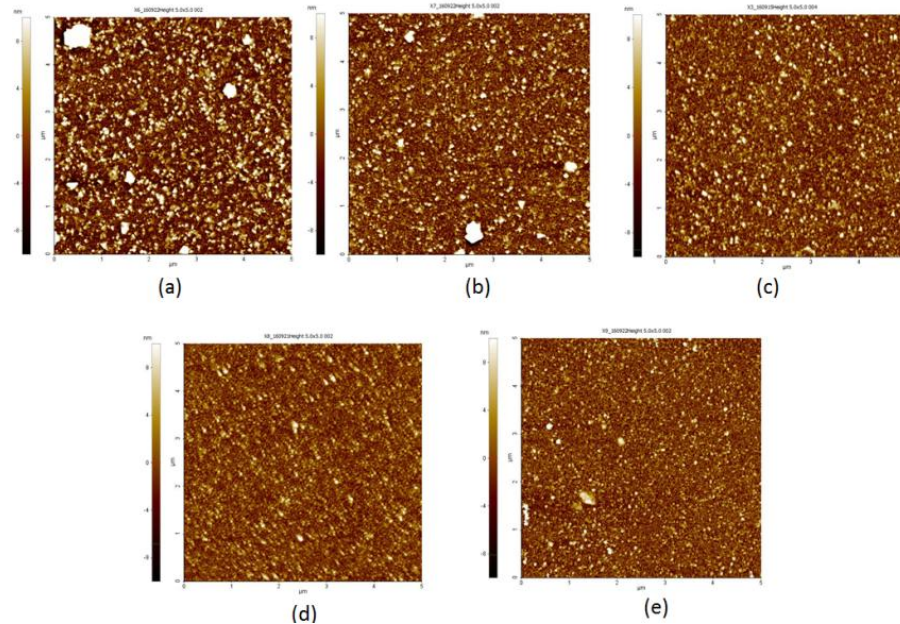


FIG. 8 AFM scan of AlN deposited at sputtering power of (a) 1200 W (b) 1500 W (c) 1800 W (d) 2100 W (e) 2400 W

4. Conclusion

This paper presents the pulsed DC sputtering of c-axis oriented AlN films on 3C-SiC/Si (100) substrates. We investigated the effect of substrate temperature and sputtering power on the crystal orientation, film quality, and in-plane stress. Several generic trends are observed. First, the crystal quality of the AlN (002) film improves with an increase in substrate temperature and sputtering power. Second, the deposition rate increases with sputtering power, and remains constant at increasing temperature. The increasing kinetic energy of the adatoms contributes to both observations. Third, the film surface becomes smoother at increasing temperature and power due to the adatom diffusion from the grain boundary to lower energy positions. Fourth, the values of the in-plane stress decreases at increasing deposition temperature and power due to the build-up of compressive stress, which is in contrast with the literature. Fifth, the AFM and SEM graphs show smoother surfaces at increasing deposition temperature and power. The FWHM values of the rocking curves, the residual stress and the surface roughness of the deposited films reveals that off-axis 3C-SiC/Si(111) substrate provides a better template compared to on-axis 3C-SiC(111) and 3C-SiC(100) substrates for the successful sputtering of c-axis oriented AlN films. This can be attributed to the lower surface roughness and stacking fault density of the 3C-SiC layer, as well as smaller bow magnitude of the off-axis 3C-SiC/Si substrates.

References:

- [1] J. Ruffner, P. Clem, B. Tuttle, D. Dimos, and D. Gonzales, "Effect of substrate composition on the piezoelectric response of reactively sputtered AlN thin films," *Thin Solid Films*, vol. 354, pp. 256-261, 1999.

- [2] A. Claudel, Y. Chowanek, E. Blanquet, D. Chaussende, R. Boichot, A. Crisci, *et al.*, "Aluminum nitride homoepitaxial growth on polar and non-polar AlN PVT substrates by high temperature CVD (HTCVD)," *physica status solidi (c)*, vol. 8, pp. 2019-2021, 2011.
- [3] D. Isarakorn, A. Sambri, P. Janphuang, D. Briand, S. Gariglio, J. Triscone, *et al.*, "Epitaxial piezoelectric MEMS on silicon," *Journal of Micromechanics and Microengineering*, vol. 20, p. 055008, 2010.
- [4] V. Cimalla, J. Pezoldt, and O. Ambacher, "Group III nitride and SiC based MEMS and NEMS: materials properties, technology and applications," *Journal of Physics D: Applied Physics*, vol. 40, p. 6386, 2007.
- [5] C. Zuo, N. Sinha, J. Van der Spiegel, and G. Piazza, "Multifrequency Pierce oscillators based on piezoelectric AlN contour-mode MEMS technology," *Microelectromechanical Systems, Journal of*, vol. 19, pp. 570-580, 2010.
- [6] S. Trolier-McKinstry and P. Muralt, "Thin film piezoelectrics for MEMS," *Journal of Electroceramics*, vol. 12, pp. 7-17, 2004.
- [7] X. Jiang, K. Kim, S. Zhang, J. Johnson, and G. Salazar, "High-temperature piezoelectric sensing," *Sensors*, vol. 14, pp. 144-169, 2013.
- [8] K.-H. Chiu, J.-H. Chen, H.-R. Chen, and R.-S. Huang, "Deposition and characterization of reactive magnetron sputtered aluminum nitride thin films for film bulk acoustic wave resonator," *Thin Solid Films*, vol. 515, pp. 4819-4825, 2007.
- [9] X.-P. Kuang, H.-Y. Zhang, G.-G. Wang, L. Cui, C. Zhu, L. Jin, *et al.*, "Effect of deposition temperature on the microstructure and surface morphology of c-axis oriented AlN films deposited on sapphire substrate by RF reactive magnetron sputtering," *Superlattices and Microstructures*, vol. 52, pp. 931-940, 2012.
- [10] G. Iriarte, J. Rodriguez, and F. Calle, "Synthesis of c-axis oriented AlN thin films on different substrates: A review," *Materials Research Bulletin*, vol. 45, pp. 1039-1045, 2010.
- [11] M. Benetti, D. Cannata, F. Di Pietrantonio, E. Verona, A. Generosi, B. Paci, *et al.*, "Growth and characterization of piezoelectric AlN thin films for diamond-based surface acoustic wave devices," *Thin solid films*, vol. 497, pp. 304-308, 2006.
- [12] K. Kusaka, D. Taniguchi, T. Hanabusa, and K. Tominaga, "Effect of input power on crystal orientation and residual stress in AlN film deposited by dc sputtering," *Vacuum*, vol. 59, pp. 806-813, 2000.
- [13] Z. Vashaei, T. Aikawa, M. Ohtsuka, H. Kobatake, H. Fukuyama, S. Ikeda, *et al.*, "Influence of sputtering parameters on the crystallinity and crystal orientation of AlN layers deposited by RF sputtering using the AlN target," *Journal of Crystal Growth*, vol. 311, pp. 459-462, 2009.
- [14] H. Jin, B. Feng, S. Dong, C. Zhou, J. Zhou, Y. Yang, *et al.*, "Influence of Substrate Temperature on Structural Properties and Deposition Rate of AlN Thin Film Deposited by Reactive Magnetron Sputtering," *Journal of electronic materials*, vol. 41, pp. 1948-1954, 2012.
- [15] W.-J. Liu, S.-J. Wu, C.-M. Chen, Y.-C. Lai, and C.-H. Chuang, "Microstructural evolution and formation of highly c-axis-oriented aluminum nitride films by reactively magnetron sputtering deposition," *Journal of crystal growth*, vol. 276, pp. 525-533, 2005.
- [16] G. F. Iriarte, F. Engelmark, M. Ottosson, and I. Katardjiev, "Influence of deposition parameters on the stress of magnetron sputter-deposited AlN thin films on Si (100) substrates," *Journal of materials research*, vol. 18, pp. 423-432, 2003.
- [17] H. Zhong, Z. Xiao, X. Jiao, J. Yang, H. Wang, R. Zhang, *et al.*, "Residual stress of AlN films RF sputter deposited on Si (111) substrate," *Journal of Materials Science: Materials in Electronics*, vol. 23, pp. 2216-2220, 2012.
- [18] C.-M. Lin, W.-C. Lien, V. V. Felmetser, M. A. Hopcroft, D. G. Senesky, and A. P. Pisano, "AlN thin films grown on epitaxial 3C-SiC (100) for piezoelectric resonant devices," *Applied Physics Letters*, vol. 97, pp. 141907-141907-3, 2010.

- [19] A. Iqbal, K. Chaik, G. Walker, A. Iacopi, F. Mohd-Yasin, and S. Dimitrijev, "RF sputtering of polycrystalline (100),(002), and (101) oriented AlN on an epitaxial 3C-SiC (100) on Si (100) substrate," *Journal of Vacuum Science & Technology B*, vol. 32, p. 06F401, 2014.
- [20] A. Iqbal, G. Walker, A. Iacopi, and F. Mohd-Yasin, "Controlled sputtering of AlN (002) and (101) crystal orientations on epitaxial 3C-SiC-on-Si (100) substrate," *Journal of Crystal Growth*, vol. 440, pp. 76-80, 2016.
- [21] L. Wang, S. Dimitrijev, J. Han, A. Iacopi, L. Hold, P. Tanner, *et al.*, "Growth of 3C-SiC on 150-mm Si (100) substrates by alternating supply epitaxy at 1000 C," *Thin Solid Films*, vol. 519, pp. 6443-6446, 2011.
- [22] S. Khan, M. Shahid, A. Mahmood, A. Shah, I. Ahmed, M. Mehmood, *et al.*, "Texture of the nano-crystalline AlN thin films and the growth conditions in DC magnetron sputtering," *Progress in Natural Science: Materials International*, vol. 25, pp. 282-290, 2015.
- [23] J. Komiyama, K. Eriguchi, Y. Abe, S. Suzuki, H. Nakanishi, T. Yamane, *et al.*, "Polarities of AlN films and underlying 3C-SiC intermediate layers grown on (111) Si substrates," *Journal of Crystal Growth*, vol. 310, pp. 96-100, 2008.
- [24] M. Assouar, O. Elmazria, L. Le Brizoual, and P. Alnot, "Reactive DC magnetron sputtering of aluminum nitride films for surface acoustic wave devices," *Diamond and related materials*, vol. 11, pp. 413-417, 2002.
- [25] H. Cheng, Y. Sun, J. Zhang, Y. Zhang, S. Yuan, and P. Hing, "AlN films deposited under various nitrogen concentrations by RF reactive sputtering," *Journal of crystal growth*, vol. 254, pp. 46-54, 2003.
- [26] D. Flötotto, Z. Wang, L. Jeurgens, E. Bischoff, and E. Mittemeijer, "Effect of adatom surface diffusivity on microstructure and intrinsic stress evolutions during Ag film growth," *Journal of Applied Physics*, vol. 112, p. 043503, 2012.
- [27] E. Chason, "A kinetic analysis of residual stress evolution in polycrystalline thin films," *Thin Solid Films*, vol. 526, pp. 1-14, 2012.
- [28] E. Chason and P. R. Guduru, "Tutorial: Understanding residual stress in polycrystalline thin films through real-time measurements and physical models," *Journal of Applied Physics*, vol. 119, p. 191101, 2016.
- [29] G. Huffman, D. Fahndline, R. Messier, and L. Pilione, "Stress dependence of reactively sputtered aluminum nitride thin films on sputtering parameters," *Journal of Vacuum Science & Technology A*, vol. 7, pp. 2252-2255, 1989.
- [30] H.-C. Lee and J.-Y. Lee, "Effect of negative bias voltage on the microstructures of AlN thin films fabricated by reactive rf magnetron sputtering," *Journal of Materials Science: Materials in Electronics*, vol. 8, pp. 385-390, 1997.
- [31] H. Liu, G. Tang, F. Zeng, and F. Pan, "Influence of sputtering parameters on structures and residual stress of AlN films deposited by DC reactive magnetron sputtering at room temperature," *Journal of Crystal Growth*, vol. 363, pp. 80-85, 2013.
- [32] Z. Fang, Z. Yan, Y. Tan, X. Liu, and Y. Wang, "Influence of post-annealing treatment on the structure properties of ZnO films," *Applied Surface Science*, vol. 241, pp. 303-308, 2005.

Chapter 8: Applications Of AlN/3C-SiC/Si Composite Layers For Piezoelectric Applications

This chapter consists of three conference papers:

- Iqbal, A., Mohd-Yasin, F., & Dimitrijev, S. (2014, October). The design and optimization of two low frequency energy harvesters employing 3C-SiC/AlN/Mo composite layers. In *3RD INTERNATIONAL CONFERENCE ON FUNDAMENTAL AND APPLIED SCIENCES (ICFAS 2014): Innovative Research in Applied Sciences for a Sustainable Future* (Vol. 1621, No. 1, pp. 290-296). AIP Publishing
- Iqbal, A., Mohd-Yasin, F., & Dimitrijev, S. (2014, August). Design optimization and finite element analysis of AlN/3C-SiC piezoelectric bio-sensors. In *Semiconductor Electronics (ICSE), 2014 IEEE International Conference on* (pp. 509-512). IEEE.
- Iqbal, A., & Mohd-Yasin, F. (2015, August). Comparison of seven cantilever designs for piezoelectric energy harvester based On Mo/AlN/3C-SiC. In *Micro and Nanoelectronics (RSM), 2015 IEEE Regional Symposium on* (pp. 1-4). IEEE.

The Finite element analysis results such as the output voltage, von misses stress and the resonance frequency etc depends on the material properties of each structural layer. In this chapter, the values assigned to each layer is taken from the literature review reported by numerous research groups. The output voltage directly depends on the piezoelectric coefficients i.e. d_{33} and d_{31} . In all the simulations throughout this chapter, the value of 5.1 pm/V and 2.56 pm/V are used for the d_{33} and d_{31} respectively.

8.1. The Design and Optimization of Two Low Frequency Energy Harvesters Employing 3C-SiC/AlN/Mo Composite Layers

Abid Iqbal^{1a}, Faisal Mohd-Yasin¹, and Sima Dimitrijev¹

¹*Queensland Micro- and Nanotechnology Centre, Griffith University, Brisbane, QLD 4111, AUSTRALIA*

^{a)}Corresponding author: abid.iqbal@griffithuni.edu.au

Abstract. This paper presents the design and simulation of two cantilever-based energy harvesters that employ cubic silicon carbide on the silicon (3C-SiC-on-Si) wafer as the base material and the bottom electrode. Aluminum Nitride (AlN) is employed as the piezoelectric/middle layer due to its excellent material properties and high stability in varying temperature and harsh environments. Molybdenum (Mo) serves as the top layer/electrode. The thickness of the structural layers are optimized through MATLAB and also analyzed via Finite Element Analysis using Intellisuite. Two designs are proposed at a low resonant frequency, one with a conventional cantilever beam, the other with a T-shaped cantilever beam. Both structures are simulated, and their performances are compared.

Introduction:

The growth of micro-scale wireless electronics such as sensors is increasing significantly because of the miniaturization and low power consumption, easily attainable with MicroElectromechanical Systems (MEMS). These wireless micro-scale electronics consume a minimum amount of electrical energy from batteries or chemical fuel cells. The limited life-span and expensive replacement and re-fuelling procedure of conventional power sources prompt to find alternative power sources from ambient energy in the environment. Numerous ambient energy sources are available for harvesting such as solar, thermoelectric, acoustic and mechanical vibrations. Among them, the mechanical vibration energy source has the maximum capacity to power low power wireless electronic devices [1].

Mechanical vibration has three transduction mechanisms i.e. piezoelectric, electrostatic and electromagnetic [2]. Electrostatic generator output impedance is very high and results in a current limited supply. Parasitic capacitances present within the structure also deteriorate the generator efficiency. Electromagnetic generators are readily available in macro-scale systems. Building electromagnetic generators on the microscale will have some difficulties. These include poor planar magnetic properties, a small number of coil turns, low vibration amplitude and difficulty of integration into Microsystems. Piezoelectric has the most capability to generate maximum power for a given size. [3].

Silicon (Si) based cantilever piezoelectric energy harvesters have been investigated by many groups. One such group fabricated a Si-based cantilever piezoelectric energy harvester.

They utilized lead zirconate titanate (PZT) as the piezoelectric material while platinum/titanium (Pt/Ti) and nickel were used as the electrodes and proof mass, respectively. The device was capable of generating $2.16\mu\text{W}$ power [4]. Another group employed an array of cantilevers as a piezoelectric energy harvester and produced $3.98\mu\text{W}$ power [5]. Two other groups also generated $2.15\mu\text{W}$ [6] and $0.32\mu\text{W}$ [7] using a Si substrate with Si as a proof mass. However, to the best of the author's knowledge, none of the research works addressed the issue of extreme environment conditions, for example, higher loads and temperatures. Devices on the microscale based on Si technology cannot operate in extreme environments. Conventional Si technology cannot function beyond 500°C [8]. Silicon material properties are insufficient to operate in harsh environments (i.e. to operate at high temperature of 500°C). This is overcome by exploiting SiC material because of its excellent mechanical and chemical properties such as extreme hardness, low-friction reducing mechanical wear-out and chemical inertness to corrosive atmospheres [9].

Patterning of single crystal 4H- and 6H-SiC with wet chemicals becomes difficult in micromachining processing. Hetero-epitaxial 3C-SiC and poly-crystalline SiC are more suitable for micromachining. Different processing techniques such as bulk micromachining, surface micromachining and micro-molding are used to fabricate micromechanical structures including resonators and micromotors. SiC-based electric micromotors and micro jet-engine power generation sources enable longer duration were examined and showed SiC's excellent durability where mechanical properties of Si are insufficient [10]. Active monitoring and control of combustion engines are used to improve the fuel efficiency and pollution reduction, and can be done by SiC-based harsh environment sensors. SiC's high-temperature potential led to the development of catalytic metal-SiC and metal insulator-SiC prototype gas sensors for monitoring gas emission and fuel leakage detection [11]. Consumers such as automobile and aircraft industries are looking for harsh environment type devices, and thus more research is required to commercialize SiC MEMS.

The aim of this research is to design an energy harvester for harsh environments using a cantilever structure that is capable of withstanding a high temperature using cantilever structure [12]. Silicon carbide is chosen as a structural layer while Aluminum Nitride is selected as the piezoelectric material. The high melting point, high curie temperature (1100°C) and chemical stability of AlN makes it more preferable than ZnO as the chosen piezoelectric material.

In this paper, we presented the design and optimization of an energy harvester based on the conventional cantilever beam and proposed a T- shaped cantilever beam energy harvester at room temperature. The simulation results show that higher potential is generated in the T-shaped cantilever beams as compared to the conventional cantilever beams. Also, the thickness of the structural layer and piezoelectric layers i.e. SiC and AlN are optimized via Finite element methods using Intellisuite. It is found that 0.6 micron thickness of AlN results in high open circuit voltage. The range of output power highly depends on the size of energy harvesters dimensions, the load resistance, resonance frequency and acceleration amplitude etc. In this paper, we didn't simulated the output power generations of the proposed designs because of Intellisuite software limitations. We planned to fabricate and optimize the sensing electronic circuitry for the proposed designs in the future. The simulation of both designs on high temperature was planned. However, the simulation was not completed because of limited modules for piezoelectric simulation related to temperature in Intellisuite software. The resonance frequency of the proposed piezoelectric energy harvester would decreases with an increase in operational temperature because of spring softening effect. However, the piezoelectricity of AlN films is supposed to not be affected by the change in operational temperature because of high curie temperature of AlN i.e. 1100°C .

Fundamental frequency of cantilever

The fundamental frequency of the cantilever beam depends on material properties (Young's modulus and density of the material) and dimensions (length and thickness of the beam). The fundamental frequency is given by eq. 1 [12]:

$$f = \frac{1}{2\pi} \frac{h}{L^2} \sqrt{\frac{E}{\rho}} \quad (1)$$

where "E" Young's modulus, "ρ" is the density of the material, "h" and "L" are the thickness and length of the cantilever beam, respectively.

Mathematical Modelling

The unimorph piezoelectric cantilever beam is shown in Fig.1. It consists of three layers, i.e., a piezoelectric layer, substrate/bottom and the top electrode. The cantilever beam is fixed to at one end, at $x=0$ and free at the other end, at $x=L$. The length and width of the cantilever beam are L and w , respectively. All the three layers are identical in length. The thickness of the substrate/bottom electrode, the piezoelectric, and the top electrode layers are denoted as t_s , t_p and t_e , respectively.

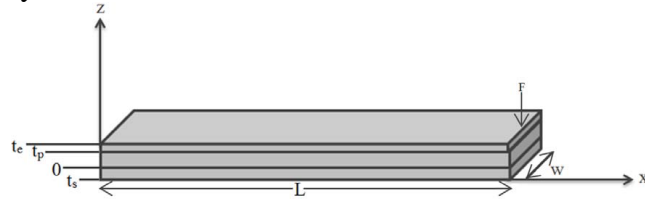


FIGURE 1. Unimorph piezoelectric cantilever beams in cartesian system

The Young's modulus of the substrate/bottom electrode, the piezoelectric and the top electrode are represented as E_e , E_p , and E_t , respectively. The direction of the length is poled along the x-axis, and the thickness is poled along the z-axis. The neutral plane of the cantilever is denoted as t_n . A constant force, F is applied on the cantilever tip or the free end of the cantilever in d_{31} vibrational mode. The generated output voltage is dependent on the cantilever beam dimensions, the material properties and also the applied force. The generated voltage is given by eq. 2.

$$\frac{V_{avg}}{F} = \frac{L}{2} g_{31} \frac{E_p}{wD} \left(\frac{t_p^2}{2} - t_n t_p \right) \quad (2)$$

where g_{31} is piezoelectric coefficient related to the piezoelectric strain coefficient, E_p is Young's modulus of the piezoelectric, "w" is the width of the cantilever and t_p , t_n are the thickness of the layers, respectively. D is the bending modulus per unit width and is given as eq. 3:

$$D = \frac{1}{3} (E_s t_s^3 + E_p t_p^3 + E_e (t_e^3 - t_p^3)) + t_n (E_s t_s^3 - E_p t_p^2 - E_e (t_e^2 - t_p^2)) + t_n^2 (E_s t_s + E_p t_p + E_e (t_e - t_p)) \quad (3)$$

The maximum displacement at the free end can be found as eq. 4. The maximum displacement is proportional to the applied force and the length of the cantilever beams, while inversely proportional to the width and bending modulus respectively.

$$h_{\max} = \frac{FL^3}{3wD} \quad (4)$$

Design Optimization Using Matlab

Cantilever dimensions should be selected to match with the targeted vibration source's frequency, and the device must be in micro-scale range.

Thickness of piezoelectric layers

The natural frequency of the structure depends on dimensions and material properties such as elasticity and density as shown in eq. 1 and eq. 2. The dimension of the device can be varied to optimize the resonance frequency of the device. The optimized dimensions of the cantilever are shown in Table 1 for the desired resonance frequency. The thickness of piezoelectric material plays a vital role in the magnitude of output power. Piezoelectric thickness optimization can be done with the help of eq. 3. A parametric sweep is performed on piezoelectric thickness vs. output voltage using Matlab. The maximum voltage generated by piezoelectric material with an optimized thickness of 600nm is 49.58mV as shown in Fig 2.

Proof mass

Optimization of the proof mass dimensions can support scaling down of the natural frequency of the cantilever to match source input frequency. The width of the proof mass is kept constant to make the uniform device, even though mass proof width has an effect on natural cantilever frequency. The length and the thickness of the proof mass are critical parameters for optimization purposes. As the proof mass thickness increases, there is a gradual decrease in cantilever's natural frequency and also this induces more strains in the cantilever. Optimization of proof mass length was examined between length ratios (L_{pm}/L) and cantilever natural frequency, where L_{pm} is proof mass length and L is cantilever beam length. A parametric sweep was carried on mass proof length and its effects on natural frequency of cantilever as shown in Fig. 3. As the proof mass length increases, then the natural frequency of the cantilever decreases gradually down to the lengths ratio equal to 0.3 and after this point the natural frequency starts increasing due to increasing in cantilever stiffness. After a length ratio of 0.3 is reached the cantilever beam starts becoming stiffer; this means that the elastic modulus of the cantilever beam increases with proof mass length.

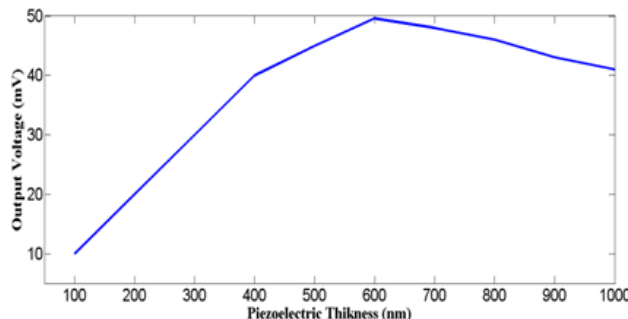


FIGURE 2. Calculated output voltage versus piezoelectric thickness

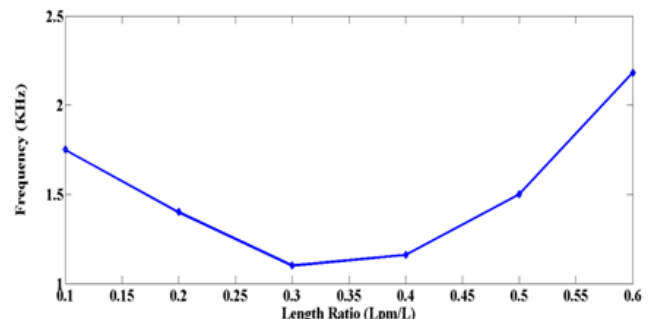


FIGURE 3. Length ratio between proof mass and cantilever beam effects on frequency

Even though natural frequency increases, the longer proof mass will help in producing more strain in the cantilever beam. Large strains are more helpful in piezoelectric energyharvesting device to generate more power. The selection of proof mass length has been chosen based on a lower fundamental frequency which is useful to match with low vibration source frequencies and to generate more power at resonance.

Finite Element Analysis

The finite element analysis is carried out using Intellisuite Software. Two kinds of analysis are carried out. The first one is a structural analysis to verify the resonance frequency, while the second one is a piezoelectric analysis to determine the generated output voltage.

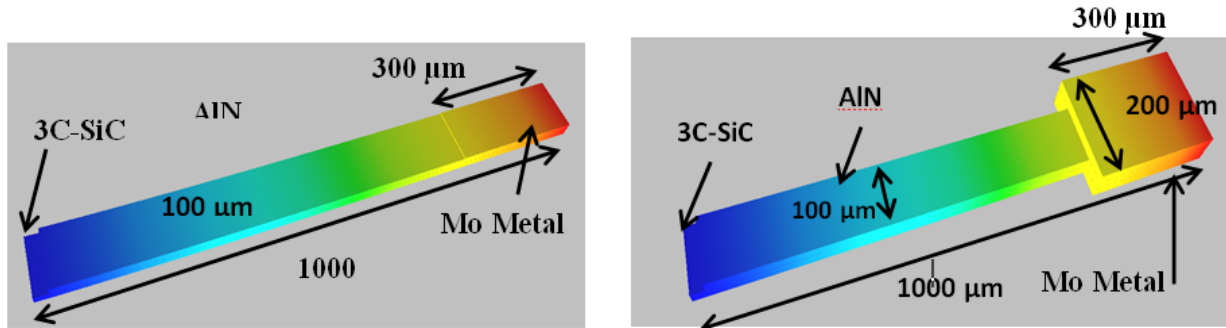


FIGURE 4. Simulated conventional and proposed T- shaped piezoelectric energy harvester in 3D (a) Conventional Cantilever Beam (b) T-shaped Cantilever Beam

Geometry

Two different materials are employed for the cantilever piezoelectric energy harvester as the substrate/bottom electrode, namely 3C-SiC and Si. The piezoelectric thin film is used as the active material and has major advantages such as the generation of significant motion, low hysteresis, and high sensitivity with wide dynamic ranges. Three major piezoelectric thin films are lead zirconate titanate(PZT), zinc oxide (ZnO) and aluminum nitride (AlN). Aluminum Nitride is chosen for this design due to its high melting point and chemical stability. The material selected for the top electrode and the proof mass is molybdenum (Mo),

which has a high density and the ability to provide displacement. The body load condition is applied in each layer of the cantilever beam with an acceleration of 2.25 m/s^2 in d_{31} mode.

The 3D cantilever structure is shown in Fig.4 consists of three layers and the proof mass that is placed at the free end. The length and the width of the cantilever are $1000\mu\text{m}$ and $100\mu\text{m}$, respectively, whereas the thicknesses is varied for each layer including the proof mass that is poled along the z-axis. Both the conventional and proposed T-shaped cantilever beam are shown in the figure. The proof mass width for the T-shaped is 200 microns while its length is set as 300 microns. The substrate/bottom electrode is 600nm thick; the piezoelectric layer is also 600nm thick, while the top electrode is 200nm thick layers. The optimized dimensions of both proposed models are given in Table 1.

Boundary Settings

The boundary settings are concerned with the constraint conditions, the surface load, and the electric boundary condition. Two types of boundary conditions are applied for modal analysis and piezoelectric analysis. A fixed constraint is applied at one end, and modal analysis is carried out after applying the material properties. While in the piezoelectric analysis, one end of the cantilever beam was fixed while the load is applied at the other end along the z-direction. The floating potential and ground are assigned to the top and the bottom surfaces of the piezoelectric material. The remaining surfaces of the piezoelectric layer are assigned as zero charges.

TABLE 1. Optimized dimensions of proposed cantilever piezoelectric energy harvester

Parameters	Dimensions Values	Dimensions Values
	(Conventional Cantilever Beam)	(T-shaped Cantilever Beam)
Cantilever Length (μm)	1000	1000
Cantilever Width(μm)	100	100
Substrate Thickness (nm)	600	600
Piezoelectric Thickness (nm)	600	600
Top Electrode (nm)	100	100
Proof Mass Length (μm)	300	300
Proof Mass Width (μm)	100	200
Proof Mass Thickness (μm)	0.6	0.6

Mesh Settings

In the mesh settings, the free mesh parameters option is chosen to mesh the 3D cantilever beam. The auto mesh was chosen for all the simulation. The total number of mesh elements

used for the cantilever beam and proposed T-shaped cantilever beams are 11059 and 15000, respectively.

Results and Discussion

The thickness of the aluminum nitride was optimized for maximum output voltage using the Intellisuite as shown in Fig. 5. The 3C-SiC thickness is set at 1 micron, while the Mo thickness is also kept constant at 0.5 micron and the AlN thickness is varied from 0.1 to 1 micron. It can be observed that maximum voltage is generated for a 0.6 micron thickness which is in close agreement with Matlab results as shown in Fig. 2. The effect of proof mass thickness on the resonance frequency is shown in Fig. 6. It can be seen that the thickness of proof mass can be utilized to tune the resonance frequency. As shown in eq. 1, the resonance frequency of the cantilever beams is inversely proportional to the proof mass.

The comparison between the open circuit voltage of a conventional cantilever beam and the proposed T-shaped cantilever beam is shown in Fig. 7. The simulation results also reveals that the T-shaped design generates twice the voltage as compared to conventional cantilever beams.

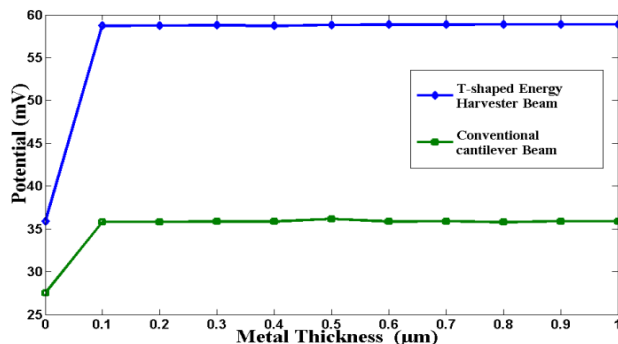


FIGURE 5. Simulated result of open circuit voltage versus metal thickness of proof mass

The 2D plot of the open-circuit voltage of both the conventional and the proposed design is shown in Fig. 5. The open-circuit voltage for the conventional cantilever is found to be 35 mV, while for T-shaped design is found to be 59 mV with the same boundary conditions and the proposed design applied on both of them.

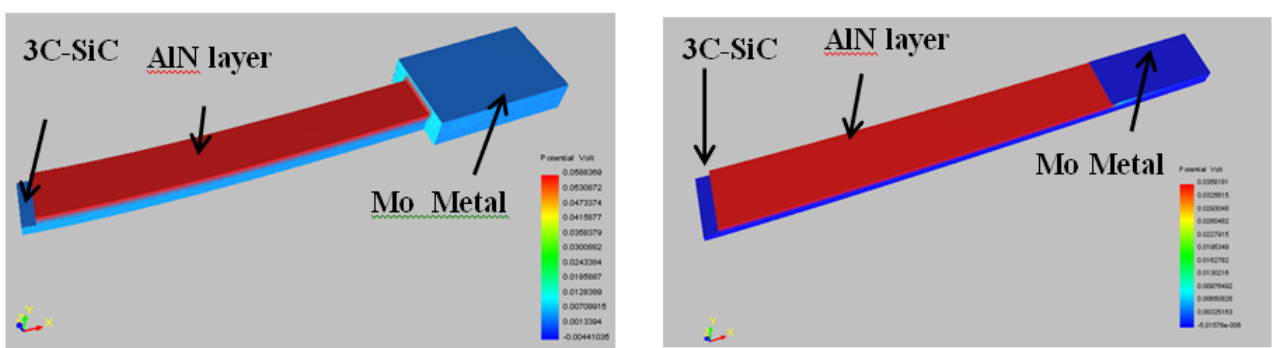


FIGURE 6. 3D Plot of open circuit voltage of conventional and T-shaped cantilever beams
a) T-shaped cantilever beam (b) Conventional cantilever beam

It can be observed from eq. 2; that the open circuit voltage is proportional to the applied force. From Newton's second law of motion, we know that force is directly proportional to the mass and applied acceleration. From Fig. 2, it can be seen that the proof mass in the T-shaped cantilever beam is double the proof mass of the conventional cantilever beams, which results a force of magnitude twice that found in conventional cantilever beams. Also, the strain produced in the T-shaped cantilever beam is doubled and generates, which generate approximately twice the magnitude of voltage via the piezoelectric phenomena compared to the conventional cantilever beam.

Conclusion

This paper has described the design optimization of two cantilever structures based on 3C-SiC for energy harvesting at room temperature. The optimization of the piezoelectric layer and proof mass is carried out using Matlab. The thickness of the AlN is optimized, and it was observed that maximum voltage is generated with the thickness of 0.6 μm . The device is designed to resonate at the desired resonant frequency of 1-2kHz in d_{31} mode. The simulation result shows that the generated output voltage per unit force for the T-shaped cantilever beam is approximately two times that found for the conventional cantilever beam. The close agreement between the analytical analyses and Finite element results are observed for both structures. The next paper will report on the performances of both structures at high temperatures.

Acknowledgements

This work is supported by Queensland Micro- and Nanotechnology Centre (QMNC) and Griffith School of Engineering. This work was performed in part at the Queensland node of the Australian National Fabrication Facility, a company established under the National Collaborative Research Infrastructure Strategy to provide nano and microfabrication facilities for Australia's researchers.

References

1. Dutoit, N. E., Wardle, B. L., and Kim, S. G. "Design considerations for MEMS-scale piezoelectric mechanical vibration energy harvesters." *Integrated Ferroelectrics* **71**, 121-160,(2005).
2. Beeby, S. P., M. J. Tudor, and N. M. White. "Energy harvesting vibration sources for microsystems applications." *Measurement science and technology* **17**, R175,(2006).
3. Roundy, S., and Wright, P. K. "A piezoelectric vibration based generator for wireless electronics." *Smart Materials and structures* **13**, 1131, (2004).
4. Fang, H. B., Liu, J. Q., Xu, Z. Y., Dong, L., Wang, L., Chen, D., and Liu, Y. "Fabrication and performance of MEMS-based piezoelectric power generator for vibration energy harvesting." *Microelectronics Journal* **37**, 1280-1284, (2006).
5. Liu, J. Q., Fang, H. B., Xu, Z. Y., Mao, X. H., Shen, X. C., Chen, D., and Cai, B. C. "An MEMS-based piezoelectric power generator array for vibration energy harvesting." *Microelectronics Journal* **39**, 802-806, (2008).
6. Shen, D., Park, J. H., Ajitsaria, J., Choe, S. Y., Wikle III, H. C., and Kim, D. J. "The design, fabrication and evaluation of a MEMS PZT cantilever with an integrated Si proof mass for vibration energy harvesting." *Journal of Micromechanics and Microengineering* **18**, 055017, (2008).
7. Fang, H. B., Liu, J. Q., Xu, Z. Y., Dong, L., Chen, D., Cai, B. C., and Liu, Y. "An MEMS-based piezoelectric power generator for low frequency vibration energy harvesting." *Chinese Physics Letters* **23**, 732-734, (2006).

8. Lee, T. H., Bhunia, S., and Mehregany, M. "Electromechanical computing at 500 C with silicon carbide." *Science* **329**, 1316-1318, (2010).
9. Epstein, A. H. "Millimeter-scale, Micro-ElectroMechanical Systems gas turbine engines." *ASMEJournal of Engineering for Gas Turbines and Power* **126**(2), 204-226, (2006).
10. Hunter, G. W., Neudeck, P. G., Xu, J., Lukco, D., Trunek, A., Artale, M., and Liu, C. C. "Development of SiC-based gas sensors for aerospace applications." In *MRS Proceedings* Cambridge University Press **815**, J4-4, (2004).
11. Sarro, Pasqualina M. "Silicon carbide as a new MEMS technology." *Sensors and Actuators A: Physical* **82**, 210-218,(2008).
12. Kudimi, J. M. R., Mohd-Yasin, F., and Dimitrijev, S. "SiC-based Piezoelectric Energy Harvester for Extreme Environment." *Procedia Engineering* **47**, 1165-1172, (2012).

8.2. Design Optimization and Finite Element Analysis of AlN/3C-SiC Piezoelectric Bio-Sensors

Abid IQBAL*, Faisal MOHD-YASIN and Sima DIMITRIJEV

Queensland Micro- and Nanotechnology Centre,

Griffith University, Brisbane,

QLD 4111, Australia

Abstract— In this paper we present the design and simulation of a bio-sensor for pathogens detection based on an AlN/3C-SiC/Si piezoelectric cantilever. Cubic silicon carbide (3C-SiC) is chosen as the base layer due to its excellent material properties and chemical inertness over silicon in harsh environmental conditions. Aluminum nitride (AlN) is selected as the piezoelectric active layer due to its similar thermal expansion coefficient as silicon carbide to reduce thermal stress. The desired resonant frequency of 157.16 KHz is optimized using Matlab, and the finite element analysis is carried out using COMSOL software to verify the shift in the resonant frequency due to the added mass of the bacteria. The surface functionalization of the SiC as a biosensor, as well as the fabrication recipes, are also proposed.

Keywords—Microresonator, Piezoelectric, 3C-SiC, Si, Pathogens, Extreme environment.

Introduction

Quartz crystal resonators are being widely used in timing references due to their high precision and thermal stability. However, the poor integrability of these crystals with CMOS and their large size encouraged various research groups to develop other types of resonators. MEMS resonators have received the most interest as an alternative to quartz crystals due to their smaller size, compatibility with CMOS ICs and low power consumption [1]. Various transduction methods such as piezoelectric, capacitive, piezoresistive and thermal transduction are explored, each possessing relative merits and trade-offs over the other [2-3]. For example, capacitive microresonators have weak electromechanical response, while thermal microresonators require high voltage and power. Similarly piezoelectric resonators lose out in terms of lower quality factor (Q).

Beside timing references, these microresonators are used for other applications such as energy harvesters and bio sensors. The MEMS-based resonant bio sensors detect the pathogens by measuring the decrease in resonance frequency due to the added mass of the pathogens. This mass-sensing technique is being explored by various research groups. Their smaller sizes and high resonant frequencies provide higher resolution and precision compared to conventional mass sensors [4-10]. Hao et al. employed a length-extensional bulk mode resonator for mass sensing with a mass sensitivity of 215 Hz/pg accompanied with the Quality Factor, Q of 4000 in the air [6]. One group has utilized a square-extensional mode resonator as a mass sensor with a sensitivity of 3.3 Hz/ng and Q exceeding 106 [7].

Heteroepitaxial 3C-SiC and poly-crystalline SiC are typically utilized for micromachining because the patterning and wet etching of single

crystal 4H- and 6H-SiC are much more difficult compared to that of 3C-SiC thin film. The 3C-SiC thin films are used in various applications due to their better mechanical properties over silicon at high temperature and harsh environments. The most common applications are micro jet-engine power generation sources, energy harvesters for harsh environment and electric micromotors [8]. Also, the SiC based harsh sensors are employed for the monitoring of combustion engines, to improve the fuel efficiency and pollution reduction. It is also used as gas sensors for monitoring gas emission and fuel leakage detection [9].

In this work, we proposed a cantilever beam resonator sensor based on AlN/3C-SiC for sensing bio particles e.g. bacteria and viruses, etc. The high Young modulus to Poisson ratio of 3C-SiC results in high resonant frequency and higher Quality Factor as compared to Silicon on insulator (SOI). The resonant frequency of the proposed resonator based on 3C-SiC is 157 KHz [10]. The 3C-SiC is chosen as structural layer due to its resilient mechanical properties to the harsh environment and also the large energy band gap of 2.49eV, which leads to the higher stability of resonance frequency with varying temperature and environmental changes. The finite element analysis is carried out for the design verification and also to measure the frequency shift due to a single bacterium cell. Piezoelectric sensing is used for the biosensors. Aluminum Nitride is chosen as the piezoelectric material. High melting point and chemical stability of AlN have given preference over zinc oxide as the chosen piezoelectric material.

Fundamental Frequency of Cantilever

The resonance frequency of the cantilever beam depends on material properties and its dimensions. The fundamental resonance frequency of the cantilever beam can be given by eq. 1.

$$f = \frac{1}{2\pi} \sqrt{\frac{k}{m}} \quad (1)$$

where "k" is the spring constant of the cantilever beam, which depends on the dimensions of the beam. M is the beam mass which also depends on the dimension and density of the material.

Mathematical Modelling

The unimorph piezoelectric cantilever which is proposed for use as a biosensor is shown in Fig 1. It consists of three layers, i.e.; the first layer is the substrate which is also employed as a bottom electrode; the second layer is the piezoelectric active layer while the third layer is the top electrode. In our case, we proposed 3C-SiC is substrate/bottom electrode, AlN as a piezoelectric layer while Mo is the top electrode. The cantilever beam is attached to the substrate at one end, while the other end is set as free, at $x=L$, where "L" and "w" are the length and width of the cantilever beam. The thickness of the substrate is t_s , while the thickness of the piezoelectric is t_p and the thickness of the top electrode layers is denoted as t_e . The modulus of elasticity for the substrate electrode is E_s , while those of the piezoelectric and the top electrodes are represented as E_p and E_t respectively.

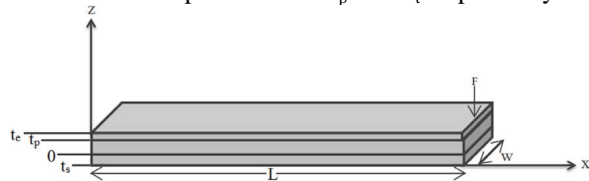


Fig. 1. Unimorph piezoelectric cantilever beams in cartesian system

The output voltage generated from the energy harvester can be given by equation 2, which depends on its dimensions, material properties and also on the applied force.

$$\frac{V_{avg}}{F} = \frac{L}{2} g_{31} \frac{E_p}{wD} \left(\frac{t_p^2}{2} - t_n t_p \right) \quad (2)$$

where " g_{31} " is the piezoelectric coefficient correlated to piezoelectric strain coefficient, the Young's modulus of the piezoelectric is E_p , the

width of the cantilever is "w" and the thickness of the layers is t_p and t_n .

The maximum displacement at free end can be found eq. 3. The maximum displacement is proportional to the applied force and the length of the cantilever beams, while inversely proportional to the width and bending modulus.

$$h_{max} = \frac{FL^3}{3wD} \quad (3)$$

where D is the bending modulus per unit width and is given as eq. 4:

$$D = \frac{1}{3} (E_s t_s^3 + E_p t_p^3 + E_e (t_e^3 - t_p^3)) + t_n (E_s t_s^3 - E_p t_p^2 - E_e (t_e^2 - t_p^2)) + t_n^2 (E_s t_s + E_p t_p + E_e (t_e - t_p)) \quad (4)$$

Working Principle

The working principle of a piezoelectric bio sensor is quite simple. The cantilever beam is coated with a sensing layer, which is capable of recognizing specific target molecule or pathogens, i.e. able to recognize target molecules in key-lock processes. The piezoelectric technique is proposed for the sensing. When the cantilever beam resonates, it induces the charges in the piezoelectric layer due to cantilever movement at the resonance frequency.

The resonant frequency of the cantilever beams is inversely proportional to the mass. This resonance frequency shifts towards a lower value with the increase in mass due to pathogen attachment. The mass of the pathogens can also be measured by calculating the frequency shift towards the right.

Finite Element Analysis

The Finite element Analysis (FEA) is performed to pre-determine and optimize the resonant frequency of the desired Eigen mode utilizing Comsol, which is shown in Fig 2. The fixed constraint was applied to the pad, and the model was meshed using Manhattan bricks with standard physics. The desired first mode is shown in Fig 3. The Eigen frequency is found as 157.16 KHz. The dimension of the proposed cantilever beam resonator is optimized to get the desired resonance frequency of 157 KHz, which can give a high sensitivity of 307 Hz/pg. The thickness of each layer is optimized to 1 micron which gives the desired resonance frequency and maximum open circuit piezoelectric potential. The dimension of the proposed piezoelectric sensor is shown in Fig 3. The design is optimized in terms of the thickness of the layers, length, and width of the structural and piezoelectric layer and proof mass to obtain the desire resonant frequency.

The FE analysis is performed to verify the design and concept. A polystyrene particle of size 1 micron was placed on the microresonators as shown in Fig 2. A frequency analysis was done by applying a boundary load of 1×10^{-5} N/m² on the resonator to see the effect of the particle on the resonance frequency. It can be observed that the resonance frequency decreases by 307 Hz after the particle placement due to increase in the mass according to the equation 1. A frequency sweep was done to find the resonance frequency with and without particle in place. The shift in resonance frequency towards the right due to polystyrene particle can be observed by comparing Fig 4 and Fig 5, and is proportional to the mass of the particle.

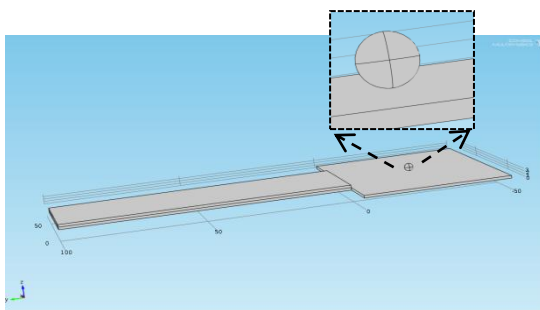


Fig. 2. Schematic of T-shaped cantilever beam resonator with small small particle

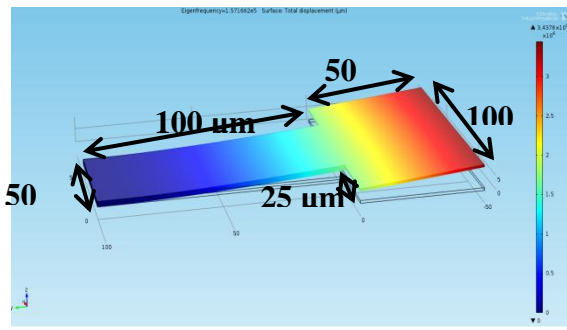


Fig. 3. Optimized dimension of proposed T-shape piezoelectric microresonator

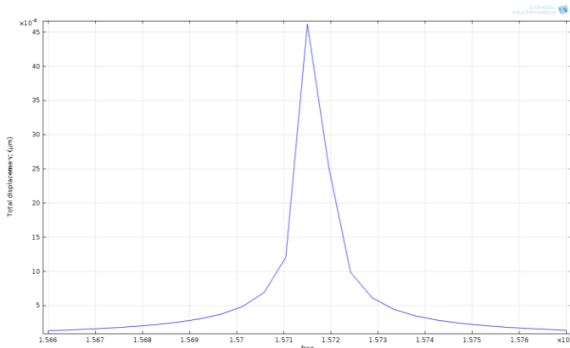


Fig. 4. Frequency sweep of the T-shaper microresonator without the polystyrene

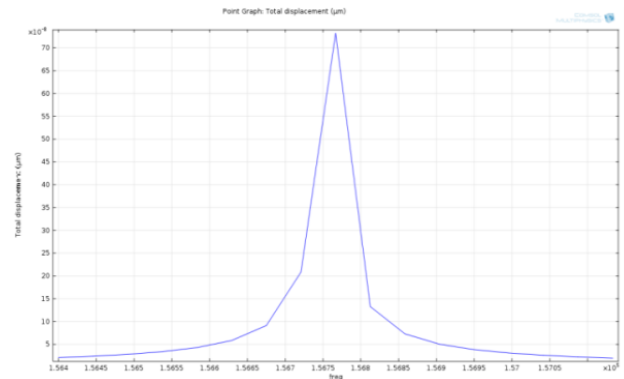


Fig. 5. Frequency sweep of the T-shaper microresonator with the polystyrene

Fabrication Steps and Functionalization:

The main advantage of 3C-SiC over Si as a bio sensor is regarding the immobilization agent. Silicon-based biosensors need an expensive gold layer on top, which is modified for the immobilization of the antibodies. Unlike Si, Silicon carbide can be used for the immobilization of the antibodies on its surface without depositing any gold layers which also reduces the costly and tedious fabrication steps. The immobilization of the antibodies can be easily achieved via amino propyl tri ethoxy silane (APTES) linker via covalent conjugation as shown in Figure 6 [7]. The Surface hydroxylation of the SiC (-OH termination) can be done by treating it with hydrofluoric acid (HF) while the surface functionalization of 3C-SiC with APTES (Sigma- Aldrich) can be achieved by soaking in a 1% APTES/toluene solution for approximately 90 min. The carboxylic group of antibodies can be stimulated through EDC 1-ethyl-3-[3-dimethylaminopropyl] carbodiimide hydrochloride (EDC) and N-hydroxy-succinimide (Sulfo-NHS).

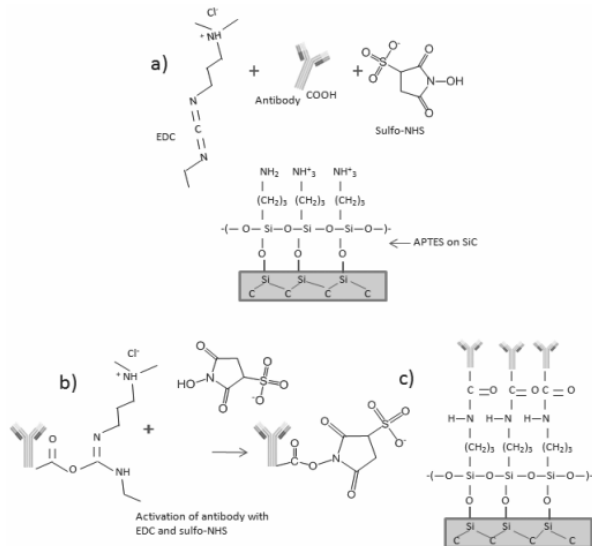


Fig. 6. Process followed for anti-myoglobin immobilization. a) EDC Sulfo NHS solution and anti-myoglobin are deposited on APTES|SiC samples, b) Activation of the antibody carboxylic group with EDC, sulfo- NHS produces a semi-stable amine-reactive ester and c) Antibodies coupled to the surface [7].

The detail fabrication steps of the proposed design are shown in Fig 7.

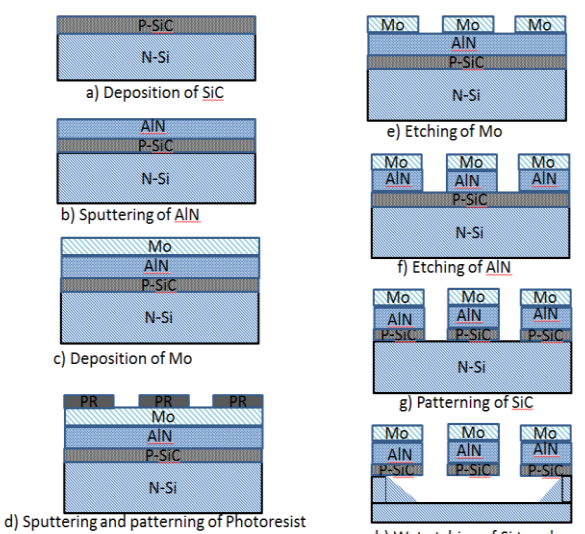


Fig.7. Surface-micromachined 3C-SiC MEMS fabrication process flow. (a) p type doping of Silicon substrate (b) LPCVD 3C-SiC and doping . (c) Sputtering of AlN on SiC. (d) Deposition of Mo (e) Patterning of Photoresist for Pad Metals deposition (f) Etching of Mo (g) Wet etching of Si to release the 3C-SiC/AlN/Mo structure.

Discussion

The finite element analysis and the mathematical modeling of the bio sensor based on a SiC/AlN/Mo cantilever beam are presented. The proposed bio sensor utilizes the electrical actuation while employing piezoelectric sensing. The SiC is utilized as the structural as well as the lower electrode while AlN is used as the active

piezoelectric material. The similar thermal expansion coefficient of all the layers reduces the residual and thermal stress, and the high curie temperature of AlN enables the operation of the designed resonator in harsh environments. From equation 1, when the proof mass increases due to the pathogens cell attached to it, the resonance frequency decreases proportional to the mass added. The FEA analysis of a single particle of 1 micron diameter of polystyrene, which is placed on the micro resonator, is performed. The results show a decrease of 307 Hz in resonance frequency due to the small particle, and is proportional to the mass of the polystyrene particle. The Von mises stress is also found at the resonant frequency, which is less than the elastic limit of all the structural layers i.e. 3C-SiC, AlN, and Mo. Also unlike silicon-based biosensors that require a gold layer on top and modification of it for antibody attachment the immobilization of the antibodies can be done via amino propyl tri ethoxy silane (APTES) linker on 3C-SiC surface which reduces the costly and tedious fabrication steps of gold deposition. These results are based on the Finite Element Analysis results only. The actual device will be fabricated and tested in future.

Conclusion:

The mathematical modeling and Finite Element Analysis (FEA) of a bio sensor based on cubic silicon carbide (3C-SiC) for pathogen detection is presented in this paper. The resonator is proposed to actuate electrically while piezoelectric sensing will be employed to detect the shift in the resonant frequency. The AlN is chosen as a piezoelectric material due to its high Curie temperature and similar thermal expansion coefficient with 3C-SiC to reduce the thermal stresses. The design parameters such as length, width, and resonance frequency were optimized using Matlab, and the design was evaluated using the Comsol and Intellisuite software for finite element analysis. 3C-SiC is chosen due to its excellent material properties and ease in functionalization compared to silicon which reduces the expansive and tedious steps of depositing gold on Si for functionalization. The functionalization of the 3C-SiC is also proposed in this paper. The close agreement between the analytical model and simulation results verify the design and working of the proposed bio sensors.

Acknowledgment

This work is supported by Queensland Micro- and Nanotechnology Centre (QMNC) and Griffith School of Engineering. This work was performed in part at the Queensland node of the Australian National Fabrication Facility, a company

established under the National Collaborative Research Infrastructure Strategy to provide nano and microfabrication facilities for Australia's researchers.

References

- [1] E. Noel du Toit, L.W. Brian and K. Sang-Gook, " Design considerations for MEMS-scale piezoelectric mechanical vibration energy harvesters", Integrated Ferroelectrics, vol. 71, pp.121-160.
- [2] S. P. Beeby, M. J. Tudor, and N. M. White," Energy harvesting vibration sources for microsystems applications." Meas. Sci. Technol. 2006;17:R175-R195.
- [3] S. Roundy, PK Wright, "A Piezoelectric vibration based generator for wireless electronics",Smart Mater. Struct., vol: 13, pp.1131-1142, 2004.
- [4] F. Hua-Bin, L Jing-Quan, X Zheng-Yi, Lu D, W .Li and C .Di, " Fabrication and performances of the MEMS-based piezoelectric power generator for vibration energy harvesting", Microelectronics Journal., vol:37, pp: 1280-1284, 2006.
- [5] Fang Hua-Bin, Liu Jing-Quan, XuZheng-Yi, L. Dong, D. Chen and Cai Bing-Chu, " An MEMS-based piezoelectric powergenerator for low frequency vibration energy harvesting.", Chinese Phys.Lett., vol:23, pp. 732, 2006.
- [6] T. H. Lee, S Bhunia and M. Mehregany, "Electromechanical computing at 500C with Silicon Carbide", Science, vol:329, pp:1316-1318, 2010.
- [7] A. H. Epstein, "Millimeter-scale, Micro-ElectroMechanical Systems gas turbine engines", ASME journal of Engineering for Gas Turbines and Power, vol:126(2), pp: 204-226, 2006.
- [8] G.W. Hunter, P.G. Neudeck and J. Xu, "Developed of SiC-based gas sensors for aerospace applications", Material Research Society Symposium Proceeding, vol.815, 2004.
- [9] PM Sarro, "Silicon Carbide as a new MEMS technology", Sensors and Actuators,vol:82, pp:210-218, 2008.
- [10] J.M.R. Kudimi, F. Mohd-Yasin and S. Dimitrijev, " SiC-Based Piezoelectric Energy Harvester for Extreme Environment", Procedia Engineering, vol. 47, pp. 1165-1172, 2012.

8.3. Comparison of Seven Cantilever Designs for Piezoelectric Energy Harvesters Based On Mo/AlN/3C-SiC

Abid Iqbal^{1*} and Faisal Mohd-Yasin

*Queensland Micro- and Nanotechnology Centre, Griffith University,
Brisbane, QLD 4111, AUSTRALIA*

Abstract— This paper compares the performances of seven different cantilever designs (straight beam, straight-tapered beam, T beam, U beam, V beam, V-T beam and Y beam) to be employed as a piezoelectric energy harvester. All cantilevers employ the same materials i.e. Aluminium Nitride as a piezo layer, Cubic Silicon Carbide as a structural layer and Molybdenum as the proof mass and electrical electrodes. The thicknesses of these layers are equal for all structures. Their performances are compared in term of resonant frequency, maximum displacement, open-circuit voltage, and stress. The results reveal that the V-T shaped cantilever beam energy harvester emerges as the overall winner.

Keywords— Aluminium Nitride; Piezoelectric Energy Harvester; Silicon Carbide; Finite Element Analysis (FEA); Cantilever Beams

Introduction

Micro-scale wireless electronic sensors are traditionally powered by chemical fuel cells. The limited life span of the battery and its difficulty to replace prompted researchers to harvest ambient energy from the environment. The prominent ambient sources are solar, wind, biogas, acoustic, mechanical vibrations and thermoelectric [1]. The mechanical vibration is harvested via three transduction mechanisms i.e. electrostatic, electromagnetic and piezoelectric [2]. The parasitic capacitance present within the electrostatic transducer, and the high output impedance limits the output current, and hence reduces the generator efficiency. The electromagnetic generators are difficult to

fabricate on the micro-scale due to the complex properties of planar magnets, the minimum number of coil turns and difficulty in integration. The piezoelectric energy harvester is the most practical solution to harvest ambient vibration energy [3].

Silicon-based piezoelectric energy harvesters have been investigated by various research groups. One such group utilized lead zirconate titanate (PZT) as a piezoelectric material, silicon as a structural layer, while using nickel and platinum/titanium (Pt/Ti) as proof mass and electrodes. Their device was capable of generating 2.16 μW electric power [4]. Another research group made an array of cantilever beams to increase the power and operational frequency bandwidth capable of producing 3.98 μW of electric power [5]. Subsequent works by two groups generated 2.15 μW [6] and 0.32 μW [7] of power, respectively.

The aim of this project is to develop piezoelectric energy harvesters for harsh environments. Silicon- and PZT-based energy harvesters cannot operate at those environments due to electrical and mechanical limitations [8]. This can be overcome by employing a material which is stable in those conditions [9]. We chose silicon carbide as a structural layer because of its excellent mechanical and chemical properties such as extreme hardness, low-friction reducing mechanical wear-out and chemical inertness to corrosive atmospheres excellent mechanical and

electrical properties. Aluminium Nitride is chosen as the active piezoelectric material due to its high melting point, chemical stability and high Curie temperature ($>1200^{\circ}\text{C}$).

In this paper, we study the effect of various shapes of cantilever on resonance frequency, open circuit output voltage, strain, and stress. Four types of analysis are carried out in this study for all the proposed cantilever beams. The first is modal analysis to calculate the resonance frequency. The second is the dynamic analysis to measure the maximum displacement along the z-axis. The third is to measure the open circuit output voltage. The fourth is the stress analysis to measure the stress at the resonance frequency. In this paper, the total power generations of the proposed designs are not simulated because of Intellisuite software limitations. The total generated power depends on the value of load resistor that needs to be optimized for maximum output wattage. We planned to fabricate and optimize the sensing electronic circuitry for the proposed designs in the future.

Mathematical Modelling

The fundamental frequency (f) of a cantilever beam can be given by eq 1 or eq 2:

$$f = \frac{1}{2\pi} \sqrt{\frac{k}{m}} \quad (1)$$

$$f = \frac{1}{2\pi} \frac{h}{L^2} \sqrt{\frac{E}{\rho}} \quad (2)$$

where “k” is the spring constant of the cantilever beam, “m” is beam mass, “E” Young’s modulus, “ρ” is the density of the material, “h” and “L” are the thickness and length of the cantilever beam, respectively.

The relation between the stress and strain in a linear elastic material can be given by Hooke’s law:

$$S = sT \text{ or } T = cS \quad (3)$$

where S is the strain and T is the stress, while s is the elastic compliance constant and c is the elastic stiffness constants.

$$D = \epsilon_0 E + P \quad (4)$$

The correlation between electrical charge density displacement (D) and electric field (E) can be given by Gauss’s Law. D is electric flux density (C/m^2), ϵ_0 is permittivity of free space (F/m), E is Electric-field intensity (C/m^2), and P is Electric polarization vector (C/m^2).

The piezoelectric properties of the material can be derived using equation 3 and 4, called electromechanical coupling. Equation 5 is normally used for the direct piezoelectric effect while equation 6 is normally used for the indirect piezoelectric effect [4].

$$D = dT + \epsilon E = dT + \epsilon^T E \quad (5)$$

$$S = S^E T + d^T E \quad (6)$$

where S is a six-dimensional strain vector, T is stress vector, E is the electric field vector, D is the three-dimensional electric displacement vector, dT is a six by six compliance matrixes at constant electric field, $[d]$ is a 3×6 piezoelectric strain coefficient matrix and ϵ^T is a three by three dielectric constant matrix at constant stress. The piezoelectric strain coefficient is defined as the strain developed per unit applied electric field strength or developed charge density per given strain.



Fig. 1 Unimorph piezoelectric cantilever beam in a cartesian system

The proposed energy harvesters are based on the unimorph piezoelectric cantilever beam, as shown in Figure 1. It consists of three layers i.e. a substrate layer which also acts as the bottom layer, the piezoelectric active layer, and the top electrode which also can be used as proof mass to increase the output voltage. The proposed energy harvester is fixed at one end, at $x=0$ while it is free at another end, at $x=L$. The length and width of the proposed cantilever beam are L and w , respectively. The lengths of the three layers are kept the same, while their thickness can be different. The thickness of the substrate/bottom electrode, the piezoelectric and the top electrode layers are denoted as t_s , t_p and t_e , respectively. The Young's modulus of the substrate/bottom electrode, the piezoelectric and the top electrode are represented as E_s , E_p , and E_e , respectively. The direction of the length is poled along the x -axis, and the thickness is poled along the z -axis. The neutral plane of the cantilever is denoted as t_n . A constant force, F is applied on the cantilever tip or the free end of the cantilever in the d_{31} vibrational mode.

The open circuit output voltage can be calculated using equation 7, which depends on the cantilever beam dimensions, the material properties, and the applied force.

$$\frac{V_{avg}}{F} = \frac{L}{2} g_{31} \frac{E_p}{wD} \left(\frac{t_p^2}{2} - t_n t_p \right) \quad (7)$$

where g_{31} is piezoelectric coefficient related to the piezoelectric strain coefficient, E_p is Young's modulus of the piezoelectric, "w" is the width of the cantilever and t_p , t_n are the thicknesses of the layers respectively. D is the bending modulus per unit width and is given by equation 8:

$$D = \frac{1}{3} \left(E_s t_s^3 + E_p t_p^3 + E_e (t_e^3 - t_p^3) \right) + \\ t_n (E_s t_s^3 - E_p t_p^2 - E_e (t_e^2 - t_p^2)) + \\ t_n^2 (E_s t_s + E_p t_p + E_e (t_e - t_p)) \quad (8)$$

The maximum displacement obtained at free end can be measured using equation 9.

$$h_{max} = \frac{FL^3}{3wD} \dots\dots \quad (9)$$

Geometric Designs of Cantilevers Beams:

Thickness of each layer:

The thickness of the piezoelectric material is optimized to 1 micron for the 3C-SiC, AlN and Molybdenum layers for maximum output voltage from equation 7.

Proof mass:

The dimensions of proof mass are important in tuning the natural resonance frequency as given in equation 1. The width of the proof mass is kept the same as that of the cantilever in all cases. The effect of proof mass was studied between length ratios (L_{pm}/L) and the natural frequency of the cantilever beams, where L_{pm} is the proof mass length and L is cantilever beam length. The length of the proof mass was changed via a parametric sweep while the resonance frequency was observed. The natural frequency decreases gradually up to length ratio equal to 0.3, with an increase in proof mass. The resonance frequency decreases with further increase in the length of proof mass due to increase in stiffness of the cantilever.

Geometry:

Highly doped 3C-SiC layer is used as the structural and the bottom electrode. The energy harvesters are designed to operate in a transverse mode, in which the stress is perpendicular to the poling directions. AlN is chosen as the piezoelectric active layer. Molybdenum (Mo) is chosen for the top electrode and the proof mass, because it has similar properties as SiC and AlN. The high density is helpful as a proof mass which provides the ability for added displacement. Figure 2 shows the seven types of microresonator proposed for this study for energy harvesting. All the designs are optimized for the resonance frequency less than 2000 Hz.

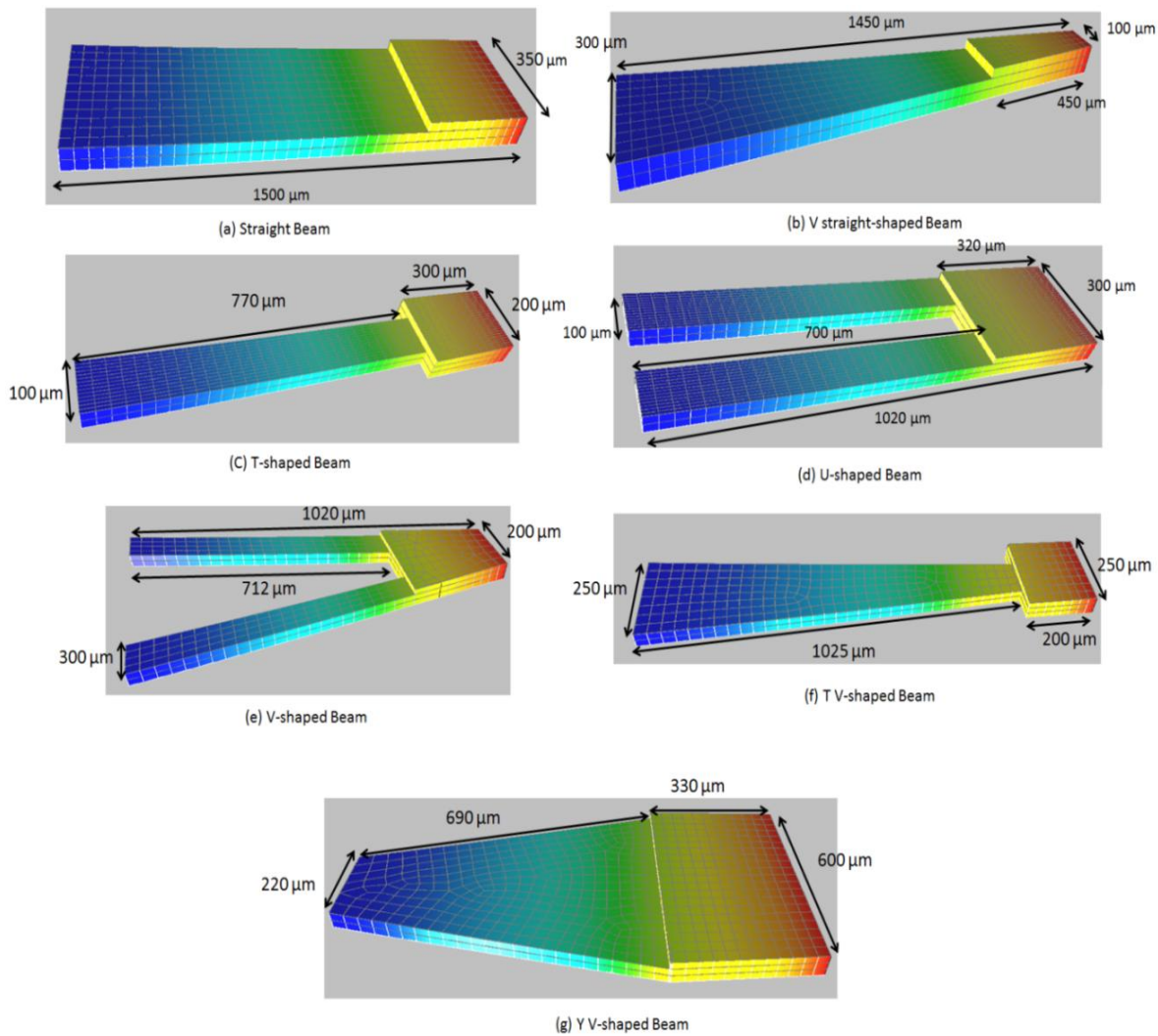


Fig. 2 Cantilever beam with various proposed shapes for piezoelectric energy harvester.

FEA Analyses:

The Finite Element Analysis is carried out using the Intellisuite. The following are the setting done for the analysis and was chosen from the mask layers:

Material Properties:

The material properties were assigned to each layer after determining the dimensions for each design in 3D builder and exporting to the TEM module for analysis.

Boundary Settings:

In these designs, two types of boundary condition are applied. Mechanical boundary condition, all the beams are constrained from one end while the load is applied on the other end in terms of the acceleration in the z-direction. In Electrical boundary conditions, the ground voltage is applied on the lower face of the piezoelectric layer while the floating voltage is applied on the upper end.

Mesh Settings

In the mesh settings, the free mesh parameters option is chosen to mesh the 3D cantilever beam. The auto mesh was chosen for all the simulations while the mask layout from the mask layers. The total number of mesh elements being arranged for all the cantilever beams is between 11000 and 20000.

Results and Discussion

Figure 3 shows the resonance frequency of all the proposed structures between 1550 Hz to 1900 Hz, which will be suitable to harvest ambient vibrations.

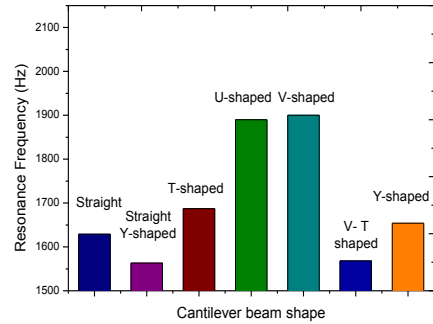


Fig. 3 Natural resonance frequency of different cantilevers

The dynamic analysis was performed by applying 1g mechanical load as shown in Figure 4.

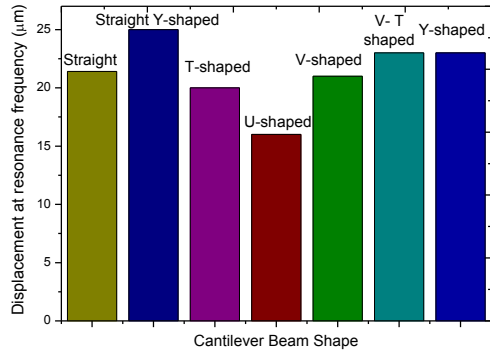


Fig. 4 Maximum displacement along z-axis

For the piezoelectric analysis, a 1g acceleration was applied along the z- direction. The results are shown in Figure 5.

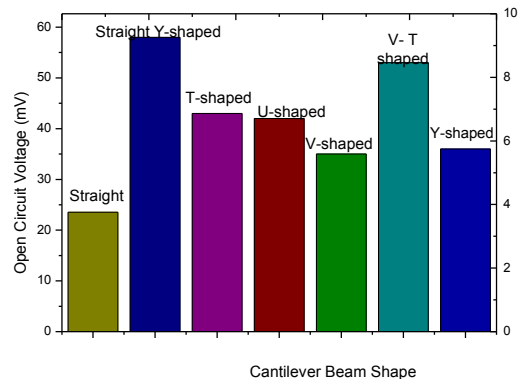


Fig. 5 Maximum open circuit voltage at resonance frequency

The stress analysis was performed as shown in Figure 6. The Von Mises's result was evaluated, and it was found that the maximum value of stress was lower than the yield strength of each structure.

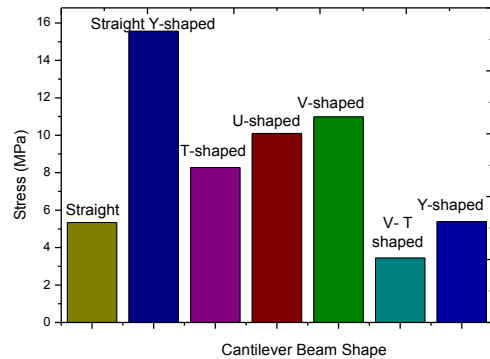


Fig 6. Maximum stress at resonant frequency

Conclusions

This paper simulated the performance of seven cantilever beams designed to harvest electrical power from mechanical vibration. The resonant frequencies for all structures are between 1550-1900 Hz. The maximum displacements are very similar for all except for the U beam due to higher stiffness. The Y beam and V-T beam generated the highest open-circuit voltage. However, the Y-shaped cantilever also yields the highest stress, making the V-T beam the overall winner.

Acknowledgements

This work is supported by Queensland Micro- and Nanotechnology Centre (QMNC) and Griffith School of Engineering. This work was performed in part at the Queensland node of the Australian National Fabrication Facility, a

Numerous research group has measured the d_{33} value in the range of 4.01 to 5.2 pm/V. Zhang et al. [1] reported the piezoelectric coefficient d_{33} value as 5.06 pm/V of AlN thin films measured by the piezoresponse force microscopy (PFM) measurement. Karabalin et al. also reported the piezoelectric coefficient d_{31} of 100 nm AlN layer as 2.4 pm/V [2]. Most of the research groups, in the literature review, has reported the value of piezoelectric coefficient (d_{33}) as 5.1 pm/V, that we used in all our simulations. However, we extracted the piezoelectric coefficient value of 4.7 pm/V for our deposited films that is about 8.5 percent lower than the value used in simulations. Repeating the simulation with our extracted values will decrease the output voltage by 8 percent.

- [1] M. Zhang, J. Yang, C. Si, G. Han, Y. Zhao, and J. Ning, "Research on the piezoelectric properties of AlN thin films for MEMS applications," *Micromachines*, vol. 6, pp. 1236-1248, 2015.
- [2] R. Karabalin, M. Matheny, X. Feng, E. Defay, G. Le Rhun, C. Marcoux, *et al.*, "Piezoelectric nanoelectromechanical resonators based on aluminum nitride thin films," *Applied Physics Letters*, vol. 95, p. 103111, 2009.

company established under the National Collaborative Research Infrastructure Strategy to provide nano and microfabrication facilities for Australia's researchers.

References

- [11] E. Noel du Toit, L.W. Brian and K. Sang-Gook (2005), "Design considerations for MEMS-scale piezoelectric mechanical vibration energy harvesters", *Integrated Ferroelectrics*, vol. 71, pp.121-160.
- [12] S. P. Beeby, M. J. Tudor, and N. M. White (2006)," Energy harvesting vibration sources for microsystems applications." *Meas. Sci. Technol.* Vol. 17:R175-R195.
- [13] S. Roundy, P. K. Wright (2004), "A Piezoelectric vibration based generator for wireless electronics",*Smart Mater. Struct.*,vol: 13, pp.1131-1142.
- [14] F. Hua-Bin, L Jing-Quan, X Zheng-Yi, Lu D, W .Li and C .Di (2006), " Fabrication and performances of the MEMS-based piezoelectric power generator for vibration energy harvesting", *Microelectronics Journal*, vol.37, pp: 1280-1284.
- [15] L. Jing-Quan, F. Hua-Bin, Xu. Zheng-Yi, M. Xin-Hui, Xiu-Cheng and Di Chen (2008), "An MEMS-based piezoelectric powergenerator array for vibration energy harvesting." *Microelectronics Journal*, vol: 39, pp.802-806.
- [16] S. Dongna, P. Jung-Hyun, A. Jyoti, C. Song-Yul, C. W. Howard, K. Dong-Joo (2008), "The design, fabrication and evaluation of a MEMS PZT cantilever with an integrated Si proof mass for vibration energy harvesting." *J. Micromech. Microeng.*, vol:18, pp. 055017.
- [17] Fang Hua-Bin, Liu Jing-Quan, XuZheng-Yi, L. Dong, D. Chen and Cai Bing-Chu (2006), " An MEMS-based piezoelectric powergenerator for low frequency vibration energy harvesting.", *Chinese Phys.Lett.*, vol:23, pp. 732.
- [18] T. H. Lee, S Bhunia and M. Mehregany, (2010) "Electromechanical computing at 500C with Silicon Carbide", *Science*, vol:329, pp:1316-1318.
- [19] A. H. Epstein, (2006) "Millimeter-scale, Micro-ElectroMechanical Systems gas turbine engines",*ASME journal of Engineering for Gas Turbines and Power*, vol:126(2), pp: 204-226.
- [20] G.W. Hunter, P.G. Neudeck and J. Xu (2004), "Developed of SiC-based gas sensors for aerospace applications", *Material Research Society Symposium Proceeding*, vol.815.
- [21] P. M.Sarro (2008), "Silicon Carbide as a new MEMS technology", *Sensors and Actuators*

Chapter 9: Conclusions and Recommendations

9.1. Conclusion:

The primary contribution of this work is to provide details of the deposition of a highly oriented c-axis AlN thin film on top of 3C-SiC/Si substrates. A 3C-SiC buffer layer was used to decrease the lattice mismatch and the difference in the coefficient of thermal expansion between the AlN film and the Si substrate.

Chapter 2 (unpublished) provides a literature review of the published works on sputtered AlN (002) films on a variety of substrates. The main contribution is the generic range of sputtering parameters and their roles towards achieving the objective. This chapter also offers the physical explanations of the effect of the sputtering parameters in view of kinetic energy and surface mobility of the adatoms.

Chapter 3, which has been published in the Journal of Vacuum Science and Technology-B describes the first attempt to produce AlN thin films on top of 3C-SiC/Si (100) substrates using RF sputtering. The GIXRD results revealed that a low pressure, high power, and median nitrogen concentration all play an important role in the AlN deposition. AlN films with (002), (100) and (101) orientations were produced, albeit at the low deposition rate.

Chapter 4, which has been published in the Journal of Crystal Growth documents the first attempt using DC sputtering to overcome the low deposition rate issue. The main contribution is the observation that the crystal orientation of AlN can be controllably changed from (002) to (101) on top of 3C-SiC/Si (100) substrates by increasing the N₂/Ar flow rate from 40 % to 100 %. It is also the first time that the effect of RF Bias voltage to tune the residual stress on the AlN films has been demonstrated.

Chapter 5, which has been submitted to the Journal of Crystal Growth documents the improved results that have been obtained on top of 3C-SiC/Si (111) substrates. The GIXRD and the rocking curve measurement demonstrate that AlN (002) films have been successfully produced over a wide range of N₂/Ar ratio. This is attributed to the low lattice mismatch of 1 % between AlN (002) film and 3C-SiC (111) buffer layer. It should be noted that the samples from chapter 4 and 5 have been batch-processed using the same equipment and process

parameters. The main disadvantage of this process is the ‘electrical arcing’ during deposition that shuts down the power.

Chapter 6 (unpublished) introduces the use of the pulsed-DC sputterer to overcome the electrical arcing, as well as to crank to the sputtering power up to 2400 W. During this experiment, highly c-axis AlN (002) has been deposited on top of two types of 3C-SiC/Si (111) substrates, the on-axis and 4⁰ off-axis. The literature survey reports that the latter has smoother surface, less stacking fault density and smaller bow magnitude. The GIXRD scan and the rocking curve measurements confirm the superiority of the off-axis 3C-SiC/Si (111) substrate in depositing AlN (002) with higher crystal quality, smoother surface and lower residual stress.

Chapter 7 (unpublished) employs the same pulsed-DC sputtering system to deposit AlN (002) films on top of 3C-SiC/Si (100) substrates. The role of substrate temperature and sputtering power on growth of AlN films are elucidated. There are two key contributions. The crystal quality increases with an increasing substrate temperature and sputtering power, which is in agreement with literature. Interestingly, the value of the residual stress decreases with increasing substrate temperature and sputtering power, in contrast to the literature.

Chapter 8 presents three conference proceedings on the simulated applications of the AlN (002) on top of the 3C-SiC/Si substrates as energy harvester and bio-sensor. The main contributions are the optimization of the design and dimensions of the proposed structures using numerical analysis and COMSOL simulations.

9.2. Suggestions for future research

The most immediate future work is the fabrication of the structures that were proposed in chapter 8. The material advantages of 3C-SiC layer should be tested through the application of piezoelectric energy harvesters at high temperatures. The chemically-inert advantage of the 3C-SiC layer should be tested with the application of bio sensor for pathogens detection.

Aluminium nitride has been explored as a key material to make RF MEMS switches and resonators due to its high acoustic velocity. The micro- and nano-resonators based on

Mo/AlN/SiC composite structure should be designed and fabricated. Those resonators will have potentially high resonance frequency because of the relatively high Young's modulus of the 3C-SiC layer. The SAW and BAW chemical sensors are another prospective area, where the advantages of the material properties of SiC and AlN can be explored.

Piezoelectric-based pressure sensor could also be developed based on a proposed Mo/AlN/SiC composite structure. A proposed sensor will have the advantages of small dimension, excellent durability, high sensitivity and capability of working in harsh environmental conditions.